Imaging stellar surfaces with intensity interferometry:

Laboratory simulation of a large telescope array

Tiphaine Lagadec

Lund Observatory
Lund University

2014-EXA89

Degree project of 60 higher education credits (for a degree of Master)
August 2014

Supervisor: Dainis Dravins

Lund Observatory
Box 43
SE-221 00 Lund
Sweden

Abstract

Context. Intensity interferometry was invented and used by R.Hanbury Brown and R.Q.Twiss in the 1960's to measure stellar angular diameters. Its main advantage over conventional interferometry is that it enables very long baselines and is insensitive to poor seeing. However, because it requires very large light collectors, it was never pursued further.

The Cherenkov Telescope Array (CTA) is a new upcoming facility that will detect rapid flashes of optical Cherenkov light induced by extraterrestrial gamma-rays. Its large telescopes could very well be used part-time for intensity interferometry. With its 2 km maximum baseline, it could image surfaces of hot stars at an unprecedented sub-milliarcsecond resolution.

Aim. To experimentally simulate intensity interferometry in the laboratory with an array analogous to the planned CTA.

Methods. Small pinhole apertures were illuminated by experimentally produced light with appropriate quantum statistics to simulate stars. High-speed single-photon counting avalanche diode detectors mounted on laboratory telescopes made up the array, enabling more than 100 baselines. A digital data processor was used to calculate the spatial coherence of the stars.

Results. Intensity interferometry was successfully performed for stars of different sizes and shapes. With all the baselines available, it was possible to reconstruct two-dimensional maps of the spatial coherence required for image restoration.

Conclusions. The results experimentally demonstrated the validity and potential of a multi-telescope array similar to the CTA for stellar surface imaging.

Populärvetenskaplig sammanfattning

Stjärnorna på himlen syns vara små eftersom de är avlägsna objekt, solar på enorma avstånd. Den närmaste stjärnan är Alfa Centauri på ett avstånd av 4,4 ljusår, cirka 41 miljon miljoner kilometer. Solen är den enda stjärna vars yta vi kan se i detalj medan andra stjärnor är så avlägsna att de inte ens i de största teleskopen syns som mer än små ljusa prickar.

De skarpaste bilder som i dag erhålls av himmelsobjekt fås med så kallade interferometrar. Dessa är anläggningar där flera teleskop kopplas ihop för att bilda ett gemensamt större instrument. Kraftfullast bland dessa är Europeiska Sydobservatoriets interferometer i Chile och dess amerikanska motsvarighet i Kalifornien. Med dessa har man lyckats avbilda ett fåtal stora stjärnor. Någon visade sig inte vara rund utan kraftigt avplattad eftersom den snurrar jättesnabbt kring sin axel. Andra stjärnor kan tänkas ha andra former eller kan bestå av flera stjärnor i omloppsbanor tätt kring varandra. Att se stjärnor som utsträckta objekt kan lära oss mycket om dem men också om vår egen stjärna, solen.

De stjärnor som hittills kunnat avbildas är jättestjärnor, mycket större än solen, och det finns tusentals ljusa stjärnor som fortfarande bara kan ses som prickar. Bildskärpan i en interferometer bestäms av avståndet mellan de teleskop som ingår i anläggningen: större avstånd ger bättre skärpa. Fastän man sedan länge drömt om att länka teleskop över många kilometrar, är det ännu inte möjligt över mer än ett par hundra meter. Begränsningarna sätts av kraven på extrem precision i hur ljuset mellan teleskopen måste kombineras, samt av luftoron i jordens atmosfär.

En annan teknik, så kallad intensitets-interferometri, tillåter längre avstånd mellan teleskopen och därmed en högre bildskärpa. Metoden innebär att det synliga ljuset i teleskopet omvandlas till elektroniska signaler som överförs i kablar utan att störas av luftens turbulens. Nackdelen är att viss information går förlorad, vilket gör det svårare att återskapa bilder av himmelsobjekten. Dessutom kräver denna teknik mycket ljus och därför också stora teleskop.

Genom en historisk tillfällighet uppförs nu en anläggning med sådana stora teleskop, CTA, “Cherenkov Telescope Array”, för ett helt annat huvudändamål, att observera gammastrålning från världsrymden. När energirika gammastrålar tränger in i jordens atmosfär, skapas partiklar som utsänder blixtar av blåaktigt ljus, så kallad Tjerenkovstrålning. Eftersom denna är mycket ljussvag, måste teleskopen vara både stora och många. Teleskopens prestanda råkar motsvara vad som krävs för intensitets-interferometri och möjligheten till denna tillämpning har uppmärksammats inom projektet. Teleskopen kommer att ligga på avstånd upp till ett par kilometrar vilket möjliggör en bildskärpa som är storleksordningen bättre än med dagens anläggningar. Detta kommer att möjliggöra avbildning av främst stjärnor som är hetare än solen (tekniken fungerar bäst för varmare stjärnor). Möjligen kommer man till och med att kunna se silhuetter av planeter när de syns passera över stjärnskivan!

Eftersom tekniken aldrig använts med modern digital elektronik, måste metoderna utvecklas och testas innan observationer i full skala kan påbörjas. Detta är vad som gjorts i detta examensarbete. Många små teleskop sattes upp i ett laboratorium i ett mönster motsvarande det kommande CTA. Med denna installation mättes olika konstgjorda stjärnor. Efter analys av mätningarna, kunde storlek och form på de olika “stjärnorna” bestämmas och det kunde experimentellt visas att teorin fungerade. Detta är första gången som avbildande intensitets-interferometri genomförts för astronomiskt relevanta objekt. Med denna teknik torde det bli möjligt att erhålla bilder av stjärnytor när CTA kommer i drift någon gång kring år 2020.

Acknowledgements

First of all, I would like to thank my supervisor, Dainis Dravins, for introducing me to the fascinating subject of intensity interferometry. I also thank him for his complete investment and support in the project. Further, I thank him for his help proofreading my thesis and translating my popular abstract into Swedish.

I would also like to thank Paul Nuñez for organizing the Hanbury Brown & Twiss workshop in Observatoire de la Côte d'Azur in Nice, thus giving me the opportunity to meet the intensity interferometry community and to present my project. I am also very thankful for his considerate collaboration in reconstructing images out of my experimental data.

Additionally, I thank SPIE, the international society for optics and photonics, for giving me a grant to travel to the SPIE *Astronomical Telescopes + Instrumentation* conference in Montréal, in June of this year.

Finally, I thank Henrik Rhodin and Petter Thorén for helping in cleaning up the optics laboratory; without their help I would not have been able to conduct this experimental project.

Contents

Abstract **3**

Populärvetenskaplig sammanfattning **5**

1 Context of the project **13**
1.1 Imaging stars 13
1.2 History and prospects for stellar interferometry 15
1.3 Stellar intensity interferometry 21
1.3.1 Retrospective on intensity interferometry 21
1.3.2 The potential of intensity interferometry 22
1.3.3 The Cherenkov Telescope Array: An opening for intensity interferometry 23
1.3.4 Previous simulations 25

2 Optical coherence theory **29**
2.1 Diffraction of light 29
2.2 The coherence of light 33
2.2.1 Temporal coherence 33
2.2.2 Spatial coherence 36
2.2.3 Interference of spatially coherent beams of light 37
2.2.4 Interference of temporally coherent beams of light 39
2.3 The Michelson stellar interferometer 41
2.4 The intensity interferometer 43
2.4.1 General principles 43
2.4.2 The signal to noise ratio 44
2.4.3 Higher-order correlations 45
2.4.4 Quantum interpretation 45

3 Laboratory set-up **49**
3.1 Overall set-up 49
3.2 Detectors 52
3.3 Correlator 54
3.4 Artificial stars 55
3.5 Focussing the telescopes 58
3.6 Experimental procedure 59

4 Artificial star diffraction images **63**

5 Intensity interferometry of stars 67
5.1 Reading and plotting the data 67
5.2 Visibility curves for three round stars 72
5.3 2D visibility map for a binary system 73
5.4 2D visibility map for an elliptical star 75
5.5 Image reconstruction 77

6 Additional tests 79
6.1 Different scatterers 79
6.2 Polarization effects 81

7 Discussion and conclusion 83
7.1 Interpretation of the experimental results 83
7.2 Lessons learned 85
7.3 Ideas for future improvements 87
7.4 Issues encountered 88

8 Summary 89

Publications 91

Bibliography 94

Chapter 1

Context of the project

1.1 Imaging stars

Stars are faraway objects and subtend small angles in the sky. They also form a vast variety of objects and present complex structures such as stellar winds, disks, binary companions, etc. Imaging stars is motivated by the desire to understand these objects better and to confront stellar surface models against actual observations. Furthermore, imaging in general represents a key approach to a broader public, and thus to the popularisation of astronomy.

In order to resolve stars as extended objects, and not only as point sources, very high resolution instruments are required. The capability of a telescope in resolving an object can be approximated with the diffraction-limited angular resolution:

$$R = 1.22\frac{\lambda}{D}, \tag{1.1}$$

with λ the wavelength of the light observed, D the aperture of the telescope, with R in radians. This limit comes from the diffraction effect, an effect occurring in any optical system of finite size. However this relation only holds for a perfect optical system and in most cases R will be altered by different factors. The most critical cause of alteration in a ground-based telescope comes from the Earth's atmosphere. When starlight enters the atmosphere it suffers many phase jumps due to various turbulent air flows. It results in a distorted star image. In this manner, the resolution of a telescope can sometimes be decreased by a factor of 100! The effect of turbulent air flows is attenuated for dry climates with steady air and for this reason, large telescopes are often built in arid places. Furthermore, Equation 1.1 suggests a higher resolution for shorter wavelengths λ, but in reality that is complicated to achieve since short wavelengths are more affected by turbulence.

Typical bright stars subtend angles of a couple of milliarcseconds, with the largest reaching on the order of 30 milliarcseconds. Figure 1.1 shows the distribution of angular diameters of bright stars. Resolving one of the largest of these stars would thus typically require a telescope of ≈ 5 m, and larger than ≈ 50 m for resolving details 10 times smaller on the star. However, these telescope size estimations are for the diffraction-limited case only.

For all of these reasons, achieving high angular resolution is a huge challenge, instruments reaching the current highest resolution are indeed state-of-the-art instruments. One way of dealing with the atmosphere is to observe from space. In this manner Hubble Space Telescope produces stunning images of the universe, and its successor, the James Webb Space Telescope, is avidly awaited. Back on Earth, atmospheric effects can be corrected by adaptive optics or by speckle analysis. Currently, the facilities producing the highest angular resolution are interferometers.

In the next sections, interferometry is introduced by giving a historical perspective, a portrait of the current state and some future prospects. The discussion is focused on the optical domain only. The particular technique of intensity interferometry is further discussed in more detail as it is the subject of this thesis. Motivations for the technique are presented. Finally, a revival opportunity for this last technique with the Cherenkov Telescope Array is outlined. Previous simulations are shown, introducing the particular goals of this thesis project.

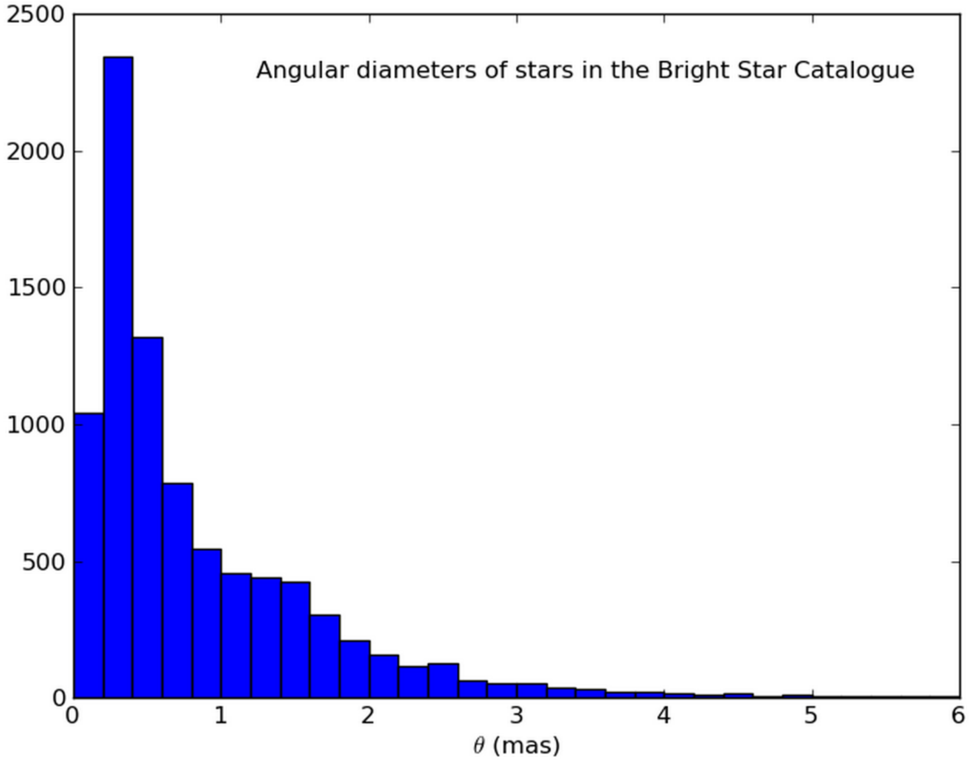

Figure 1.1: Angular diameter distribution of stars from the Bright Star Catalogue [1]. The Y-axis shows the number of stars. Figure from [2]. First the effective temperature of the stars were estimated by fitting a polynomial model to the data of the B-V color indexes. The angular diameters were then calculated from those effective temperatures assuming the stars were perfect blackbodies with uniform circular disk.

1.2 History and prospects for stellar interferometry

This section aims to give a historical background to stellar interferometry. The current state of the technique is described later together with some future prospects. To make the reading easier, Figure 1.6 at the end of this section, summarises the information of the historical development of stellar interferometry into a timeline scheme. This figure was inspired by a similar figure in [3].

Hippolyte Fizeau was the first one to suggest that the tight relation between the dimensions of the source and the dimensions of the interference fringes in a Young's slits experiment could be used to measure angular diameters of stars. He thought of using such a Young's slits configuration in front of a telescope to produce interference of the light coming from a star and deduce its angular extent. The idea was suggested for the *Prix Bordin* awarded by the *Académie des Sciences* already in 1867. At that time the idea was judged ingenious but too difficult to realise [4]. It was not until 20 years later that Michelson gave a complete mathematical description of stellar interferometry [5]. In 1891, he became the first to successfully obtain fringes of Jupiter's satellites, allowing the measurement of their angular diameters [6]. He did so by using the same method as that suggested by Fizeau; he covered the objective of a 30 cm telescope by two symmetrical and adjustable (in width and distance) slits.

In 1920, John August Anderson collaborated with Michelson, on a new design of stellar interferometry. They discovered that the resolution in interferometric measurements was insensitive to poor seeing, but they also discovered that a 10 m telescope would be needed to resolve an object of ≈ 0.01 arcsecond, which was not conceivable at this time. Instead Michelson understood that the baseline (distance between the two slits) was itself the limiting parameter. Thus, in 1921, they studied and built a new interferometer design on Mount Wilson: Figure 1.2 (left). The light from a star observed at an angle θ was collected by two small mirrors M1 and M4 separated by a distance d and then sent to the principal mirror of the telescope by use of two small relay mirrors M2 and M3. They used the Hooker telescope of 2.5 m diameter (Figure 1.2, center) on Mount Wilson. The interferometric system was temporary added to the structure of the telescope as shown in Figure 1.2 (right). The final arrangement was finally successfully used for approximatively 10 years, to measure angular diameters until all the brightest stars reachable with their interferometer had been measured.

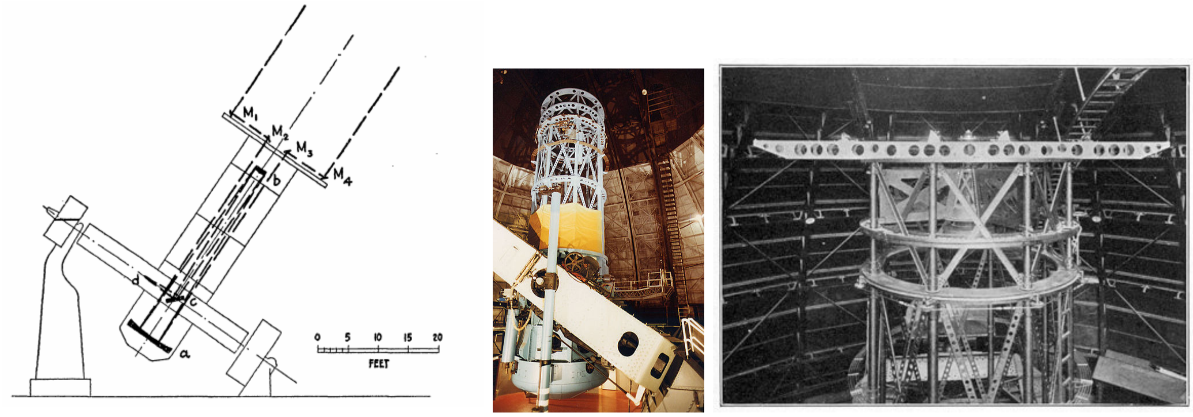

Figure 1.2: [Left] Schematic view of the set-up for interferometry on the Hooker telescope, figure from Michelson [7]. [Center] 2.5 m Hooker telescope on Mount Wilson as it looks today. [Right] Part of the Hooker telescope on Mount Wilson as it was used by Michelson for stellar interferometry.

Because of the comprehensive work on Mount Wilson on measuring stellar angular diameters, no easy improvements could be achieved, and interferometry was relatively forgotten for about 30 years.

However, in less energetic parts of the electromagnetic spectrum, in radio astronomy, interferometry started developing considerably. During World War II, the electronics and detectors underwent great advancements, significantly benefiting science, including radio astronomy. In 1954, R. Hanbury Brown together with R. Q. Twiss elaborated a novel method of radio interferometry, intensity interferometry [8]. While previously, interferometry dealt with the optical superposition of the light, thus the amplitude of light, intensity interferometry looks at the superposition of the intensity. Here, by "superposition" is meant "multiplication"; indeed there is no physical superposition of light in an intensity interferometer. Instead, the rapid variations of the light intensity are measured by two detectors at two different locations. The signals are then brought together electronically to be multiplied. The result is a mathematical correlation function that tells about the angular diameter of the source. So, the quantity deduced by an "amplitude" and an intensity interferometer are the same, but the techniques are different. Soon after successfully utilising the technique in the radio, R. Hanbury Brown and R. Q. Twiss decided to build an optical intensity interferometer. The resulting interferometer was built in Narrabri, in Australia, in 1962, and was the first optical interferometer that made use of two different telescopes. It was possible because the intensities were recorded and brought together electronically, making it possible to have long baselines. The mirrors could be moved around a circle of 188 m diameter, representing the longest baseline (Figure 1.3). It was limited in that it could in practise only measure stars with visual magnitude brighter than 2.5, and thus it met the same fate as the Michelson interferometer on Mount Wilson, and stopped operating in 1974, after all the bright southern stars had been measured. It was planned to build a new and larger intensity interferometer, unfortunately this idea was abandoned given a then renewed excitement for the Michelson interferometer.

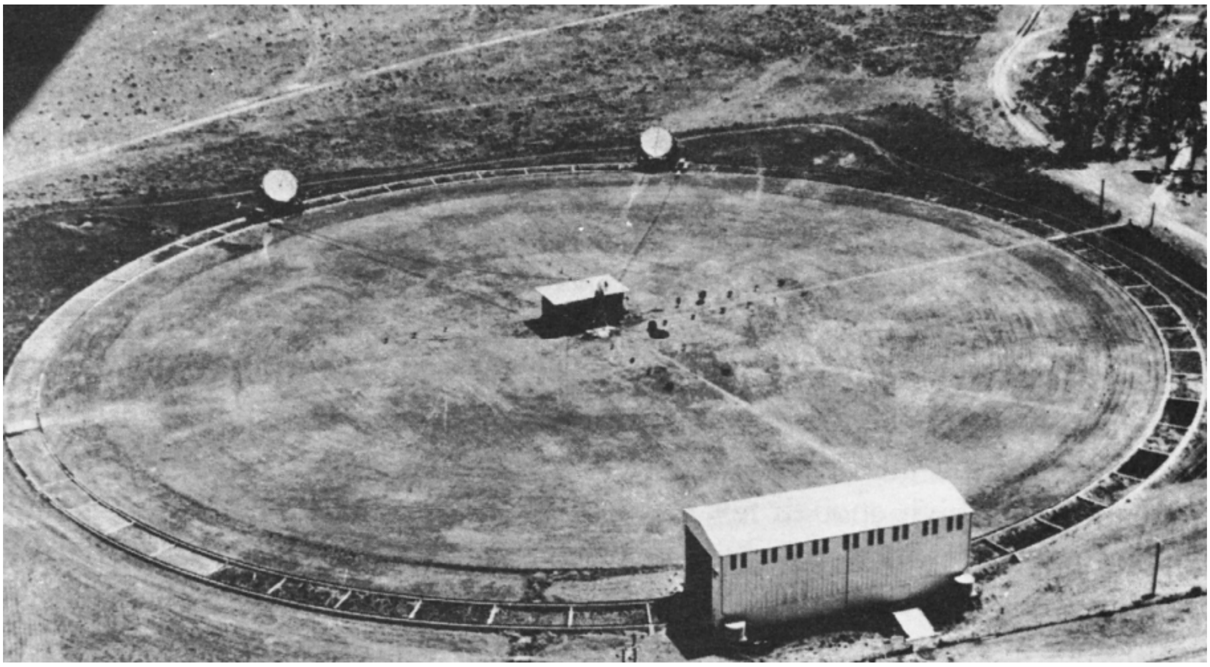

Figure 1.3: The unique intensity interferometer, in Narrabri, as it looked when operating [9].

The renewal of interest for Michelson stellar interferometry started what is currently referred to as modern interferometry in astronomy. It began with a few astronomers who recognised the potential of newly available detectors at that time [10] [11] [12].

In 1970, Antoine Labeyrie developed a method called "speckle interferometry". Aided by the work of R. Hanbury Brown and R. Q. Twiss on the photon statistics, the principle of his method is to freeze the speckle pattern of star seen through atmospheric with a fast camera, and in this manner enable to correct for the atmospheric distortion. Speckles are small patterns that in this case are due to the atmosphere, which distorts the wavefront, inducing random phase jumps. The light thus interferes with itself at random very small locations of the wavefront. Continuing his work on stellar interferometry, Labeyrie built the *Interféromètre à deux télescopes* (I2T) at Nice Observatory in France, in 1974; Figure 1.4. It was the first optical amplitude interferometer to operate with two different telescopes. The two light beams from the 26 cm telescopes were sent via mirrors through an optical path and superposed for a total baseline of 12 m [13]. Following his results with the I2T, he obtained funding and started building the *Grand Interféromètre à deux télescopes*, which started operating in 1987. The telescopes were equipped with 1.5 m mirrors and separated by a baseline of 70 m [14].

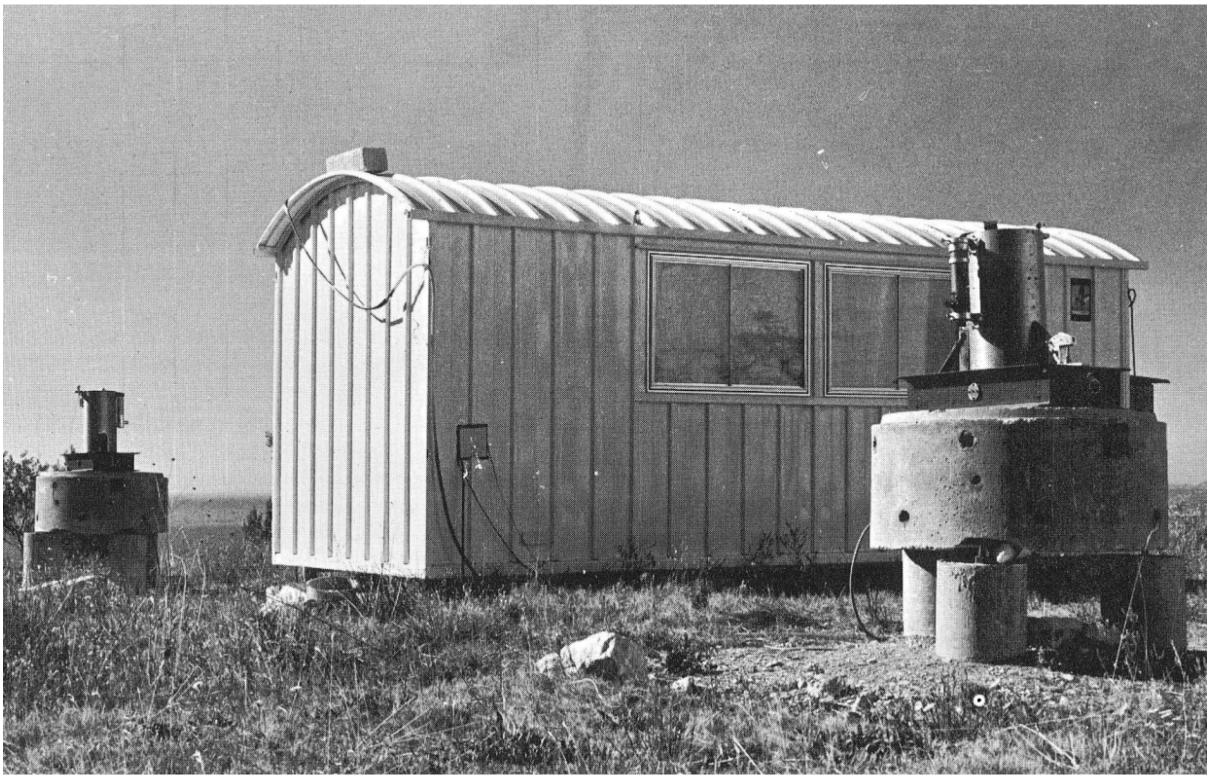

Figure 1.4: Interféromètre à deux télescopes in Nice, France, in 1974 [13].

Around the same time M. Ryle was awarded the Nobel prize for his contribution to aperture synthesis in radio astronomy. A technique that uses several radio antennas for interferometry, and by applying retrieving algorithms from a Fourier analysis, produces a combined antenna that has the effective resolution of its maximum baseline. This revolutionary technique allowed the production if images with interferometry. The theory was first developed for radio waves because their long wavelengths are more suited to fit the Maxwell description of radiation. Their formalism is consequently much simplified in comparison to that for optical waves. In other words, the phase-amplitude relationship is precisely defined for radio waves. The side effect of such long wavelengths is given by Equation 1.1, meaning that very large apertures are needed to reach sensible resolutions. Thus, an enhancement of the resolution of radio telescopes was needed more than in any other energy range.

As computational power also progressed significantly, other sophisticated techniques arose, such as, for instance, fringe tracking. It was then possible to start envisioning searches for exoplanets, very long baselines and aperture synthesis for also the optical domain [15] [16]. In the 1980's aperture synthesis was finally exploited in the visible range, and demonstrated on an array of separated telescopes, COAST (Cambridge Optical Aperture Synthesis Telescope) which was developed later in 1995 [17].

In 1977, the project of a very large array of optical telescopes was started by the European Southern Observatory, the VLT (Very Large Telescope). It began operating in 1998, and was successively implemented with additional telescopes. In its final version it is now composed of 4 primary telescopes (referred as UT, Unitary Telescopes) of 8.2 m diameter and 4 auxiliary telescopes (AT) of 1.8 m. The AT's are operated together as an interferometer for a maximum baseline of 202 m. For some part of the VLT observation time, both the AT's and the UT's are used together to form an even larger interferometer. At this moment they reach a resolution of 1 mas. When used for interferometry, the light passes through multiple underground mirrors, which must be aligned (with the optical path in air) with a precision of a fraction of an optical wavelength over a few hundred meters. This represent the largest challenge for optical interferometry. For this reason, it is at today hard to build an optical interferometer with baseline longer than a few hundred meters. The technique is thus confined mainly to bright stars with mainly wavelengths in the infrared. In addition, many baselines imply the need to split up the light into more beams in order to have it interfering between more pairs of telescopes. Currently, this is only doable for a limited numbers of telescopes (unless someone invents a way of duplicating photons). The VLT is shown in Figure 1.5, which shows the 4 large UT's and 3 of the AT's.

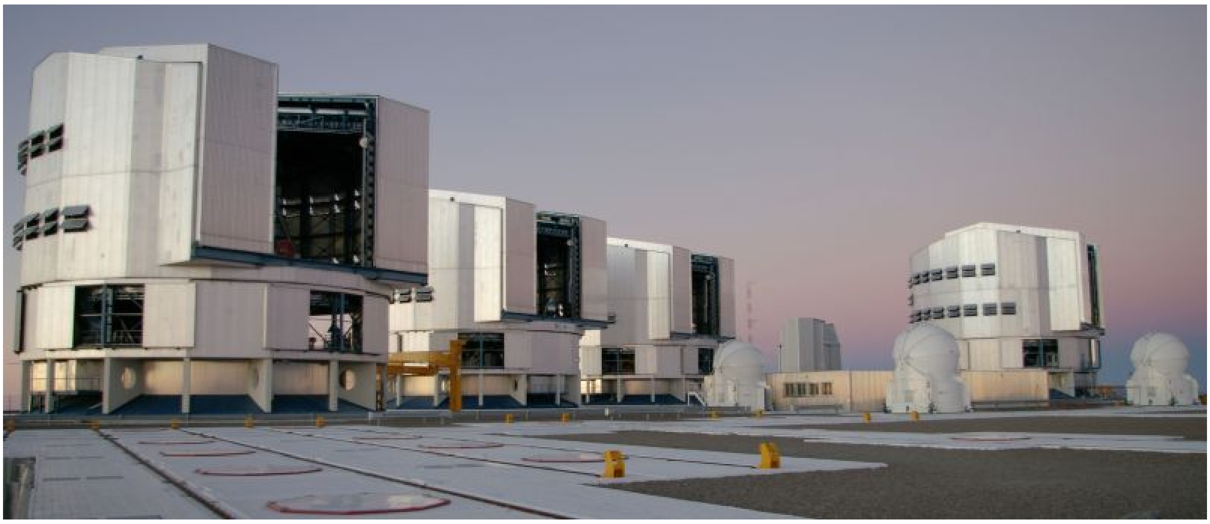

Figure 1.5: VLT on Paranal, the 4 large UT's can be seen and 3 of the 4 AT's, image from ESO.

In parallel, in 1995, Georgia State University selected Mount Wilson to build the CHARA (Center for High Angular Resolution Astronomy) array, very similar to VLTI. The array is composed of 6 telescopes of 1 m aperture working together for stellar interferometry, for baselines up to 331 m. The light beams are carried by three optical arms into a beam synthesis facility, were they are then assembled with a sub-micron precision. In 1999 it produced its first fringes. It operates in the optical as well as infrared. It possesses the same advantages and limitations the VLT, but has a longer possible baseline.

In this manner, the VLTI and CHARA, are currently producing astonishing results at high angular resolution, but still a few orders of magnitude below what is necessary for stellar surface imaging (except for few large stars). Gigantic telescopes projects are now ongoing such as the European Extremely Large Telescope (E-ELT), a telescope of 39.3 m planned aperture, the TMT (Thirty Meter Telescope), or the Giant Magellan Telescope (GMT) composed of seven 8.4 m mirrors forming a large mirror of 24.5 m equivalent diameter. Those projects are the largest projects for the coming years in the optical. It is also clear that no telescope larger than a hundred meters, nor interferometers longer than some hundred meters will be built in the near future. Even if stellar interferometry has had a huge development in the last century, the longest baseline available is only hundreds of meters, compared to thousands of kilometers in the radio domain. A lot of projects, more or less old, have carried the dream of a kilometric stellar interferometer. Among some futuristic projects are a Moon-based interferometer [18] or even a huge space interferometer such as the Hypertelescope by Antoine Labeyrie [19]. The Hypertelescope would be a space interferometer composed of very many telescopes positioned in a parabolic geometry reducing the need for pathlength equalization. It has been envisioned that the telescopes would have a separation reaching even a hundred kilometers, which could allow to image exoplanets and reveal details on their surfaces! However, the probable cost for such futuristic projects appears highly prohibitive, meaning that they will not likely happen in any near future.

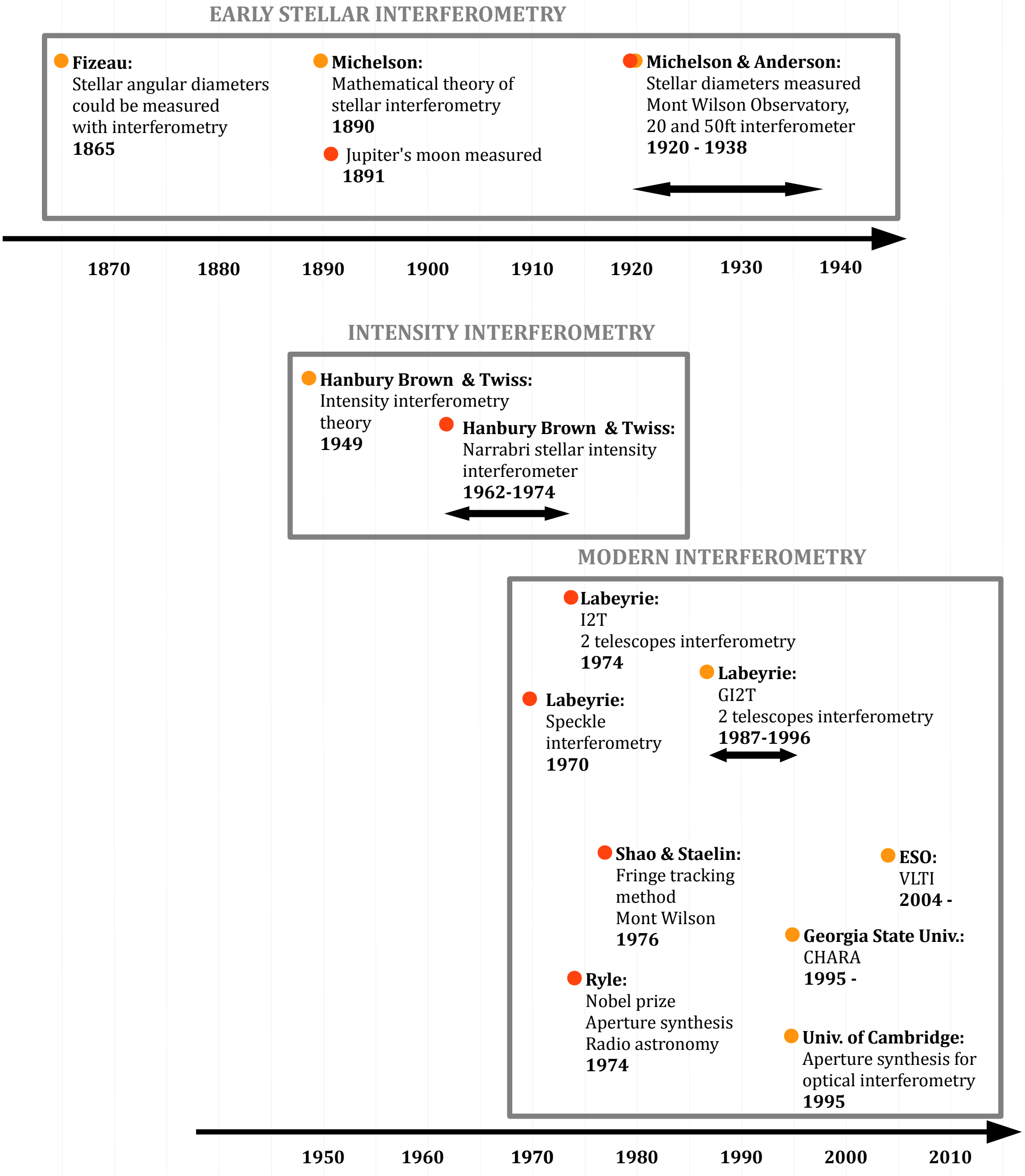
EARLY STELLAR INTERFEROMETRY
Fizeau:
Stellar angular diameters could be measured with interferometry
1865
Michelson:
Mathematical theory of stellar interferometry
1890
Jupiter's moon measured
1891
Michelson & Anderson:
Stellar diameters measured Mont Wilson Observatory, 20 and 50ft interferometer
1920 - 1938
1870
1880
1890
1900
1910
1920
1930
1940
INTENSITY INTERFEROMETRY
Hanbury Brown & Twiss:
Intensity interferometry theory
1949
Hanbury Brown & Twiss:
Narrabri stellar intensity interferometer
1962-1974
MODERN INTERFEROMETRY
Labeyrie:
I2T
2 telescopes interferometry
1974
Labeyrie:
GI2T
2 telescopes interferometry
1987-1996
Labeyrie:
Speckle interferometry
1970
Shao & Staelin:
Fringe tracking method
Mont Wilson
1976
ESO:
VLTI
2004 -
Georgia State Univ.:
CHARA
1995 -
Ryle:
Nobel prize
Aperture synthesis
Radio astronomy
1974
Univ. of Cambridge:
Aperture synthesis for optical interferometry
1995
1950
1960
1970
1980
1990
2000
2010

Figure 1.6: Timeline of the important contributions to stellar interferometry. In this figure, only a sample of the modern existing facilities is represented

1.3 Stellar intensity interferometry

1.3.1 Retrospective on intensity interferometry

The intensity interferometer was invented by R. Hanbury Brown in 1949 to measure the angular diameters of two radio sources. His idea was to look at how much the noise of the source would be correlated when measured by two separated detectors. In this manner he would avoid the need to bring the light together to coherently interfere, thus allowing a long baseline. He sought the help of R. Q. Twiss for the mathematical theory. They measured the angular diameters of their two targets Cygnus A and Cassiopeia A. These two targets were measured again in Sydney, yielding similar results in 1952. They were surprised that their measurements seemed to not be disturbed by the atmospheric perturbations. They reviewed their model, and realised it was to be expected. In this manner, they discovered one main advantage of intensity interferometry, and decided to apply it to visible light. In fact, at that time Michelson stellar interferometry had been largely forgotten for 30 years, being strongly limited by the atmospheric perturbations, and the very high optical and mechanical precisions required to bring light together in a coherent manner. Intensity interferometry could solve both these problems.

However, at this time, the physical nature of light was not fully understood. It was then strongly doubted in the optical community that fluctuations in light could be correlated between two different receivers. However, in 1956, they wrote a paper called *Correlation between photons in two coherent beams of light* [20] where they experimentally proved their opponents wrong. This paper permitted the formulation of the Hanbury Brown and Twiss effect (HBT effect), which is that fermions are anti-correlated in time and space while bosons are correlated. Later on, it largely contributed to the field of particle physics. In 1962, they received funding for their project and started building the intensity interferometer at Narrabri in Australia. The general layout can be seen in Figure 1.3, it was composed of two reflectors of roughly 6.5 m size mounted on a circular track of 188 m diameter. The telescope diameters were larger than any other optical telescopes at that time. In fact, one of the challenges of intensity interferometry is the difficulty to obtain a sufficient SNR. Therefore, large light collectors are required while, on the other hand, high optical precision is not needed, and the reflector can be made out of simple and cheap mirrors. The reflectors were indeed composed of a mosaic of 252 hexagonal glass mirrors of $\approx$ 38 cm side length. The telescopes could then be moved along the circular tracks to vary the baseline. Photomultiplier tubes were used as detectors at the foci of the reflectors. Finally, the detectors were connected to a multiplier which computed the correlation functions. From 1965 to 1972, they measured angular sizes of 32 stars of spectral types O to F. They investigated close binary stars, the effect of limb darkening, polarization and rotation. They also established an effective temperature scale for hot stars that is still used today [21].

Hanbury Brown wanted to build a new intensity interferometer. He envisioned a better instrument and proposed a new model of an intensity interferometer that would involve a significant improvement [22]. However this was never achieved, as the then revived interest for Michelson stellar interferometry showed greater promise. As a consequence, the Narrabri interferometer would remain the only intensity interferometer used for optical astronomical observations. In other fields of physics, such as in particle physics, the Hanbury Brown and Twiss effect is being extensively used, having produced thousands of publications since it started to be used.

1.3.2 The potential of intensity interferometry

The different strengths and weaknesses of intensity interferometry are compared to the ones of amplitude interferometry in Table 1.1.

	Amplitude Interferometry	***Intensity Interferometry***
Signal	Optical → cannot be divided indefinitely → only few baselines possible → low interferometric-plane coverage High SNR	Electronic → can be copied → many baselines possible → Very good interferometric-plane coverage possible Poor SNR → need large flux collectors
Mechanical precision	High → baseline limited → expensive reflectors → better for longer wavelengths	Low → very long baseline possible ⟶ **very high resolution possible** → low cost reflectors → not problem for short wavelengths ⟶ even higher resolution
Correlation	Amplitude/phase → phase measured → image possible to retrieve	Intensity (amplitude squared) → phase lost → image hard to retrieve Immune to poor seeing
Source requirement	Cool and faint stars	Hot and bright stars → Long exposure times

Table 1.1: Amplitude interferometry vs. Intensity interferometry, pros and cons.

The key point is that, intensity interferometry has low precision requirements for its equipment. Firstly, it means that in terms of costs, it falls below any other high resolution instrument in the optical. Secondly, it means that the error budget is greatly relaxed, allowing kilometer-long baselines, a dream that is not close to be achieved with Michelson-type interferometry in the visual. Thirdly, since all signals are carried electronically, intensity interferometry would today rather be a software instrument such as it is done in radio astronomy, i.e., LOFAR. This implies that very many baselines can be used, allowing a large interferometric plane coverage and thus a high image reconstruction potential for aperture synthesis. Finally, intensity interferometry uses very fast detectors and the intensity fluctuations measured are of the order of nanoseconds if not shorter (this is not the exposure time, but the speed of the detector for measuring the number of incoming photons), thus it is not affected by the much slower atmospheric disturbances.

Although intensity interferometry offers a potential for kilometer-scale interferometry, opening new resolution windows for stellar surface imaging, it is constrained to observing hot stars (typically hotter than the Sun) of small angular extent. It will therefore not replace the classical amplitude-phase interferometers in observing cool or faint objects.

1.3.3 The Cherenkov Telescope Array: An opening for intensity interferometry

In a much more energetic part of the electromagnetic spectrum, an international collaboration is currently working on the erection of a large array of air Cherenkov telescopes, the so-called Cherenkov Telescope Array (CTA) [23]. Extraterrestrial gamma radiation cannot be directly detected from earth due to the atmospheric absorption at these energies. However, when highly energetic gamma photons enter the atmosphere, they induce chain reactions resulting in showers of particles. These particles travel at a very high speed and can produce Cherenkov light flashes in air. The so-called Cherenkov light is indeed a shock wave phenomenon that happens when a particle travels at a speed higher than light speed in a medium. Cherenkov light typically lies in the blue and UV wavelength range, which is why it can be detected by optical telescopes. However the flashes are very rapid and faint, thus they need very large dishes to be observed as well as fast detectors. If several telescopes are used, the location of the gamma radiation can be traced; for this task low-cost mirrors are sufficient, but many of them are needed.

It turns out that the optomechanical qualities of Cherenkov telescopes match the requirements for also intensity interferometry. This fact, together with advances in detectors alerted a small community of astronomers who concluded that a revival of stellar intensity interferometry could be possible. Indeed, the new Cherenkov Telescope Array will work as an observatory (not only an experiment), permitting applications for different types of observations.

An artis's view of one of the two sites of the Cherenkov Telescope Array is shown in Figure 1.7. There is planned one array of 1 km^2 in the Northern, and one of 3 km^2 in the Southern hemi-

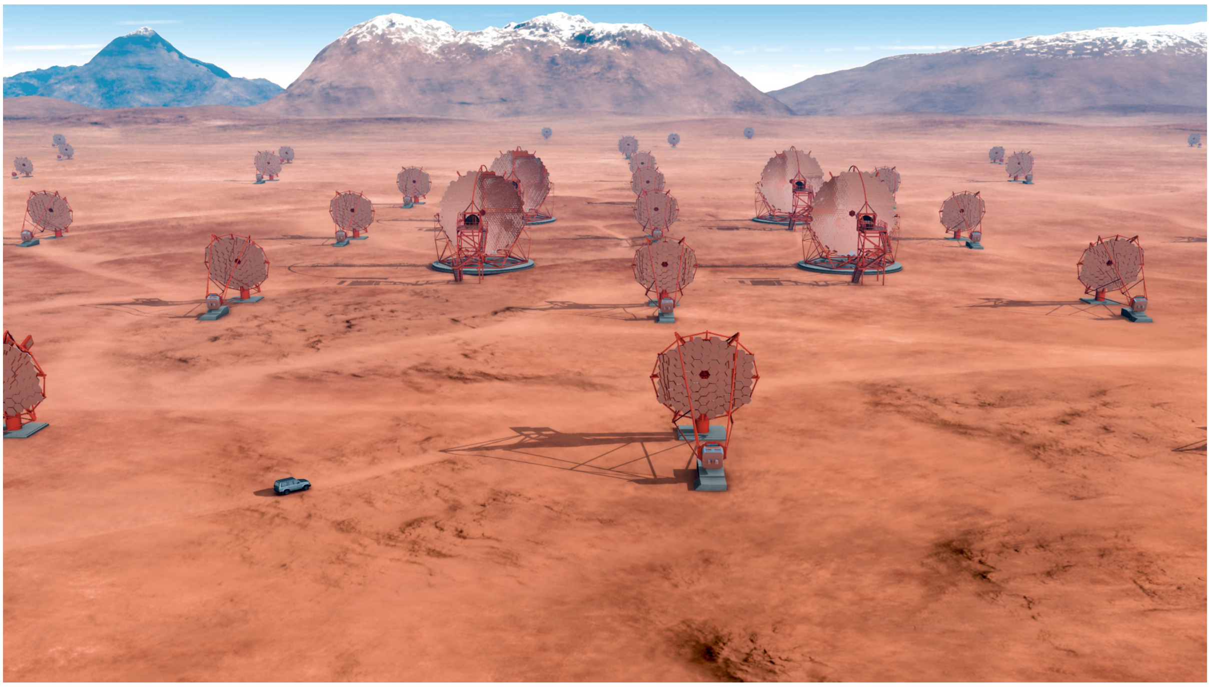

Figure 1.7: An artist's impression of the southern Chenrenkov Telescope Array. The array will be composed of very many large (24 m), medium (12 m) and small (6 m) telescopes spanning over 3 km^2. The telescopes will be low-cost large light collectors made of many mirror segments. Image from CTA website [23].

sphere to cover the full sky. Both arrays will be composed of telescopes of three different sizes; the large size telescopes (LST) of 24 m, the medium size telescope (MST) of 12 m and the small size ones of around 6 m aperture. The locations of the arrays are currently still under discussion.

This is a summary of what the Cherenkov Telescope Array will offer for stellar surface imaging by intensity interferometry:

∗ *Large optical light collectors.*
∗ *Large array of telescopes of kilometer-scale enabling milli- to microarcsecond resolution.*
∗ *Many telescopes implying many baselines that almost fully cover the interferometric plane.*
∗ *Complete sky coverage from northern and southern sites.*

Furthermore, the arrays are expected to be used for Cherenkov light detections during the darker nights, while intensity interferometry can also be performed during nights with full moon. For this reason, intensity interferometry should have an advantage in obtaining observation times during such bright nights.

Figure 1.8 shows the potential of stellar intensity interferometry (SII) using the Cherenkov telescope array, compared to the current highest angular resolution imaging instruments in the optical.

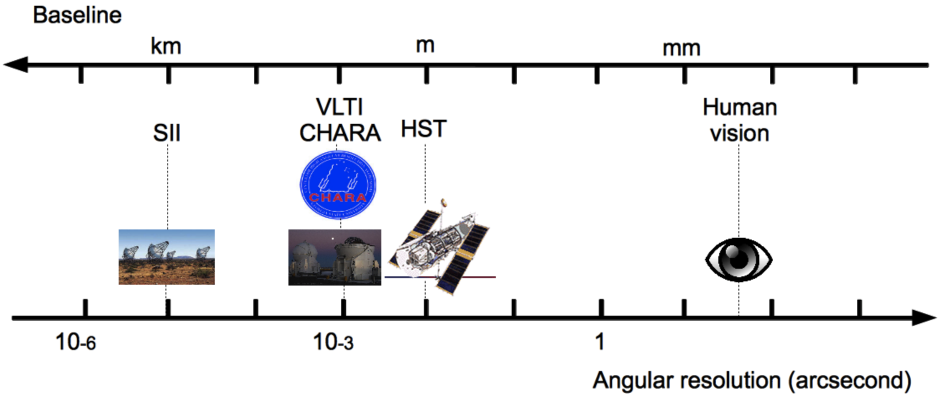

Figure 1.8: Potential angular resolution that the Cherenkov Telescope Array could achieve if used as a Stellar Intensity Interferometer (SII).

1.3.4 Previous simulations

Computer simulations of observations were performed by H.Jensen in the context of his master thesis [24]. At the time of his work, the CTA configuration was not yet defined. Several candidates in Figure 1.9 were proposed.

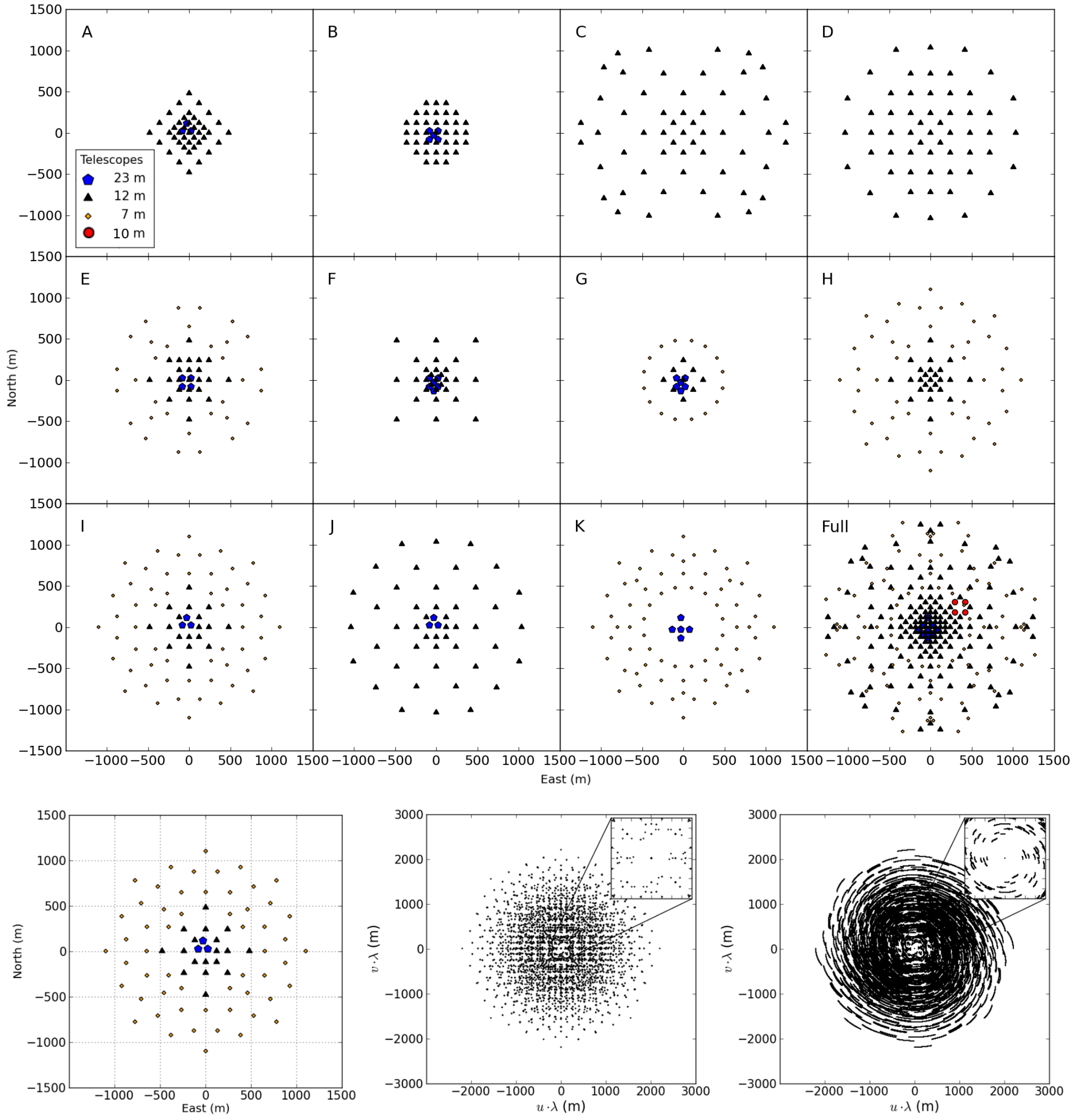

Figure 1.9: Top: Different CTA configurations originally suggested.
Bottom: Interferometric-plane coverage for configuration I, as the target star moves in the sky due to the rotation of the Earth. Left image shows the configuration, middle image shows a snapshot of the interferometric-plane at an instant when the star is at the zenith, right shows the plane coverage for the star moving from zenith to 20 degree west. Figure from [2].

In his work, H. Jensen noticed that all these configurations can be put in three different categories; configurations with dense baselines of short sizes (A, B, F and G), configurations with telescopes spread over larger areas (C, D and J) and finally configurations with both short and large baselines (E, H, I and K). Today it is expected that the South array will be of configuration E, and the North Array will be similar but smaller. It was shown that this category of arrays is also the best suited for intensity interferometry. It allows both long and short baselines, thus an almost full interferometric-plane coverage taking into account the Earth's rotation, Figure 1.9 (bottom). The special configuration I, similarly to E, offers more telescopes and more importantly more unique baselines. It spans angular scales between 0.06 mas and 1.4 mas.

Following that, numerical simulations were performed for the configuration on an image test Figure 1.10. The following parameters of simulation were used; the star was moving from zenith to 50^o west with steps of 5^o, the integration time was of 2h for each steps, the wavelength was 500 nm with a bandpass filter of 1 nm, the detector had 1 ns time resolution and 70% quantum efficiency. The results are shown in Figure 1.11.

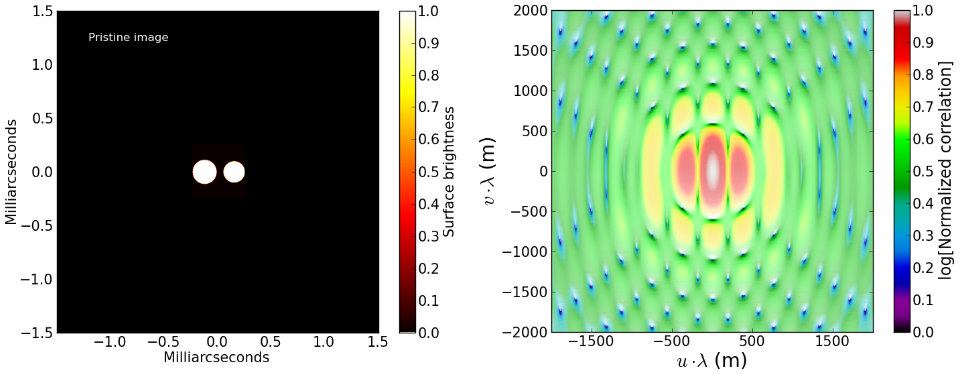

Figure 1.10: Pristine image used for the simulation (left) with it's Fourier magnitudes (right). Figure from [2]

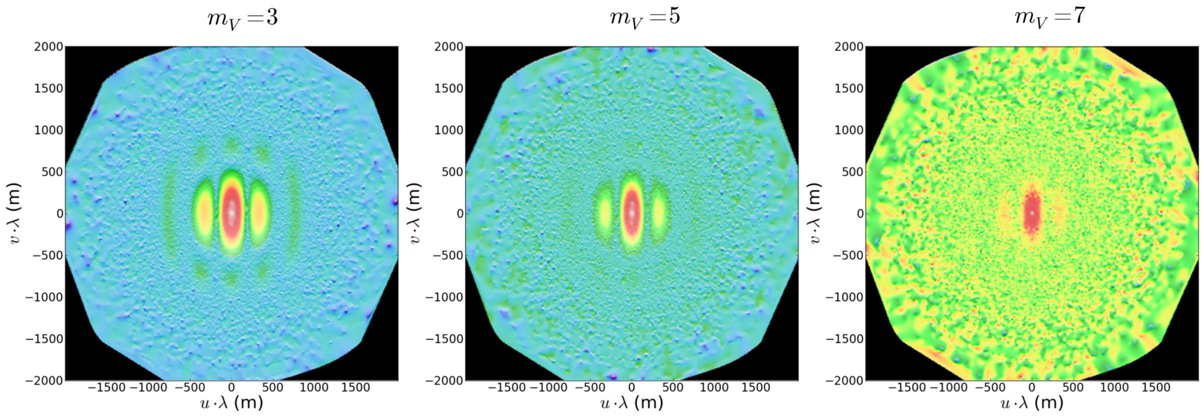

Figure 1.11: The simulated Fourier magnitudes for the pristine image Figure 1.10 and for different apparent magnitudes m_V. Figure from [2]

The simulations highlighted that both high and low frequency Fourier components are resolved with the type of array E (high frequency in the Fourier plane corresponds to short distance scales and low frequencies to large distance scales). However, this configuration uses more small size telescopes than the other configurations which makes the results more sensitive to the apparent magnitude of the star.

The results from an intensity interferometer only contain the absolute Fourier magnitudes and not the phase, which is necessary for conventional interferometric image reconstruction. Algorithms have been worked out to retrieve phase information and produce images with intensity interferometry. Paul Nuñez et al. [25] use Cauchy-Riemman phase recovery techniques to reconstruct images. Example of image reconstructions can be seen in Figure 1.12 for binaries of different size ratios.

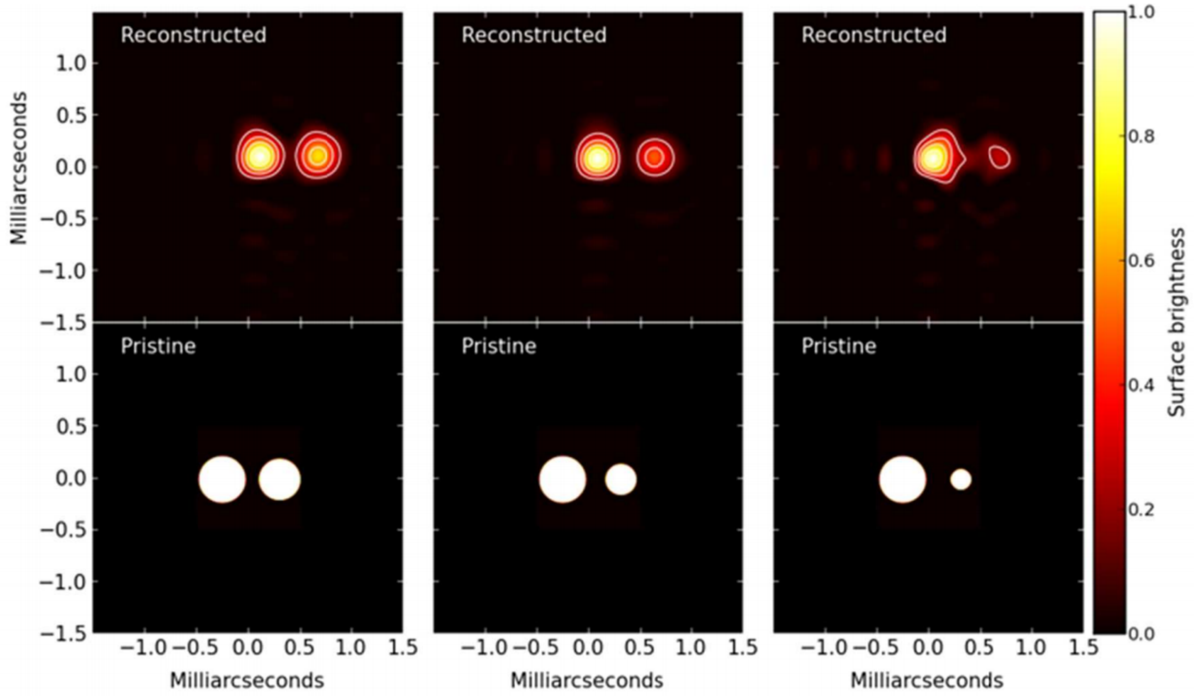

Figure 1.12: Image reconstruction for simulated binaries, figure from [24]

In this context, the present thesis project stands as one of the necessary steps between the theory and the reality. The main goal is to verify experimentally that a revival of intensity interferometry is possible with the new technologies, e.g., single-photon counting detectors and digital data processors. Furthermore, it is intended to gain experience in carrying out intensity interferometry with a CTA-like array configuration and eventually to understand the potential limitations existing or the instrument optimizations that could be desirable.

Chapter 2

Optical coherence theory

This chapter presents the theory of optical coherence necessary for understanding the physics behind interferometry. The theory of Michelson stellar interferometry is used as reference as it is the "orthodox" way of doing stellar interferometry. The theory of intensity interferometry is then developed. This chapter was written with the help of the three following books; *Fundamentals of photonics, 2nd edition* by B.E.A. Saleh and M.C. Teich [26], *An introduction to Optical Stellar Interferometry* by A. Labeyrie, S.G. Lipson, P. Nisenson [27], and *The intensity interferometer* written by R. Hanbury Brown himself [22].

2.1 Diffraction of light

Light passing through an aperture in an opaque material undergoes diffraction. It means that the light interacts with the edges of the aperture, a result of the light propagating as a wave. Huygens' principle allows an analysis of this effect by describing each point on a wave front as a secondary emitting source. The resulting wave is the sum of all these secondary sources. Close to the aperture, it has a very complex structure. However far from it, it can be approximated as a plane wavefront, permitting an easier analysis. The diffraction pattern is the intensity distribution observed on a screen after the light has been diffracted. In the far field, i.e., far from the aperture, the diffraction is what is called Fraunhofer diffraction. In this configuration, the diffraction pattern is the absolute square of the Fourier transform of the aperture.

Let us define the complex amplitude of the wave incident to the aperture in the plane of the aperture (x, y) as $U_i(x, y)$ and the amplitude after the aperture $U_a(x, y)$ then:

$$U_a(x,y) = p(x,y)U_i(x,y), \tag{2.1}$$

with

$$p(x,y) = \begin{cases} 0 & \text{if inside the aperture} \\ 1 & \text{if outside the aperture} \end{cases} \tag{2.2}$$

called the aperture function. The final complex amplitude at the screen is $U_s(x, y)$ which is $U_a(x, y)$ undergoing propagation in free space. It is equal to:

$$U_s(x,y) = CU_i(x,y) \int_{-\infty}^{\infty} \int_{-\infty}^{\infty} p(x,y) e^{i2\pi(\nu_x x + \nu_y y)} dxdy \tag{2.3}$$

where $\int_{-\infty}^{\infty} \int_{-\infty}^{\infty} p(x,y) e^{i2\pi(\nu_x x + \nu_y y)} dxdy$ is the Fourier transform of $p(x, y)$, the aperture function. $\nu_x = x/\lambda d$ and $\nu_y = y/\lambda d$. d is the distance between the aperture and the screen. C is a constant and is equal to $\frac{i}{\lambda d} e^{-ikd}$ and $U_i(x, y) = \sqrt{I_i(x, y)}$ I_i is the intensity incident to the aperture.

Finally, the diffraction pattern is given by

$$I(x,y) = |U_s(x,y)|^2 \tag{2.4}$$

Thus the intensity pattern observed at a distance d is:

$$I(x,y) = \frac{I_i}{(\lambda d)^2} | \int_{-\infty}^{\infty} \int_{-\infty}^{\infty} p(x,y) e^{i2\pi(\nu_x x + \nu_y y)} dxdy|^2 \tag{2.5}$$

Integrating $p(x,y)$ is equivalent to integrating over the surface of the aperture; as a consequence, there is a direct relation between the dimensions of the diffraction pattern and the dimension of the aperture.

It is possible to derive this expression for different types of apertures. Some of particular interest for this thesis are the circular, the elliptical and the double aperture.

Circular aperture:

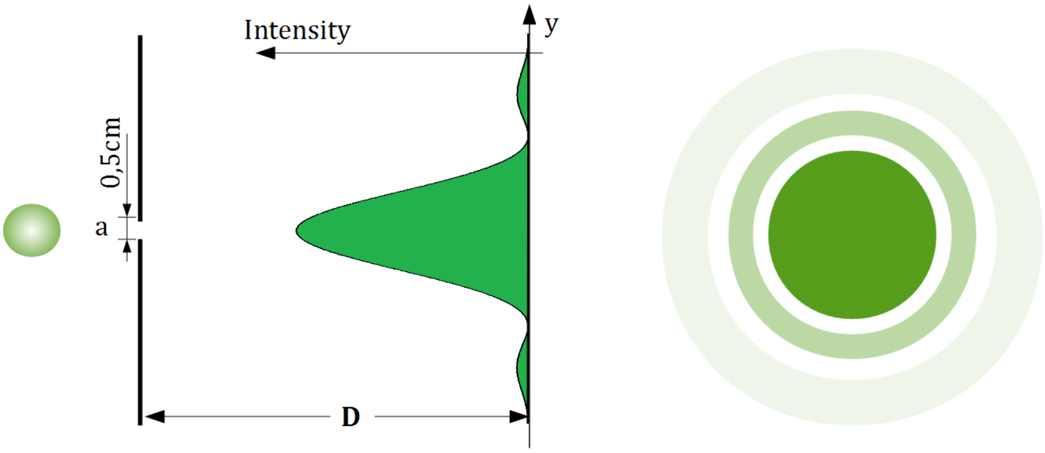

Figure 2.1: Diffraction patterns. Left: For a single aperture in 1D (circular rectangular, ...); a is the aperture size, D the distance to the screen. Right: Airy pattern for a circular aperture.

For the circular aperture, the intensity distribution is known as the *Airy pattern*, which is composed of one central blob of high intensity and surrounded by rings of decreasing intensity. The first minimum of intensity is found with:

$$y_{min} \approx \frac{\lambda D}{a} \tag{2.6}$$

Elliptic aperture:

The diffraction pattern in 1D is the same as the one in Figure 2.1 [Left], but the elliptical slit is not circularly symmetric, but possesses a long axis and a short axis, which have different radii. Similar to the aperture, the diffraction pattern will be elongated or stretched in different radial directions. One property of the Fourier transform is that a stretch in the frequency domain results into a compression in the spatial domain and vice versa. Thus, the diffraction pattern will appear more extended in the direction corresponding to the short axis of the elliptical aperture and smaller in the direction of its long axis.

Double aperture:

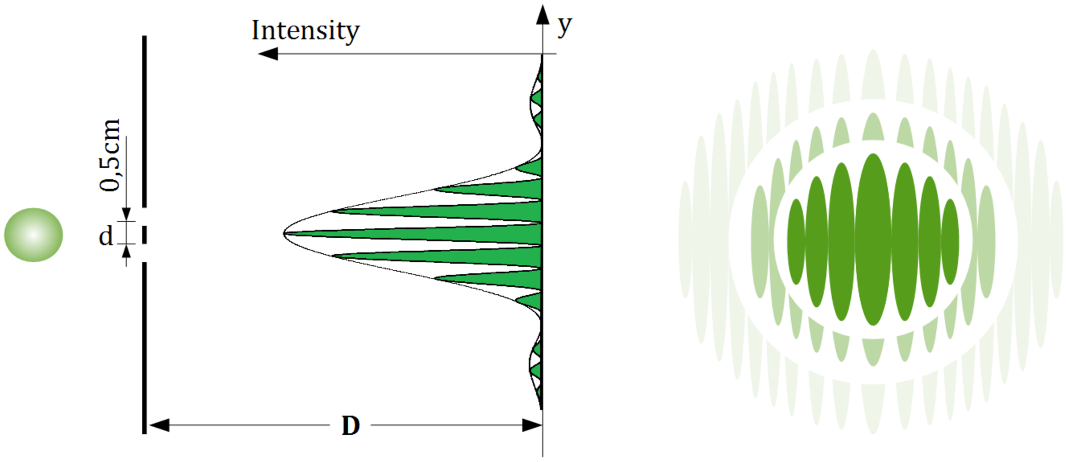

Figure 2.2: Diffraction and interference pattern. Left: For a double aperture in 1D; d is the aperture separation, D the distance to the screen. Right: Interference and Airy patterns become superimposed for a double circular aperture.

Another interesting property of the Fourier transform is its additive property. The Fourier transform of a double aperture will thus be the superposition of the Fourier transform of each aperture. If the apertures are of exactly same dimensions, then the pattern will have the same extent as from a single aperture in terms of the intensity distribution. However, a result of wave optics is that by superposing two waves, interference will occur. Thus, in the plane image, one observes an interference pattern analogous to the Airy pattern of one aperture. The extent of the Airy pattern can be found as previously, and the scale of the interference fringes can be found as follows:

$$y_{fringe} \approx \frac{\lambda D}{d} \tag{2.7}$$

with d the aperture separation, and y_{fringe} the separation between the two first fringes.

Rayleigh criterion

Diffraction is of importance for optical imaging system as it sets a limit in the imaging. What was discussed previously holds for the Fraunhofer condition, ie., very far away from the aperture. In a classic optical system, the image is formed at the focus of the optical elements, in which case the Fraunhofer diffraction also applies. Since a lens or a mirror does not have infinite dimension, it is practical to picture them as infinite objects limited by an aperture. The edges of the aperture diffract light of an incoming object. For a perfectly circular aperture (which is most of the time the case), the diffraction will be the Airy pattern seen previously. Thus, each point in the object does not produce a perfect point in the image plane, but rather an Airy pattern blob. Thus, the dimension y_{min} in Equation 2.6 represents the minimum "point-image" size that can be obtained through a lens/mirror of a certain diameter a. This leads to what is called to the Rayleigh criterion which defines how fine details can be imaged by an optical system. As for the Fraunhofer diffraction, the image of an extended object is the image obtained through geometrical ray optics (which can be called "perfect image"), but is the convolution of this image with the Fourier transform of the aperture.
The Rayleigh criterion, also called diffraction limit is given in Equation 1.1.

2.2 The coherence of light

The previous discussion assumes perfectly monochromatic and coherent waves but most light sources are neither monochromatic nor perfectly coherent. Basically, the coherence of a source relates to how predictable/stable it is or, in other words, how close to a pure sinusoidal its wavefunction is. Incoherence in most light sources comes from the fact that light is emitted independently from a large number of atoms at different frequencies, or for the case of extended sources, at different points of space. Light can be qualified as coherent (a laser has high coherence), partially coherent, or random (white light is random). Three aspect of the first-order coherence can describe a light source: the polarization coherence, the temporal coherence and the spatial coherence. The common way of studying coherence is to divide a light source into two waves and compare these two. Two exactly equal waves define a perfectly coherent source while two strongly divergent waves define an incoherent source. Usually, the coherence is normalized to 1 for the case of coherence and tends to 0 for random light. That being said, the normalized polarization coherence would be equal to 1 if the polarization of the two waves are parallel and 0 if they are perpendicular (taking any value between 0 and 1 for other inclinations relative to each other). The temporal coherence would be 1 when the two waves have equal frequencies, and will tend to 0 for large difference in frequency. And finally, the spatial coherence will be 1 for the wave vectors equal for the two waves and tend to 0 for large wave vector difference. Light can then be classified as coherent, incoherent (or random), or partially coherent.

In the following, a description of light in terms of temporal and spatial coherence is given. The polarization coherence is not considered just now although it is important, and will be considered for the later discussion. In fact it is straightforward what it represents from the understanding of spatial and temporal coherence, but its analysis is not required within the scope of this thesis.

2.2.1 Temporal coherence

The first-order temporal coherence of a source is, as hinted before, directly linked to its spectral purity. Most light sources that are encountered do not possess a unique frequency ν but rather a distribution of frequencies ν_i referred as a spectrum with a spectral width $\Delta\nu$. For the case of quasi-monochromatic thermal light, the spectrum is often thermally Doppler broadened, characterized by a Gaussian distribution with a broad spectral width. The spectrum can be defined as $S_s(\nu)$ with $S_0(\nu)$ its envelope and $\Delta\nu$ its spectral width which is the FWHM of $S_s(\nu)$, Figure 2.3. Because of the many different frequency components, the resulting wavefront shows abrupt phase jumps in time, meaning that if a thermal wave would be compared to itself with a certain time delay, it would most certainly be different and thus classified as incoherent.

The coherence time is defined as:

$$\tau_c \approx \frac{1}{\Delta\nu} \tag{2.8}$$

It corresponds to the time interval within which the light is temporally coherent. Lasers have large τ_c up to some μs, while white light has very short τ_c, in the order of fs.

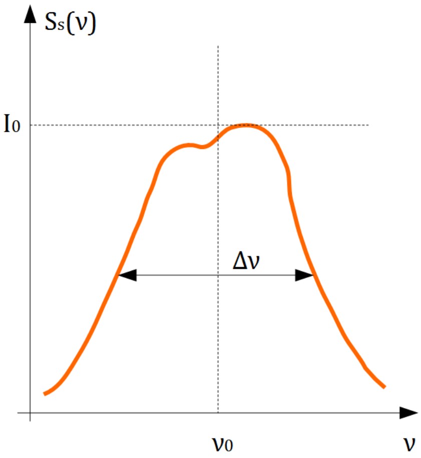

Figure 2.3: A spectrum density function. Polychromatic light is composed of very many frequencies. I_0 is the peak intensity, $\Delta\nu$ is the spectral width, ν_0 is the central frequency.

Let us define the coherence mathematically. If $U(t_i)$ is the wave function measured at the time t_i, the first-order coherence is defined as

$$G^{(1)}(t_1, t_2) = \langle U^*(t_1)U(t_2)\rangle\,, \tag{2.9}$$

where $\langle\rangle$ denotes the average for a period of time typically longer than λ/c but shorter than $t_2 - t_1$, and U^* is the complex conjugate of U. Mathematically, the coherence is the correlation between U at different times. In order to practically measure $G^{(1)}$ one needs to compare a wave at different times t_1 and t_2. One way of doing that is using a Michelson interferometer as in figure 2.4. A 45^o semi-transparent mirror splits the light along two arms, where in one arm a time delay is added by moving a mirror. The two waves are then recombined and physically, they interfere. When the time delay lies within the temporal coherence, the two waves are coherent and they interfere with a "perfect" contrast between bright and dark fringes. In the opposite case, the resulting interference pattern (also called interferogram) is blurry or does not exist. The contrast between bright and dark fringes in this case defines the first order coherence.

It is practical to define a normalized first order coherence:

$$g^{(1)}(t_1, t_2) = \frac{G^{(1)}(t_1, t_2)}{G^{(1)}(t_1 = t_2)} = \frac{G^{(1)}(t_1, t_2)}{\langle U^*(t_1)U(t_1)\rangle}. \tag{2.10}$$

Equation 2.10 can be rewritten with the time delay $\tau = t_2 - t_1$:

$$g^{(1)}(\tau) = \frac{G^{(1)}(\tau)}{G^{(1)}(0)} = \frac{\langle U^*(t)U(t+\tau)\rangle}{\langle |U(t)|^2\rangle} \tag{2.11}$$

Figure 2.5 shows $g^{(1)}(\tau/\tau_c)$ for light with three different spectral distributions. The temporal coherence is the width of $g^{(1)}$. For an ideal laser $\Delta\nu = 0$, $\tau_c = \infty$. However in a realistic case $\Delta\nu$ is of course finite, for instance a single-mode He-Ne laser has its spectral width on the order of the MHz giving a temporal coherence of some microsecond, from the perspective of a photon this is very long! For a typical broadband thermal light, such as the filtered sunlight, τ_c lies in the femtosecond range.

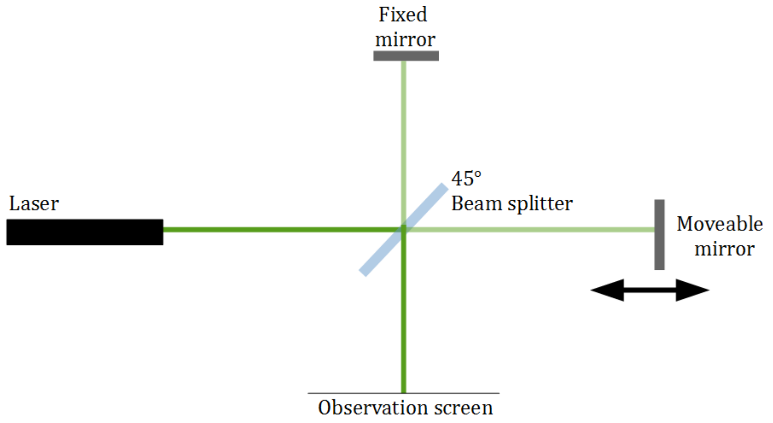

Figure 2.4: A Michelson interferometer to measure the temporal coherence. The light is directed onto a beamsplitter which splits it into two arms. The beams are reflected on mirrors and recombined at the beam splitter. One of the arms has an adjustable length, which introduces a time delay in one of the beams. It is possible to find the temporal coherence by looking at the contrast of the fringes obtained on the screen as a function of the time delay.

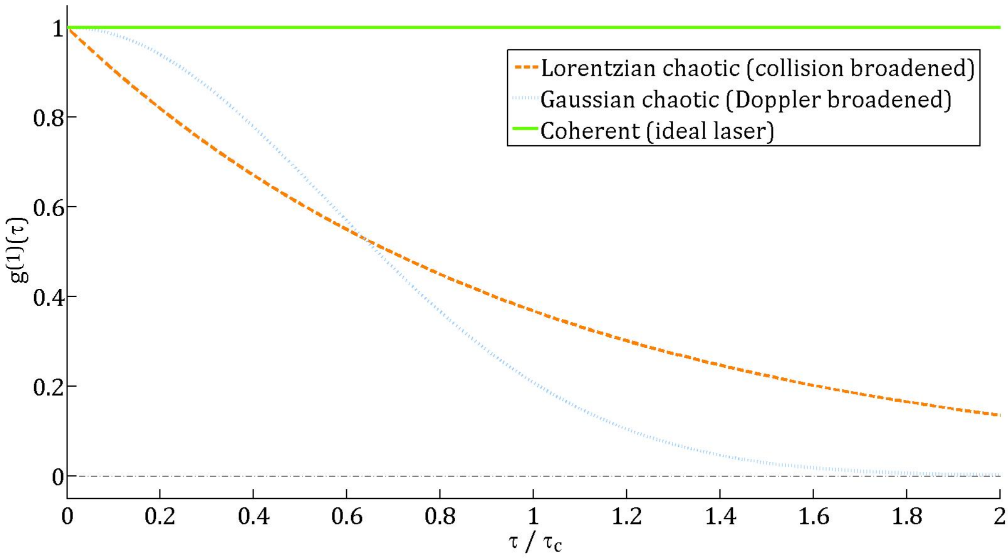

Figure 2.5: First-order temporal coherence for three different types of light.

There also exists a second-order coherence (and indeed many more). It is expressed as:

$$g^{(2)}(t_1, t_2) = \frac{\langle U^*(t_1)U^*(t_2)U(t_1)U(t_2)\rangle}{\langle |U(t_1)|^2\rangle\langle |U(t_2)|^2\rangle}, \tag{2.12}$$

which can also be simplified as:

$$g^{(2)}(\tau) = \frac{\langle |U(t)|^2|U(t+\tau)|^2\rangle}{\langle |U(t)|^2\rangle\langle |U(t)|^2\rangle} = \frac{\langle |U(t)|^2|U(t+\tau)|^2\rangle}{\langle |U(t)|^2\rangle^2}, \tag{2.13}$$

and with the intensity:

$$I(t) = \langle |U(t)|^2\rangle, \tag{2.14}$$

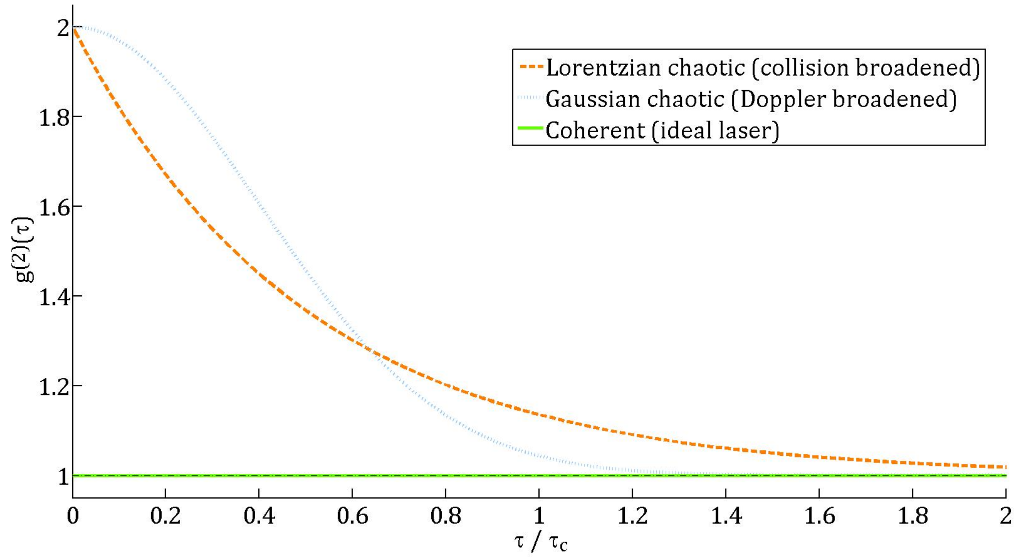

Figure 2.6: Second-order temporal coherence for three different types of light.

it becomes:

$$g^{(2)}(\tau) = \frac{\langle I(t)I(t+\tau)\rangle}{\langle I(t)\rangle^2}, \tag{2.15}$$

This is the quantity involving intensities of light that is measured in an intensity interferometer, also the basis for its name. Thus, the second-order coherence deals in comparing intensities and not amplitudes, and there is no information retained about the phases of the waves. Figure 2.6 shows $g^{(2)}$ for different theoretical light sources. The curves are reminiscent of those for the first-order coherence in figure 2.5. In fact, in the case of chaotic light (which has a Gaussian distribution of its instantaneous electric field amplitudes), $g^{(1)}$ and $g^{(2)}$ relate to each other as follow:

$$g^{(2)}(\tau) = 1 + |g^{(1)}(\tau)|^2 \tag{2.16}$$

2.2.2 Spatial coherence

Spatial coherence is very similar to temporal coherence. Indeed the same analysis can be conducted by replacing t_i by r_i in the previous equation, with r_i a position in the observation plane. Thus, spatial coherence is measured by comparing waves at two different positions in space. While the temporal coherence is linked to the spectral extent, the spatial coherence is linked to the spatial extent of the source. One can immediately see how the spatial coherence becomes a tool for measuring angular diameters, and this is the basis for stellar interferometry. The light from a star is collected at two different points in the observing plane. The two resulting waves can then be "compared". Measuring spatial coherence of light from different stars permits to find their angular diameters; see Section 2.4.4 *Interference of temporally coherent beams of light*.

2.2.3 Interference of spatially coherent beams of light

Figure 2.7 shows a Young's slit experiment. A light source is divided into two beams by means of two slits. The left side of the figure shows the case for a point source, ie., spatially coherent. The amplitude in M on the screen at time t is:

$$U_M(t) = c_1 U_1(t) + c_2 U_2(t+\tau), \tag{2.17}$$

where c_1 and c_2 are two complex amplitude transmission factors that contain information such as the size of the slits, the distance to the screen, the phase and amplitude of the diffracted beams, while τ is the time delay between the arrival from points 1 and 2. With equation 2.4, the intensity in M is the time average:

$$I_M = \langle U_M^*(t) U_M(t) \rangle, \tag{2.18}$$

By plugging in Equation 2.17 it becomes:

$$I_M(\tau) = |c_1|^2 I_1 + |c_2|^2 I_2 + 2\Re[c_1^* c_2 \langle U_1^*(t) U_2(t+\tau)\rangle] \tag{2.19}$$

Thus, the intensity in M is the sum of the intensities in 1 and 2 plus one additional term. One recognizes this the first order coherence $G^{(1)}(\tau)$ from Equation 2.9. By replacing the normalized $g^{(1)}$ in this last equation, and by simplifying $|c_i|^2 I_i = I_i'$:

$$I_M(\tau) = I_1' + I_2' + 2\sqrt{I_1' I_2'}\Re[g_{12}^{(1)}(\tau)] \tag{2.20}$$

where the indexes 1 and 2 stand for the first-order coherence between 1 and 2, also called the **mutual coherence**. The result shows that an interferometer system of the Young's slit type, such as in Figure 2.7, also allows one to study the coherence of the light source.

For the special case of temporal and spatial coherence, $U_i(t)$ can be written:

$$U(t) = e^{i\phi(\nu) - 2\pi\nu t} \tag{2.21}$$

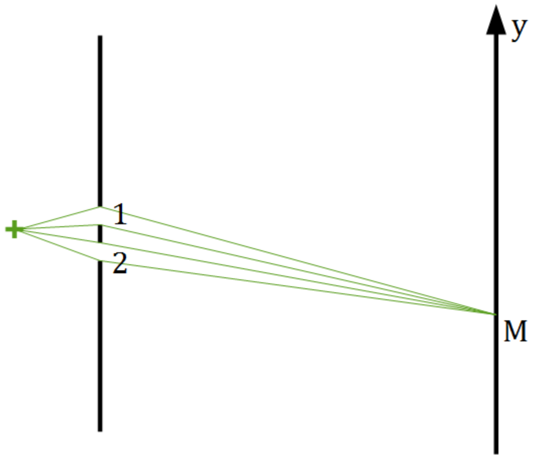

Figure 2.7: Configuration for interference of spatially coherent light. The source is a point source, its light divided by two slits. At one point M on the screen is the combination of the two beams.

Equation 2.19 becomes:

$$I_M(\tau) = I_1' + I_2' + 2\sqrt{I_1' I_2'} cos(2\pi\nu c\tau) \tag{2.22}$$

In the case of temporally incoherent light, the light is not monochromatic, but possesses a spectrum density as in Figure 2.3. Thus I_M becomes dependent on ν:

$$I_M(\tau,\nu) = S_s(\nu)[I_1' + I_2' + 2\sqrt{I_1' I_2'} cos(2\pi\nu\tau)], \tag{2.23}$$

and one needs to integrate over ν in order to find $I_M(\tau)$:

$$I_M(\tau) = \int_0^\infty I_M(\tau,\nu) d\nu \tag{2.24}$$

$$I_M(\tau) = (I_1' + I_2') \int_0^\infty S_s(\nu) d\nu + 2\sqrt{I_1' I_2'} \int_0^\infty S_s(\nu) cos(2\pi\nu\tau) d\nu \tag{2.25}$$

$S_s(\nu)$ is always positive and real, thus it can be written:

$$\int_0^\infty S_s(\nu) cos(2\pi\nu\tau) d\nu = \Re[\int_0^\infty S_s(\nu) e^{-2i\pi\nu\tau} d\nu] = \Re[\tilde{S}_s(\tau)] \tag{2.26}$$

with $\tilde{S}_s(\nu)$, the Fourier transform of $S_s(\nu)$.
One notices that $\int_0^\infty I_M(\tau,\nu) d\nu = \Re[\tilde{S}_s(\tau = 0)]$ and $I_M(\tau)$ becomes:

$$I_M(\tau) = I_1' + I_2' + 2\sqrt{I_1' I_2'} \frac{\Re[\tilde{S}_s(\tau)]}{\Re[\tilde{S}_s(0)]} \tag{2.27}$$

which gives another definition of the coherence:

$$g^{(1)}(\tau) = \frac{\Re[\tilde{S}_s(\tau)]}{\Re[\tilde{S}_s(0)]} \tag{2.28}$$

This shows that the degree of temporal coherence is directly linked to the Fourier transform of the spectral density for the optical difference at M. The normalization permits to have a perfect temporal coherence in the case of pure monochromatic light.

2.2.4 Interference of temporally coherent beams of light

This section now deals with light which originates not from a point source but an extended one. To simplify the analysis, it is assumed that it is now temporally coherent. Such a source is represented by Figure 2.8. To fulfil these conditions, one needs to assume that the source is very far away, so that the light rays form small angles. It is also assumed that M is equidistant from the slits 1 and 2; thus there is no time delay τ, and that the source is monochromatic.

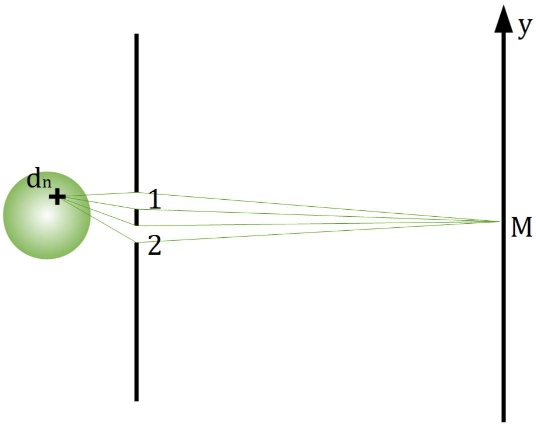

Figure 2.8: Configuration for interference of temporally coherent light. The source is extended. At one point M on the screen, light is combined from the two slits, but also from each surface element d_n on the source.

d_n is a surface element on the source. From Equation 2.19, $\langle U_1^*(t)U_2(t+\tau)\rangle$ is:

$$G^{(1)}(\tau = 0) = \langle U_1^*(t)U_2(t)\rangle \tag{2.29}$$

Let us define $U_{n1}(t)$ and U_{n2} to be the complex amplitudes at 1 and 2 due to the elementary source d_n. $G^{(1)}(\tau = 0)$ becomes:

$$G^{(1)}(\tau = 0) = \sum_n U_{n1}^*(t)U_{n2}(t) + \sum_n \sum_{m\neq n} U_{n1}^*(t)U_{m2}(t) \tag{2.30}$$

There should be no correlation between two different points on the source, thus:

$$\sum_{m\neq n} U_{n1}^*(t)U_{m2}(t) = 0 \tag{2.31}$$

Additionally, $G^{(1)}(\tau = 0)$ will vary when the distance between 1 and 2 changes and when the size of the source varies. So it is written:

$$G^{(1)}(u, v, \tau = 0) = \sum_n U_{n1}^*(t)U_{n2}(t), \tag{2.32}$$

where u, v are the coordinates of the vector between 1 and 2 in the plane of the slits (also known as the interferometric plane).

It can be shown that:

$$G^{(1)}(u, v, \tau = 0) = \int\int I(x, y)e^{-2i\pi(ux+vy)}dxdy \tag{2.33}$$

x and y are coordinates in the plane of the source.

Equation 2.33 is known as the Van Cittert-Zernike theorem. It is very important since it proves that it is possible to reconstruct an intensity map of the source ($I(x, y)$) from the mutual coherence $G^{(1)}(u, v, 0)$. For stellar interferometry it has huge consequences; it means that if a star cannot be imaged by a telescope due to the diffraction limit, its image can still be retrieved by means of interferometry. The maximum resolution achieved in such an image corresponds to the diffraction limit, not anymore set by the aperture size R but by the largest slit separation B, which is called the **baseline**.

2.3 The Michelson stellar interferometer

Michelson stellar interferometer functions similarly to the Young's slits. The principle is shown in Figure 2.10. The light from a star is collected via two primary mirrors M_1 and M_2. The two beams are then superposed on the screen where they interfere. By changing the distance between the two primary mirrors, the spatial coherence is affected and it results in a variation of contrast between the interference fringes. The contrast is thus the measure of the coherence and is written as:

$$|V_B| = |\frac{I_{max} - I_{min}}{I_{max} + I_{min}}| = g_B^{(1)}, \tag{2.34}$$

with I_{max} the maximum fringe intensity and I_{min} the minimum, $g_B^{(1)}$ is the normalised first-order coherence for B, a baseline measured in one direction of the u, v plane.

The visibility depends on B, the baseline, on the light wavelength λ and the angular size of the source θ. By measuring V_B for many different baseline, one gets a visibility curve like the ones in Figure 2.12. The curve is zero for

$$B = 1.22\frac{\lambda}{\theta}, \tag{2.35}$$

corresponding to the diffraction limit. Figure 2.12 shows the visibility curves for two stars. The largest star $\theta = 0.015$ as needs a baseline of 7.3 m to be resolved while the $\theta = 0.01$ as needs 11 m.

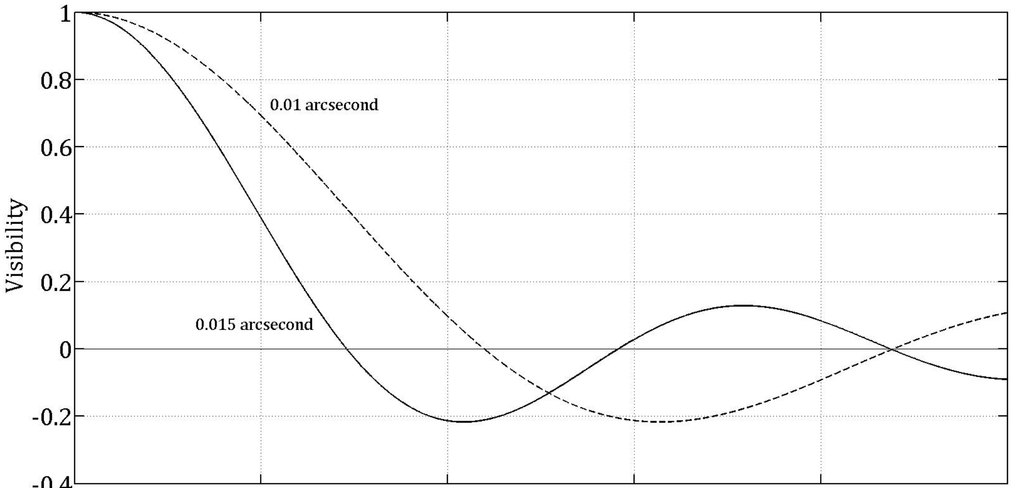

Figure 2.9: The visibility curve for two stars as a function of baseline. It is possible to measure the angular diameter by measuring the visibility for several baselines. The smaller star needs a longer baseline to be resolved.

Modern stellar interferometers are composed of independent telescopes, the light between telescopes are combined together, and transferred optically. This constitutes one of the main drawbacks of this technique. In order to obtain fringes, the light path must be controlled to subwavelength precision. For long baselines, it becomes extremely challenging so that baselines much longer than ≈ 100 m are hardly doable. Carrying the light optically poses another problem; in order to do image reconstruction, one does not only need to move two telescopes,

Figure 2.10: Principle of the Michelson stellar interferometer. Two primary mirrors (M_1 and M_2) collect starlight. The light is fetched by two secondary mirrors (M_3 and M_4) and sent to the telescope which focuses it onto a screen where interference is observed. The resolution of the system is no longer set by D, the diameter of the telescope, but by B, the baseline, which is the maximum separation between the primary mirrors. Mirror M_1 and M_2 are moveable.

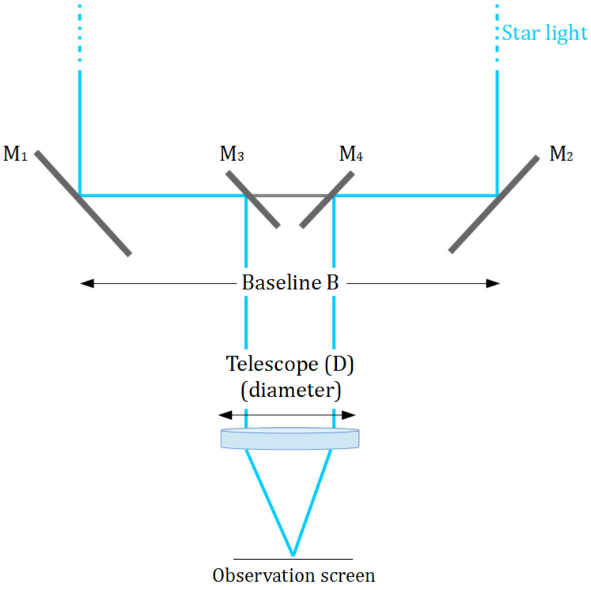

but need many of them to fill in the interferometric plane as discussed in section 2.2.4 *Interference of temporally coherent beams of light.* By increasing the number of telescopes one also needs to divide to optical signal at each telescope to obtain fringes between many different pairs of telescopes. This is done by use of beam splitters. On a practical stellar interferometer, after say 4 or 5 light divisions there is not enough photon flux left to create fringes between new pairs of detectors. Thus, the technique is limited by its number of baselines, plus by its maximum baseline which sets the resolution of the system. The atmosphere is another factor affecting the technique. Starlight travelling through the earth's atmosphere undergoes rapid phases variations, due to turbulent airflows. The visibility is severely affected by this effect.

2.4 The intensity interferometer

2.4.1 General principles

The principle of a stellar intensity interferometer is depicted in Figure 2.11. Two mirrors with independent detectors collect light from a distant star. The detectors make use of the photoelectric effect to convert photon fluxes into an electronic signal which is a measure of the intensity of the field. The two resulting signals are carried through electronic cables and are multiplied in a correlator. The intensities have rapid fluctuations that are detected by the detectors (typically they have response times on the order of nanoseconds), thus the correlation measures how correlated the fluctuations are between the two detectors. The fluctuations arise from two different phenomena, the first contribution is due to the noise in the detectors and dominates the fluctuations, while a minor contribution comes from the starlight itself and is called wave noise. This later one depends on the coherence of the source, and it is this wave noise that is of interest in intensity interferometry. Since the shot noise is not correlated between the detectors, it will not contribute to the correlation measured. However, as it dominates the noise, it decreases the correlation. It one of the reason one needs to have a high signal in intensity interferometry, indeed the correlation is a small positive product $g^{(2)}$. It is important to note that, unlike in the Michelson stellar interferometer, there is nothing interfering physically in the system. The "interference" is between electrical fluctuations.

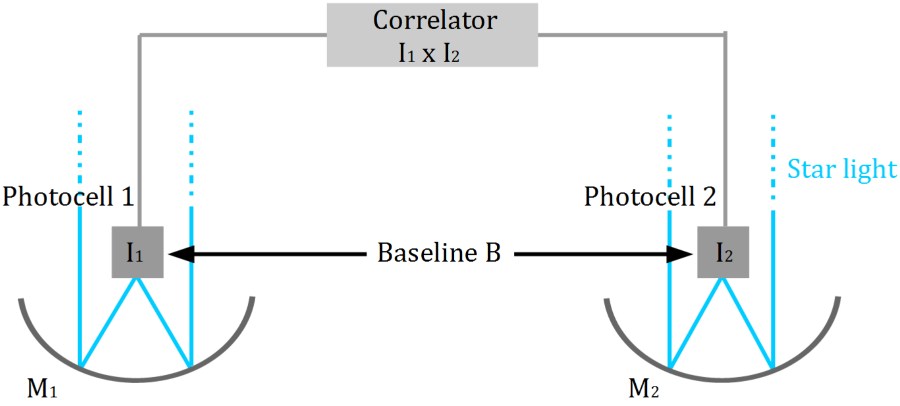

Figure 2.11: Stellar intensity interferometer. Two mirrors serve as light buckets and collect photons from a star. The intensity signal received at each photocell is converted into an electrical signal and sent to a correlator. The correlator multiplies the signal from the two detectors, providing the second-order coherence $G^{(2)}$. By changing the baseline B it is possible to retrieve a function similar to the visibility curve.

The normalised second-order coherence is:

$$|g^{(2)}(\tau)| = \frac{\langle I_1(t)I_2(t+\tau)\rangle}{\langle I_1\rangle\langle I_2\rangle} \tag{2.36}$$

with B the baseline. $I_1(t)$ and $I_2(t)$ are the instantaneous intensities measured at the detectors 1 and 2 respectively, $\langle I_1\rangle$ and $\langle I_2\rangle$ are the time averaged intensities at detectors 1 and 2. This measures the temporal second-order coherence of the source.

For the spatial coherence, the time delay is taken to be zero

$$|g_B^{(2)}(r_1, r_2, \tau = 0)| = \frac{\langle I_1(r_1, 0)I_2(r_2, 0)\rangle}{\langle I_1\rangle\langle I_2\rangle} = V_B^2 \tag{2.37}$$

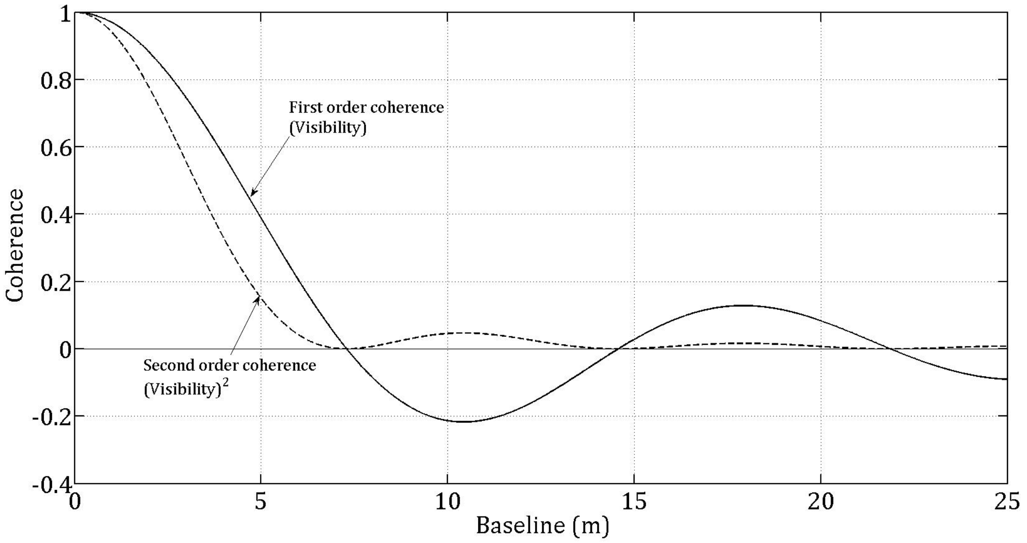

Figure 2.12: The first and second-order coherence plotted together as functions of the baseline for a 0.015 as star.

as for the Michelson stellar interferometer $g_B^{(2)}(\tau = 0)$ is measured for different baselines. The results are in the curve plotted in Figure 2.12. Similarly to the visibility, the second order correlation decreases when B increases and reaches zero for the same condition $B = \frac{\lambda}{\theta}$.

2.4.2 The signal to noise ratio

R.Hanbury Brown and R.Q.Twiss defined the SNR at the output of one of the detector as follows (Hanbury Brown and Twiss 1958):

$$(SNR)_{rms} = A\alpha n |g^{(2)}(\tau = 0)| \sqrt{\frac{\Delta f T_0}{2}}, \tag{2.38}$$

A is the telescope area, α the detector quantum efficiency, n the intensity per optical bandwidth per unit area and unit time, $|g^{(2)}(0)|$ the degree of coherence at a time delay $\tau = 0$ and for a certain baseline d, Δf the electronic bandwidth and T_0 the integration time. As a surprise it is independent of the optical passband $\Delta\nu$, provided that $\Delta\nu$ is sufficiently large. It is directly dependent on the detector performance (electronic bandwidth and quantum efficiency), and the observation constraints (observation time). Although it is dependent on the telescope area, it is not straightforward to increase the dish size, in fact, by increasing the dish size, the telescope is averaging over a larger coherence space, thus $|g^{(2)}(0)|$ may decrease. The only factor remaining is n, which is an intrinsic property of the source. To increase n one wants a bright source, but increasing the source size does not help as it also reduces the correlation, thus one wants to increase the number of photons per surface area, the only way to do that is to have a hotter star. The technique of stellar intensity interferometry is then limited to primarily hot stars. This has sometimes led to confusion as its understanding is not straightforward. Figure 2.13 shows the SNR of a stellar intensity interferometer (with some realistically assumed values for A, α, Δf, T_0 and $|g^{(2)}(0)|$) as a function of the source temperature.

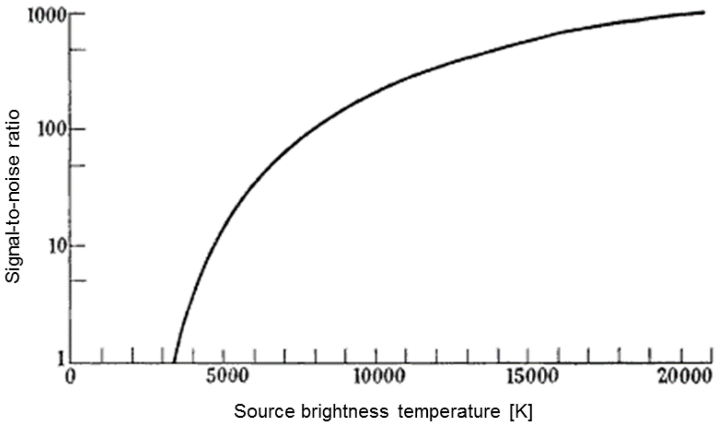

Figure 2.13: SNR achievable in intensity interferometry as function of the brightness temperature of the source. Edited image from [28]

2.4.3 Higher-order correlations

Intensity interferometry studies the second order coherence, but higher order functions can be defined in a similar manner. The third order $g^{(3)}$ is then the correlation between 3 detectors. This last one is of interest, as it would enable to obtain also the phase information otherwise lost with intensity interferometry. However $g^{(3)}$ seems to be seriously limited by SNR. The use of this order is an argument toward the use of off-line correlation, ie., not to analyse the recorded data in real time during observations, but rather make various computations afterwards. In fact, if the raw data has been stored, it will be possible to compute the correlation between any number of detectors rather than just pairs. But it is also perfectly possible to build an on-line correlator capable of calculating $g^{(3)}$.
Any higher order $g^{(n)}$ can in theory be imagined. Although such have been measured for light sources in the laboratory they have not yet been measured for any astronomical sources.

2.4.4 Quantum interpretation

Section 2.4.1 explained intensity interferometry derived from a classical representation of starlight. It is also possible to understand it from a quantum point of view, ie., by looking at the photon statistics.

In quantum mechanics, particles belong to either the fermion or the boson class. These classes are defined by their quantum statistics; fermions following the Fermi-Dirac statistics and bosons following the Bose-Einstein statistics. An example of fermions are the electrons, for which the Fermi-Dirac statistics implies that two electrons cannot occupy the same energy state. Conversely, bosons would tend to agglomerate in a single quantum state. The so-called Bose-Einstein condensate (BEC) is one beautiful example of bosons; as atoms are cooled down to their ground state, they agglomerate in a single state, resulting in a particular state of matter that is similar to a matter-wave. The formation of such a BEC is shown in Figure 2.14, from left to right the atoms are accumulating in a single state.

Photons are also of bosonic nature. However, that was not much understood when R.Hanbury Brown and R.Q.Twiss developed the theory of intensity interferometry, and they encountered some skepticism on the validity of their technique. Although, their technique was validated for radio waves, some believed that in the case of visible light, where the photon energy is high,

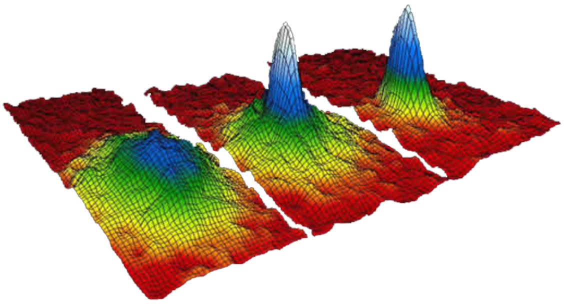

Figure 2.14: Bose-Einstein condensate forming from left to right. The x- and y-axis represent the velocity in two-dimensions, the z-axis shows the atom (rubidium atoms) distribution. The boson particles accumulate into a single state when cooled down. Source: Wikipedia.

photons could not be in the same quantum state at two different detectors and thus there could be no correlation observed. The pessimistic speculations were proven wrong experimentally. The justification actually arose from the exact fact that photons are bosons and thus will tend to appear in the same state in "packages". Hanbury Brown and Twiss called it photon-bunching and it relates to the coherence of light. On the contrary, fermions would show anti-bunching, as they cannot occupy the same quantum state, and thus would "repel" each other. Later on, Roy J. Glauber gave a rigorous description of quantum optical coherence and was awarded the Nobel prize in 2005 for his "contribution to the quantum theory of optical coherence". Surely this has highly benefited the field of particle physics. As a matter of fact, this bunching effect is widely used to study all sort of bosonic particles. Practically, the particles to study are scattered bosons (typically pions, kaons or nucleons), and the resulting correlation of the scattered particles contains information on the particle sizes, the basic concept is thus similar to stellar interferometry which measures angular diameters. Figure 2.15 and 2.16, illustrate the bunching or anti-bunching for different particle statistics. Figure 2.16 shows the second order correlation for these different statistics. It is worth noting that for the case of particle physics, this phenomenon - often called the HBT effect (for Hanbury Brown-Twiss) has led to a very wide literature, while for astronomical applications it has remained confined to the original stellar intensity interferometer in Narrabri, and usually occupies 1 page or less in textbooks treating interferometry.

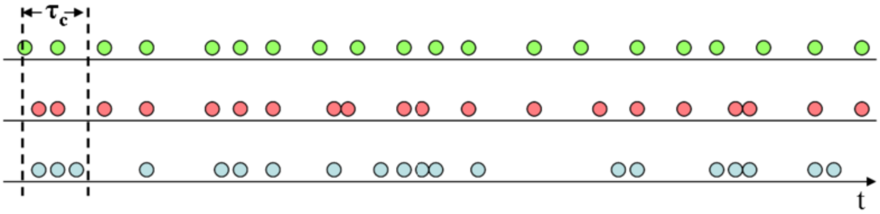

Figure 2.15: Bunching for different classes of particles. Left: From top to bottom: coherent laser radiation (no bunching), classically random (partial bunching), thermal bosons (bunching).

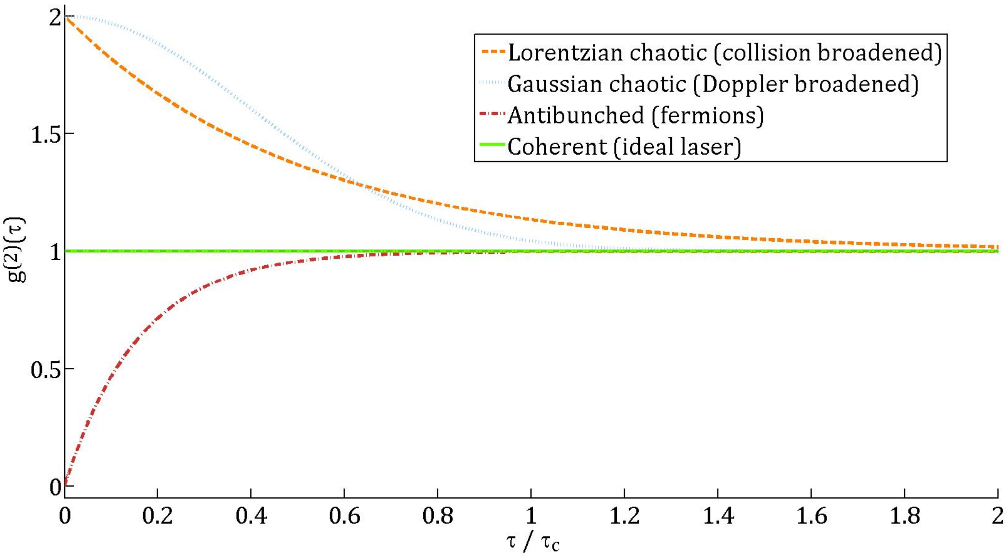

Figure 2.16: The second-order coherence for different particle statistics.

Finally, although it has high historical value, the quantum description is not necessary to understand stellar intensity interferometry (SII). However, it brings a new approach to the study of starlight, which was completely original with the Narrabri interferometer, but it was then never repeated. Here lies an important argument toward a modern SII. It would allow an even better understanding of quantum properties of starlight, and with much better instruments than the ones of Narrabri, thus it is audacious but not completely hopeless to imagine that a modern SII has a broader potential than stellar imaging and could act as a pathfinder for future quantum astronomical instruments. In fact, the classical way of studying starlight is touching its limits while quantum optics is revolutionizing other fields in sciences (medicine, particle physics, communication, security, ...).

Chapter 3

Laboratory set-up

This chapter describes the set-up of the experiment. First, a general overview of the layout is given, the detectors and the correlator are described and discussed as they represent an essential part of an intensity interferometer and the design of the laboratory star is explained.

3.1 Overall set-up

Lund Observatory possesses a large optics laboratory of 25 m length. This allows one to observe artificial stars at a practically "infinite" distance (for an adequately small star), thus simulating observations of real stars.

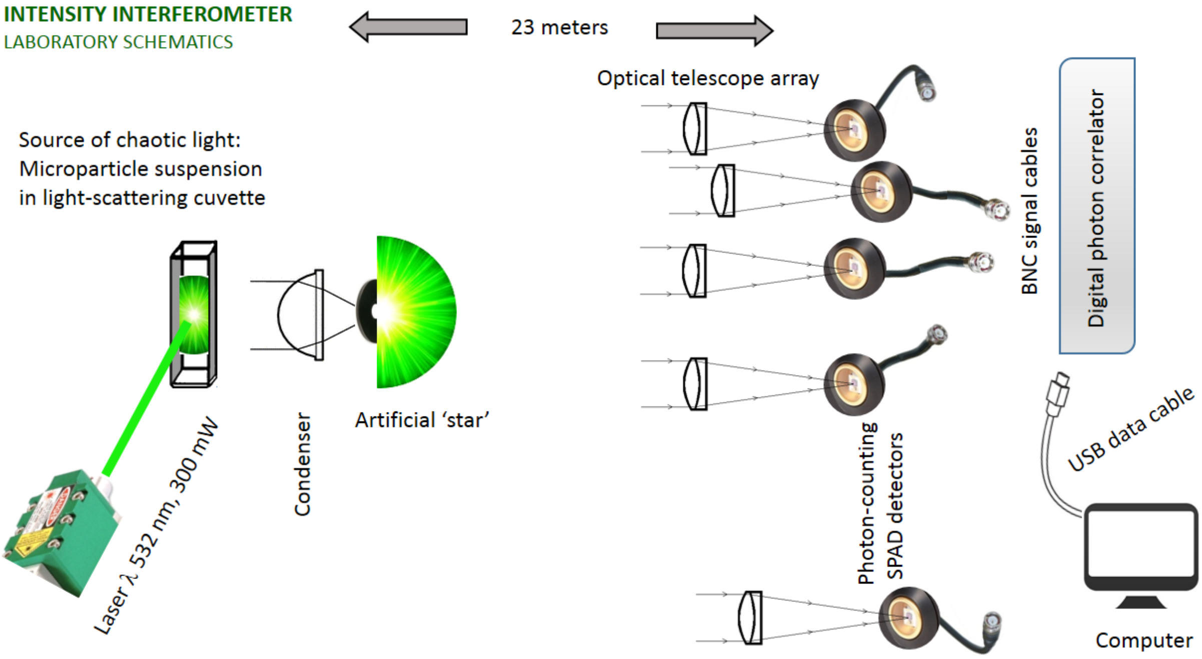
INTENSITY INTERFEROMETER
LABORATORY SCHEMATICS
23 meters
Optical telescope array
Source of chaotic light:
Microparticle suspension
in light-scattering cuvette
BNC signal cables
Digital photon correlator
Artificial 'star'
Condenser
Laser λ 532 nm, 300 mW
Photon-counting
SPAD detectors
USB data cable
Computer

Figure 3.1: Laboratory layout of a simulated stellar intensity interferometer. An artificial star is created by scattering coherent light onto microparticles in a cuvette, the resulting light is spatially filtered by a pinhole with a typical size on the order of 100 μm. An array of optical telescopes is set up at the other end of the lab. Each telescope focuses light onto a Single Photon Avalanche Diode detector. Signals from the detectors are correlated by the digital correlator, and the data are transferred to a computer through a USB cable.

The laboratory layout is shown in figure 3.1. A small-scale telescope array is set-up at one end of the laboratory room (to the right on the figure) and observes the artificial star at the other end (left in the figure). The distance between the array and the star was measured to be 23 m. The size of the artificial star is of the order of 100 μm which, seen over the distance of the lab, subtends an angular diameter of ≈ 0.9 as.

The array of telescopes is composed of five achromatic objective lenses of some 30 mm diameter and 50 mm focal length, which collect and focus the starlight onto the detectors. They are mounted on a three-axis adjustable X, Y and Z direction mount, allowing precise adjustments of the focus. The telescopes are labelled as telescope 0 to telescope 4, as seen on Figure 3.2; Table 3.1 gives the baselines for the different combinations of telescope pairs. Telescope 0 and telescope 1 provide the shortest baseline, and to achieve that, a 45^o mirror is placed at ≈ 3 cm from detector 1. Without the use of such a mirror, the physical size of the components constrains the shortest baseline to 5 cm.

The detectors are discussed in the next section. They are single pixel detectors with a small pixel size of only 100 μm, which makes it complicated to focus the star light. The detectors are then connected to a correlator via BMC cables. The correlator used is described in a following section of this chapter. The correlator cross- or auto-correlates the signal from the different detectors, and the data are sent electronically to a computer. As the overall experiment requires complete darkness, and also the bright computer screen is a disturbance, that is set up in an small adjacent room together with the correlator. The detectors are connected to the correlator with long BMC cables of 10 m. It was checked experimentally that this length of cable does not affect the correlation.

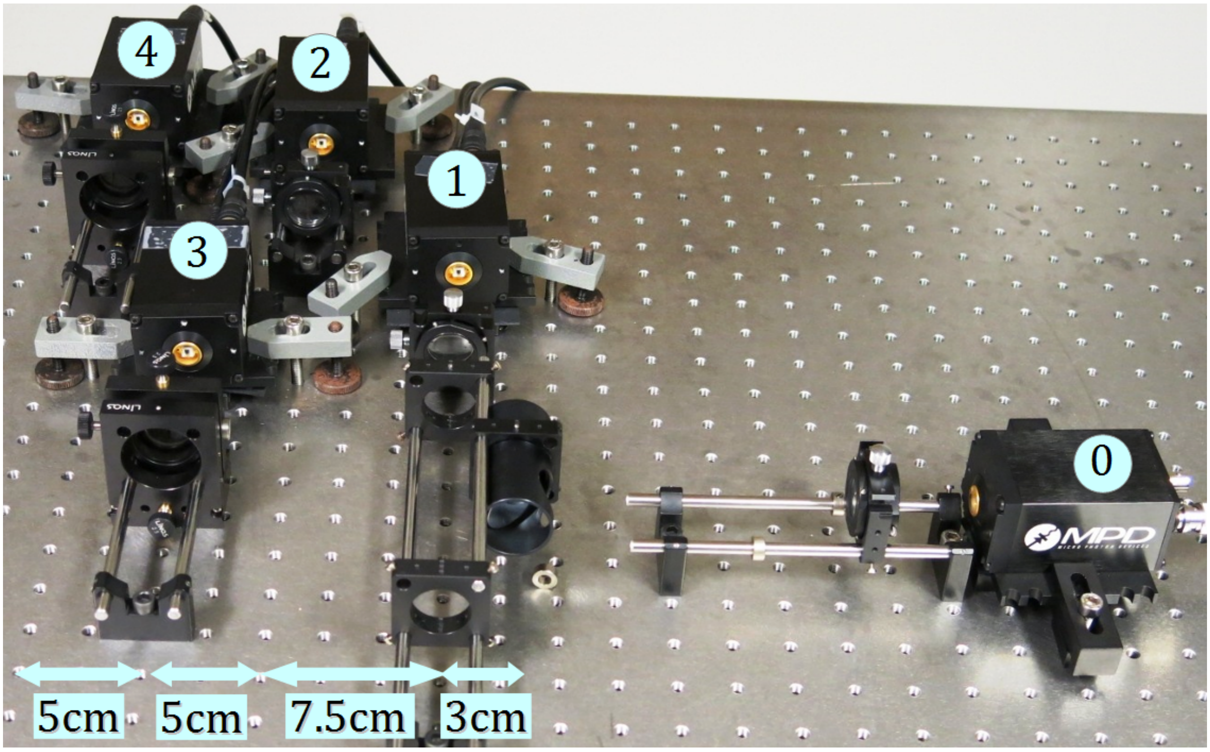

Figure 3.2: A picture of the telescope array showing the five 50 mm focal-length lenses in front of the SPAD detectors. The arrows show the baselines between adjacent telescopes.

Telescope Combination	**Baseline**
0 and 1	3 cm
0 and 2	10 cm
0 and 3	15.5 cm
0 and 4	20.5 cm
1 and 2	7.5 cm
1 and 3	12.5 cm
1 and 4	17.5 cm
2 and 3	5 cm
2 and 4	10 cm
3 and 4	5 cm

Table 3.1: Different baselines of the array shown in Figure 3.2

In order to produce a 2-dimensional array such as CTA, the pinhole aperture spatially defining the artificial star is put in a mount that can be rotated by steps of, e.g., 10^o, this being equivalent to rotating the whole array of telescopes. The principle is illustrated in Figure 3.3; the array lies on a line making an angle α with an axis of the u-v plane. It can only measure $|V^2|$ for the radial distances equal to the baselines in Table 3.1 in polar coordinates. As the correlator does not store the raw data coming from the detectors, $|V^2|$ is measured between telescopes at different radial positions but only one angle at a time. Thus, it is not possible to obtain the correlation between telescopes at different position angles. It is important to note that this arrangement allows one to cover different parts of the u-v plane by rotation, but does not allow to have baselines of other lengths than those in Table 3.1. This configuration is hence useful for measuring $|V^2|$ of rotationally asymmetric stars, such as an elliptical star or a binary system.

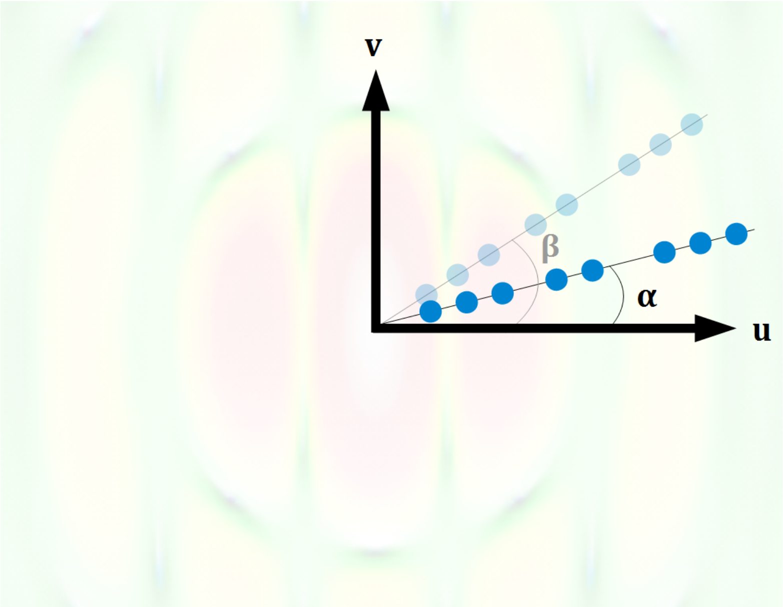

Figure 3.3: Illustration of the effect of rotating the linear array (in practice, this is done by rotating the pinhole star) to cover a larger part of the u,v-plane. The u,v-plane axes are represented with the different baselines; shown as blue dots; superimposed onto a theoretical second- order coherence map $|V^2(u, v)|$ for an example of a binary star.

3.2 Detectors

One main limitation of stellar intensity interferometry is the signal to noise ratio, from equation 2.38, the SNR depends on Δf the electronic signal and α the quantum efficiency of the detectors. These two parameters are intrinsic to the detectors and consequently the detectors are a crucial part of any intensity interferometer. Today, much more powerful detectors than the ones used in Narrabri are available on the market, which represents one of the main justifications for the renewal of an intensity interferometer. Many detectors have previously been tried out at Lund Observatory in order to find a good candidate for laboratory simulations. Single photon diode detectors were favored since they possess high quantum efficiency and are very fast in detecting single photons. Single Photon Avalanche Diodes (SPAD) manufactured in Italy[1] were chosen and ten of them were ordered, five of them are used in this laboratory setup, as explained in the previous section and pictured in Figure 3.2.

APD (avalanche photo diodes) are semiconductor detectors (solid state instruments). An incident photon reaches the light-sensitive area of the detector and produces a charge carrier (an electron-hole pair) in the absorbing region. The pair created is driven toward a multiplication region. This process is carried out by the use of an electric field applied inside the semiconductor. There, the charge is multiplied, resulting in an avalanche of charges which can be detected and transmitted by regular electronics.

A SPAD is an APD operating in the so-called Geiger mode. At this operation mode, the voltage is set above the breakdown voltage. Additionally, the current is limited to the “latching current” (minimum current required to maintain the device “ON”). So the fluctuation of the current are centered around zero (the device is “OFF” with regard to the current). The device is turned “ON” by a photon event (avalanche). This way the avalanche photodiode can record single photon events. It is understandable that the dark noise current is a crucial parameter to control, which can be achieved by efficient cooling of the detector. This mode of operation leads to a high gain.

Important issues of such devices are listed below:

> **The dead-time**: After an event (avalanche induced by an incoming photon) the dead-time is the time during which the detector cannot record any new event.
>
> **Afterpulsing**: It is possible that a carrier created by the photon event gets “stuck” at a certain region in the avalanche region. When it is liberated, it is liable to create a new avalanche.
>
> **Dark signal**: It is the signal produced by randomly produced photoelectric events within the device. The dark current can be measured by operating the device in “the dark” (no photons reaching the detector). This effect can be attenuated by cooling the device.

The ten detectors all came with technical test reports. They are of grade A which indicates a dark count below 500 cps (counts per second). Their sensitive areas are 100 μm in diameter and they are cooled through Peltier cooling.

---

[1] `http://www.micro-photon-devices.com/`

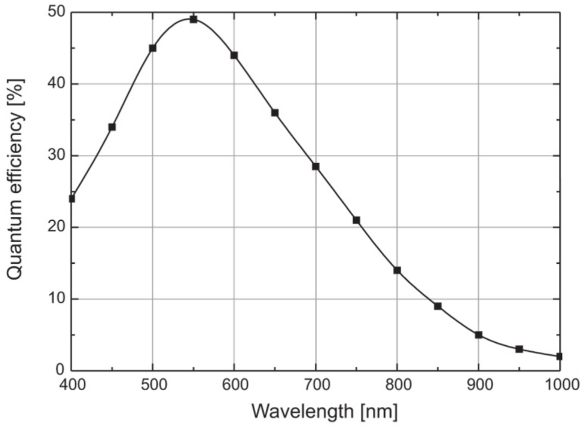

Figure 3.4: Quantum efficiency of the detector as a function of wavelength.(Provided by the manufacturer, MPD, Micro-Photon Devices)

3.3 Correlator

The correlation functions are calculated with a digital processor manufactured by a small US/China company [2]. The principle of the device is illustrated in Figure 3.5; the detectors measure the intensity of the light $I(t)$ (which is proportional to the number of detected photons, i.e., *number of counts*), the output electric signals are fed to the data processor via coaxial cables and it calculates the temporal correlation between the two signals, i.e., $I_1(t) * I_2(t+\tau)$. The correlator also provides a normalisation of the correlation, which is that the resulting function goes to 1 for long delay times τ. The data are processed in real time and are sent to a computer with the associated software through a USB 2.0 port. The software allows the visualization and storing of the correlation function in real time, as well as the intensity trace and the count rate, thus optimizing the amount of stored data.
The correlator used has a system clock speed of 200 MHz which corresponds to a time resolution of 5 ns.

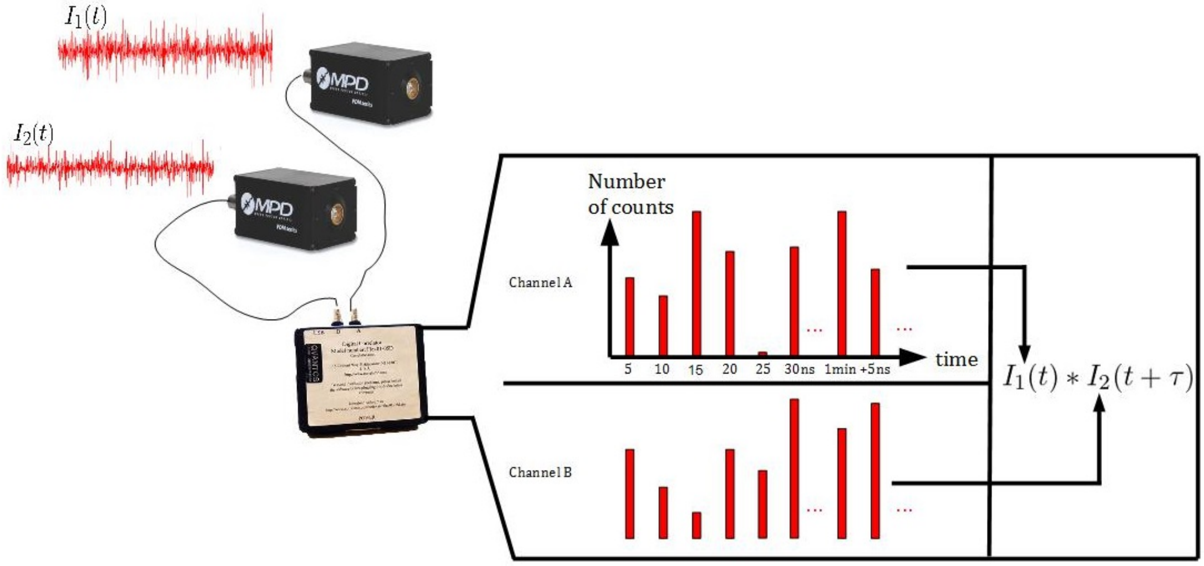

Figure 3.5: The correlator

---

[2] `http://www.correlator.com/`

3.4 Artificial stars

The design of an appropriate illumination of the artificial star is a key point of a laboratory simulation of stellar intensity interferometry. The illumination indeed needs to both have a suitable high brightness temperature, in order to achieve good SNR (see Section 2.4.2), and be of thermal light nature (in order to have the thermal photon bunching). Thermal light means that the light-wave has “random” properties, e.g., that the statistical distribution over time of the electric-field amplitudes in the light follow a Gaussian distribution. While various thermal light sources had been tested in the lab previously (mainly arc lamps), they turned out not to be bright enough. The SNR was then too low, as predicted from relationship with source temperature (Figure 2.13). An alternative way of producing thermal light of a high brightness temperature was then found by using dynamical light scattering (DLS) explained below.

If light incident onto small particles has a wavelength on the same order as the particle sizes, it can interact by scattering. In the case of elastic scattering (i.e., almost no energy shift between the incident and scattered field), the incident light impinges on the particles and is redirected in a new random direction. The electric field arising from the scattering is then the superposition of the field scattered by each particle, and in the case of a coherent light source (a laser), the field will be a combination of constructive and destructive interferences. If the particles are big enough, the field can be directly observed, appearing as a speckle pattern.

Now, if the particles are in motion, the speckle pattern is fluctuating at the same rate as the particles are moving. For the case of particles suspended in a liquid, their motion is determined by Brownian motion of the molecules of the suspending liquid. These motions are thermally excited and mechanical bumps occur onto the scattering particles, inducing a random path of these. These random motions produce a Gaussian statistics of the scattered field. In fact, let us focus on only one speckle of the whole pattern, and let us measure the intensity at this position. In time, the speckle is moving due to the Brownian motion of the scatterers, thus the intensity is oscillating. The intensity oscillates equally fast as the scatterers are moving, and because it is moving randomly, the resulting oscillations are also random. In consequence, one benefits from a bright quasi-monochromatic light source (laser), broadened in wavelength by scattering and obtaining Gaussian statistics. The source is then temporally incoherent and its temporal coherence depends on the size of the scatterers as follows:

$$\tau \approx \frac{r^2}{D_0}, \tag{3.1}$$

where r is the particle radius and D_0 is constant known as the diffusion coefficient and is an intrinsic property of the particle. In fact, a particle of small r is lighter and hence moves faster than a heavier scatterer of larger r.

This last equation also asserts that it is possible to control the temporal coherence τ of the source by controlling the size r of the scatterer. As a matter of fact, such Dynamical Light Scattering (DLS) is used in chemistry to measure molecule sizes through the temporal coherence measured by temporally correlating the scattered field. A cartoon in Figure 3.6 illustrates the principle of DLS.

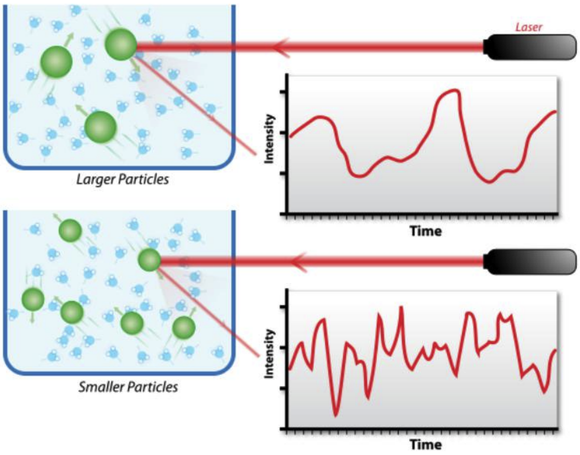

Figure 3.6: Principle of Dynamical Light Scattering. A coherent source shines onto scattering particles suspended in a medium. The smaller molecules of the thermally excited medium bump into the scattering particles, thus displacing them in a random manner, so-called Brownian motion. The intensity of resulting scattered light is fluctuating randomly in time as the scatterers are randomly moving. The smaller the scatterer (for a same diffusion coefficient) the faster the intensity fluctuations.

In practice, the artificial star is set up as follows:

A solid-state laser (*naon250* from *QIOPTIC*) produces very bright illumination; the laser can be seen on the left side of Figure 3.7. It operates at 532.05 nm (close to the peak of quantum efficiency of the detectors) and the output power can be tuned up to 305 mW, it also has an actively stabilized temperature. It is classified as a $3b$ class laser, meaning that it requires the use of goggles appropriate to its wavelength. The laser was purchased together with a portable remote control. This way it can be controlled easily without the use of an additional computer. The laser beam is focused into a cuvette holding the scattering liquid. The focusing lens is placed right before the cuvette, it has a short focal length of half a centimeter allowing a tight focusing. The light is focused at a corner of the cuvette, close to its walls. In this manner, the scattered light travels a shorter distance inside the liquid, avoiding possible multiple scattering which is not desirable (in fact this would modify the statistics of the resulting scattered light).

The scatterers are manufactured by Polysciences Inc. They consist of plastic spheres of micrometer sizes suspended in water. A kit of six different sizes of these microspheres were ordered for the lab. However by looking at the literature on dynamical light scattering it was realized that fat globules in commercial milk happen to have similar properties as these microspheres. For the purpose of the laboratory work, milk was easier to handle and several orders of magnitude cheaper than the microspheres, and for this reason, commercial milk diluted in water was used for most of the experiments. Previous simple experiments had shown that the intensity of the scattered light increased by increasing the milk concentration (more scatterers, thus more scattered light) until the solution would become opaque and then the intensity would decrease. The peak was found roughly at a ratio of 1 part of milk with 2 parts of water, which was the ratio used in the later experiments. Knowing that the cuvette holds a bit above 3 ml, it means that 1 ml of milk was diluted by 2 ml of water.

A pinhole aperture placed after the cuvette defines the 2-D shape of the star. In order to maximize the brightness a condenser lens was placed between the cuvette and the pinhole. The laser and the pinhole form an angle, which is roughly 90^o. This was made, so that the light impinging onto the pinhole comes from the scattered light and no direct laser light reaches it. The cuvette within its holder can be rotated to have the light-scattering volume in an optimal direction towards the pinhole.

In this manner, the light illumination has become randomized (chaotic) by the scattering process but still retains an extremely narrow spectral passband set by the Doppler broadening by the microspheres undergoing thermal Brownian motion in the cuvette. Given the high luminosity of the scattered laser light, this implies a very high brightness temperature over that very narrow spectral passband. However, given that the SNR ratio is independent of spectral passband (Equation 2.38), this quasi-monochromatic light source enables experiments that in many ways are equivalent to those with white light from blackbody sources of high temperature, such as hot stars.

Finally, the pinhole "star" needed to be shielded from all other parasitic light coming from the laser beams and multiple reflections. A simple and cheap carton shield was fabricated around the set-up. The inside of the box is covered by matte black material, so that there are as few reflections as possible. A small aperture lets the light forming the pinhole to escape. This method turned out to be extremely efficient in removing all the direct and diffuse light coming from the laser. A removable lid finishes the shield-box. In this way, it was also possible to easily access the pinhole and cuvette. The box also possesses a small opening for the power cable to the laser. The laser's remote control is then placed outside, and thus the laser could be operated from outside the box.

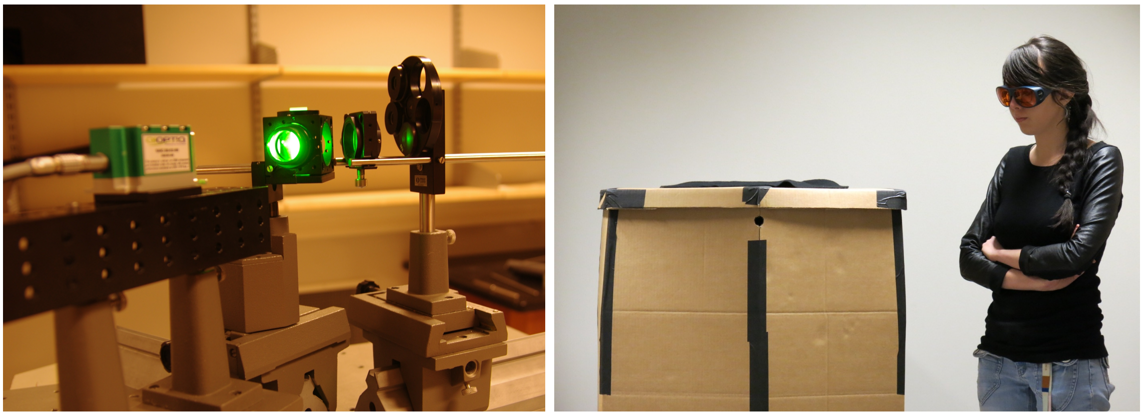

Figure 3.7: The set-up of the laboratory star [left] and the final covering box with myself standing next to it [right].

3.5 Focussing the telescopes

Focussing the light from the telescopes represented a challenge due to the small size of the detector sensitive area (100 μm). In the laboratory, the focus was adjusted manually in two steps; first visually and then with electronic assistance using the output signals of the detectors. However, for focusing visually with the bare eye, the aperture "star" had to be much brighter than what was used later during the actual experiment. To achieve that, the initial set-up was simplified to have the laser illuminating the aperture directly at full power. Indeed, for focussing, only the brightness (and not the thermal photon statistics) was required. After this first visual focus, the detectors, the correlator and the computer were turned on. Although it is obvious that the correlator did not record any correlation, due to the high coherence of the laser, the interactive part of the software also allows to read out the intensity level recorded by the detectors. It was thus possible to track the maximum intensity output. Furthermore, the micrometer wheels of the lens holders provided a high focusing accuracy. For the laboratory configuration, the procedure used was that one person read aloud the detectors' output while another was adjusting the foci, but no additional measuring equipment were needed.

3.6 Experimental procedure

This section outlines, step by step, the experimental procedure which was used to measure the cross-correlation between the photon-count signals from pairs of detectors or/and the auto-correlation from a single detector. While this section is not necessary for the understanding of the rest of the thesis, it aims to show how the experiments were done, and highlights the important steps of safety concerns.

The first steps of the procedure consisted in preparing the "star", which had to be done each time the measurements were performed. First the solution with scattering particles was prepared in the cuvette according to what was described earlier (diluting 1 ml of fresh milk with 2 ml of water). The cuvette was then placed in its holder and the angle of the cuvette relative to the laser beam was adjusted. For simplicity, a marker had been put on the cuvette holder. An aperture also had to be selected and positioned in its holder, and this was rotated to the desired angle. The next step was then to turn on the laser and first adjust it to a low power output using safety goggles. For a sufficiently low power (a couple of mW say) it was safe to take off the safety goggles and visually inspect the scattering. It had to be verified that the laser light was scattered in the solution and properly focussed onto the pinhole. Then, the lid of the shielding box could be closed, and then (again using the goggles) the power could be increased to a suitably high value. For the experiment, the maximum power available, ie., 300 mW was normally used .

The second step consisted of turning on the detectors after making sure that all lights in the laboratory, except the star, were off. As a matter of fact, this precaution was very important to protect the detectors from being damaged by too high a light flux. Moreover, during the measurements, there had to be no other light disturbing the signal from the star. When these precautions had been taken, the correlator software could be launched on the computer in the adjacent room, and the BMC cables of the desired detectors could be connected to the input channels of the correlator. After that, the first thing was to check that there actually was a signal coming from the detectors. If there was no signal, one had to verify that the detectors were both turned "ON" and connected to the correlator and that an appropriate mode had been selected with the software. If there was a signal but only very small, it had to be checked that there was a normal amount of light emerging from the star. Otherwise, the problem was likely to be from poor focus at the detectors. However, once the detectors were turned on, they needed a couple of minutes before stabilizing and becoming operational.

A screenshot of the software interface is presented in Figure 3.8. It shows that four correlation modes are offered. The so-called *QUAD*-mode was often used for the signals entering input channels A and B, as it permits to simultaneously obtain all auto- and cross-correlations (AxA, BxB, AxB and BxA). The integration time can be selected at the bottom. During the experiments, high count rates allowed to choose an integration time of typically 2 min. To start the correlation one clicks "*START*". The trace appears on the top right of the windows, the count rates for the two channels in the bottom left. The two large main windows show the four correlations (in the case of the QUAD mode). When the computations are finished, one clicked the save button and saved the file in a specific $*.SIN$ format. Typical filenames used were of the type *100-30-det1and2*, where the first number stands for the aperture size in micrometers, the second number for the position angle of the aperture in degrees and the last term for the pair of telescopes and detectors used. To simplify the analysis, the telescope with the lower number was always put in channel A.

To measure another baseline, the BMC cables (labelled as 0, 1, 2, 3 and 4, to identify the respective telescope) were switched at the correlator. The particular correlator used was the most reliable one among several available but, being a two-channel unit, it permitted only one baseline at a time to be measured. This affected the time efficiency of each experiment. Indeed, all the baselines could not be measured simultaneously but only one at a time. Thus if an integration time of 2 min was used, measuring ten different baselines would take 20 min plus some additional time for switching cables.

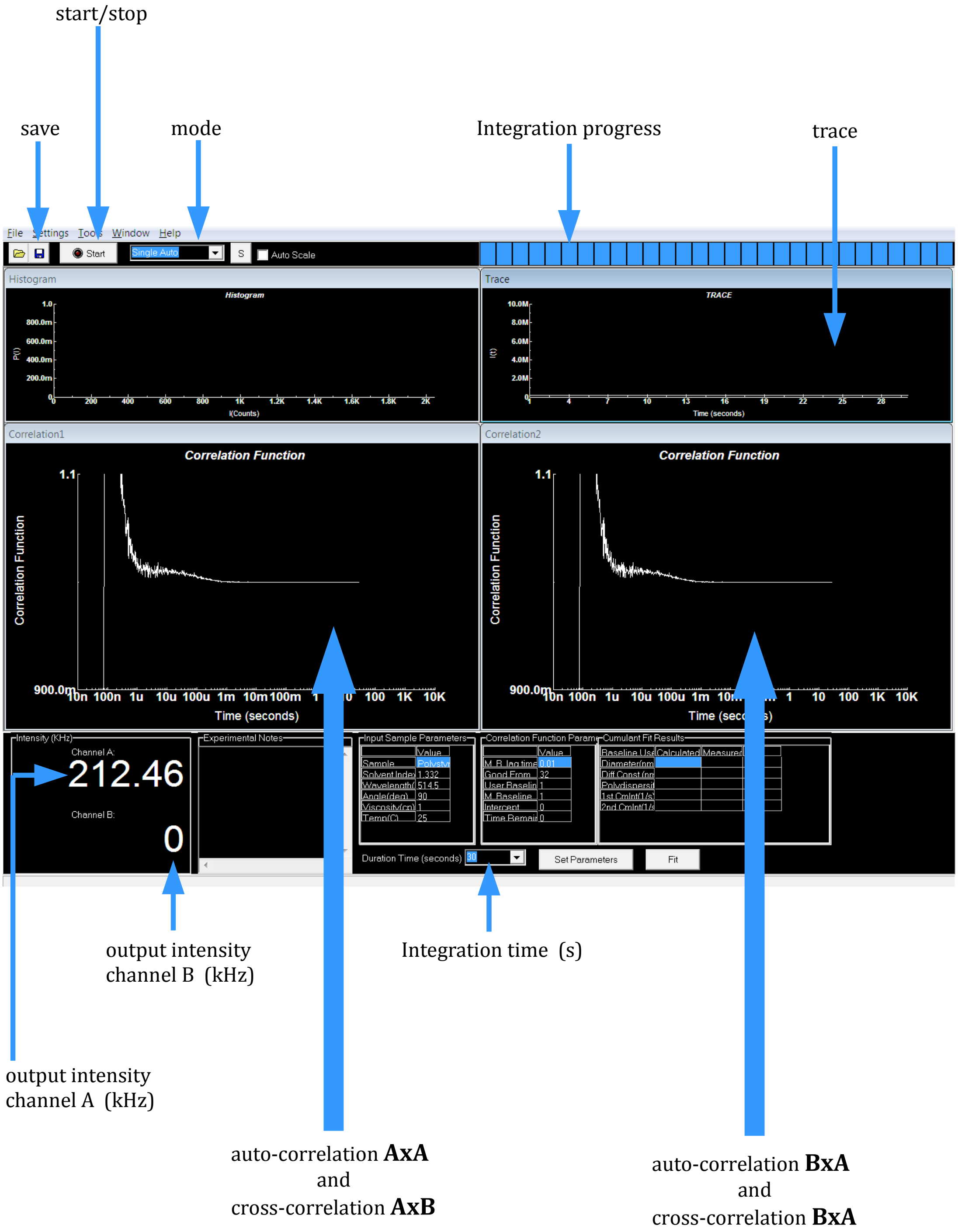
start/stop
save
mode
Integration progress
trace
File Settings Tools Window Help
Start
Single Auto
S
☐ Auto Scale
Histogram
P(I)
I(Counts)
Trace
TRACE
I(t)
Time (seconds)
Correlation1
Correlation2
Correlation Function
Time (seconds)
Intensity (KHz)
Experimental Notes
output intensity channel B (kHz)
Integration time (s)
output intensity channel A (kHz)
auto-correlation **AxA** and cross-correlation **AxB**
auto-correlation **BxA** and cross-correlation **BxA**

Channel A: 212.46

Channel B: 0

Input Sample Parameters

	Value
Sample	Polystyr
Solvent Index	1.332
Wavelength(	514.5
Angle(deg)	90
Viscosity(cp)	1
Temp(C)	25

Correlation Function Parame

	Value
M. B. lag time	0.01
Good From	32
User Baselin	1
M. Baseline	1
Intercept	0
Time Remair	0

Cumulant Fit Results

Baseline Use	Calculated	Measured	
Diameter(nm			
Diff Const (nm			
Polydispersit			
1st CmInt(1/s)			
2nd CmInt(1/s			

Duration Time (seconds): 30

Set Parameters

Fit

Figure 3.8: Screenshot of the correlator software interface.

Chapter 4

Artificial star diffraction images

While focussing the telescopes as described in Section 3.5, it was realized that it was possible to examine the detailed diffraction patterns of the pinhole apertures on the wall just behind the array of telescopes. Due to the large extent of the laboratory and the high coherence of the laser, the visible pattern extended to some 1 m in size and presented very bright and clear features. Since this cannot be observed in an ordinary and smaller optics laboratory, it was decided to take the opportunity to make a survey and photograph the diffraction patterns. Do to so, a large screen was placed in front of the optical table supporting the telescopes and detectors, and a camera was placed on a tripod in front of it, but slightly to the side in order not to block the light on its way to the screen. The distance from the pinhole to the screen was measured to be 20.38 m. All available pinholes were hence examined visually and images recorded. In addition to the pedagogical aspect of the exercise, the images obtained carried relevant information about the exact dimensions of the pinholes. Indeed, as discussed in Section 2.1, the diffraction pattern is formed by the squared magnitudes of the Fourier components of the brightness distribution of the aperture, which are directly proportional to the intensity correlations to be measured in this project. It was thus possible to have an independent precision measurement of the size of the pinholes and/or of their eventual shape irregularities.

Reference images of a ruler on the screen in vertical and perpendicular directions were also taken with the room light turned on. Knowing the source-to-screen distance, such a reference image provided a precise scale for the interpretation of the diffraction patterns (and can also partially compensate for possible distortions in the camera). This procedure allowed to select the pinholes which were the most interesting for the experiment. Five were selected on different criteria: a single round aperture of 0.10 mm diameter, one of 0.15 mm, one of 0.20 mm, a double pinhole with two 0.10 mm apertures (their exact separation was then unknown), and an irregular opening of 0.10 mm size. These sizes were the ones specified at the manufacture and are used as labels. The three first pinholes were chosen for their quality as they showed good symmetry and shape. The double pinhole was chosen to illustrate a more complex stellar structure such as a binary system. The last pinhole was chosen for its elongated shape, providing a good elliptical star. The pictures captured are shown in Figure 4.1. Each of these images covered 36x36 cm on the projection screen.

Following this analysis, the different pinholes were labelled and documented. The chosen pinholes have the following labels as used in the rest of this thesis: 0.100#1, 0.150#1, 0.200#1, 0.100 + 0.100#1, and 0.100#3. The first part of the label is the nominal fabrication size in mm, the second part is a reference number to differentiate between different pinholes of the same nominal size. To avoid confusion among similar tiny apertures, this last number was then engraved directly on the pinhole holder as small dots. For example, the number one would have one dot, number two two dots and so on. Furthermore, for the pinholes showing elliptical shapes the position of their major axis was marked onto the pinhole holder.

The recorded images were used to calculate the sizes of the pinholes using Equations 2.6 and 2.7. Table 4.1 summarizes the results, giving both the results in mm for the pinholes and the corresponding angular diameter in arcseconds. The angular diameter was of course calculated for the distance between the pinholes and the telescope array, i.e., 23 m, rather than for the somewhat shorter pinhole-screen distance, as that is irrelevant for the rest of the experiment.

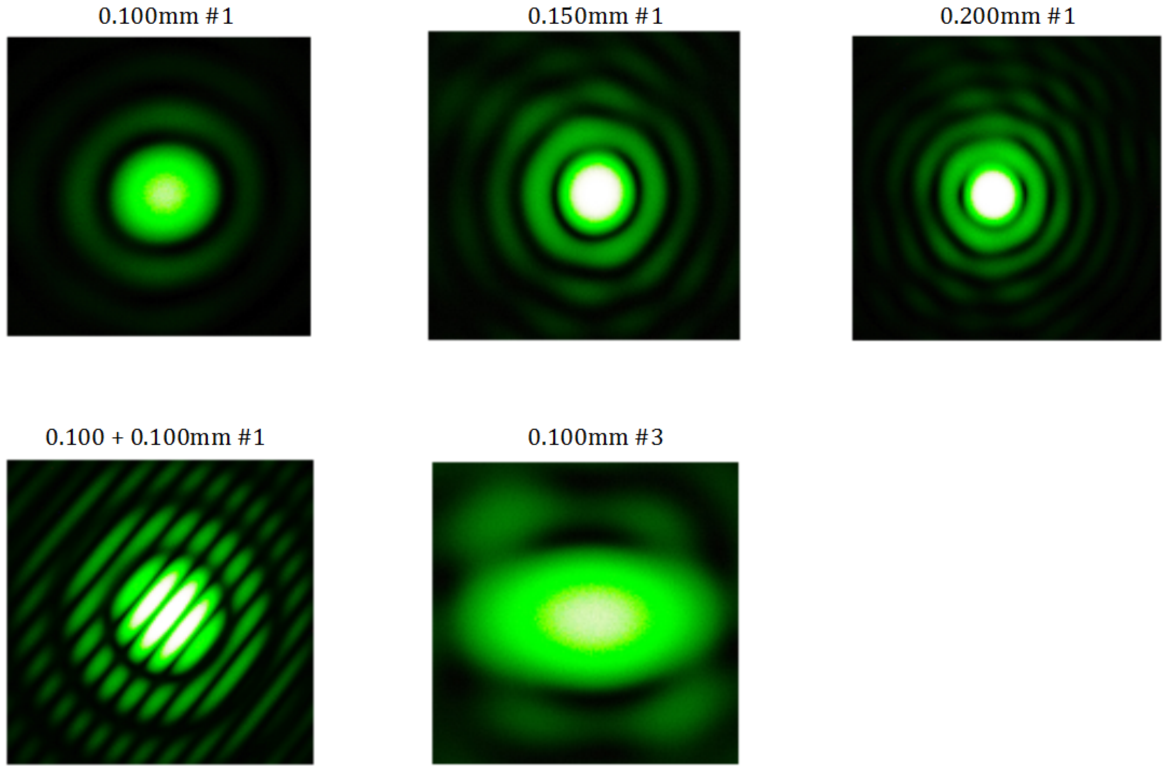

0.100mm #1

0.150mm #1

0.200mm #1

0.100 + 0.100mm #1

0.100mm #3

Figure 4.1: Fraunhofer diffraction patterns produced by five different pinhole apertures ("artificial stars"). The sizes are nominal ones from their manufacture. Images cover 36x36 cm on the projection screen.

Pinhole aperture	**Diameter measured experimentally**	**Corresponding angular diameter (at 23m distance)**
0.10 mm #1	0.090 mm	0.81”
0.15 mm #1	0.131 mm	1.18”
0.20 mm #1	0.180 mm	1.62”
0.10 mm #3		
long axis	0.064 mm	0.57”
short axis	0.036 mm	0.32”
0.10 + 0.10 mm #1	0.097 mm	0.87”
separation	0.306 mm	2.74”

Table 4.1: The apertures selected for the artificial stars were measured experimentally by analyzing the diffraction patterns from Figure 4.1. Corresponding angular diameters were calculated for a distance of 23 m, corresponding to the distance between the artificial star and the telescope array.

Chapter 5

Intensity interferometry of stars

This chapter presents the results together with an explanation of the data analysis. First, I outline how the data were analyzed, i.e., how the squared visibilities were extracted out of the correlation data. Following that, the results for different artificial stars are presented.

5.1 Reading and plotting the data

The correlator software produces data in a specific $*.SIN$ format, a format that can easily be opened and read with *Matlab*, which was used for the data analysis of this thesis. The data analysis is detailed in this section and for illustrative purposes, the analysis is described for an example of the circular aperture #1 of 0.10 mm.

For this example the correlator was set in the $QUAD-mode$ (as for most experiments), meaning that both the auto-correlations of the two channels A and B (ie., $A*A$ and $B*B$) and the cross-correlations between them (ie., $A*B$ and $B*A$) were measured simultaneously. The signal from telescope 0 was plugged into channel A an telescope 1 in channel B, thus the correlations correspond to $I_0 * I_0$, $I_1 * I_1$, $I_0 * I_1$ and $I_1 * I_0$ with I_0 and I_1 being the fluctuating intensity at the detectors 0 and 1 respectively. The two cross-correlations are thus for the baseline of 3 cm according to Table 3.1. Figure 5.1 shows what the actual correlation curves look like.

The correlator is measuring the temporal correlation, which is given as a function of a time delay τ on the $x-axis$ (here plotted on logarithmic scale); thus it is the temporal coherence of the photon stream that is measured first. Because the exposure time was set to 2 min, just above 10^2 s, it can be seen on the figure that the correlations cease around a time delay of 10^2 s. That the correlations start at either $\approx 10^{-8}$ s or 10^{-7} s comes from the time resolution of either the detectors or of the correlator. The autocorrelations are limited by the detector deadtime (80 ns), while the cross-correlations are limited by the correlator speed (5 ns). No faster auto-correlations can be recorded because each detector only give out one photon pulse per deadtime interval, however faster cross-correlations can be measured since the detector deadtimes are not simultaneous in different detectors.

High peaks for short delay times are observed for both auto-correlations, and are the result of detector afterpulsing. Although this occurs only for a small fraction of all photon detection events, its statistical signature stands out strongly. A few charge carriers have a probability to get stuck in the semiconductor detector and are released within few hundreds of nanoseconds inducing a new avalanche that is recorded as a photon event. The high correlation observed for such release times have nothing to do with the real physical correlation of photon arrival times (photons coming from the star). The cross-correlations are largely immune to this effect since the afterpulsing is not correlated between different detectors.

Figure 5.2 shows a zoom-up of Figure 5.1 for the part of the correlation curves that are of interest. This part coincides with the decay of the second-order temporal coherence $g^{(2)}(\tau)$ for chaotic light of Figure 2.5 and 2.6. The characteristic time of the decay is a measure of the temporal coherence τ_c of the incoming photons. For the Doppler broadened near-monochromatic light from the artificial star, it is observed that it lies in the μs range, but for a real star observed in broadband white-light, it would lie in the femtoseconds range.
In an ideal theoretical case, the correlation functions would reach the value 2; however multiple mechanisms contribute to diluting this value. Among the likely sources of loss is the effect of the finite size of the telescopes, the coherence is hence averaged over the telescope area which decreases it. Other sources may originate from imperfections in the detectors, such as their noise characteristics and their afterpulsing. If the laser light has undergone multiple scattering, the photon statistics of the starlight itself will not correspond to the chaotically "perfect" photon bunching. Finally, other external signals or stray light, to which the detectors may be sensitive, might decrease the correlation.

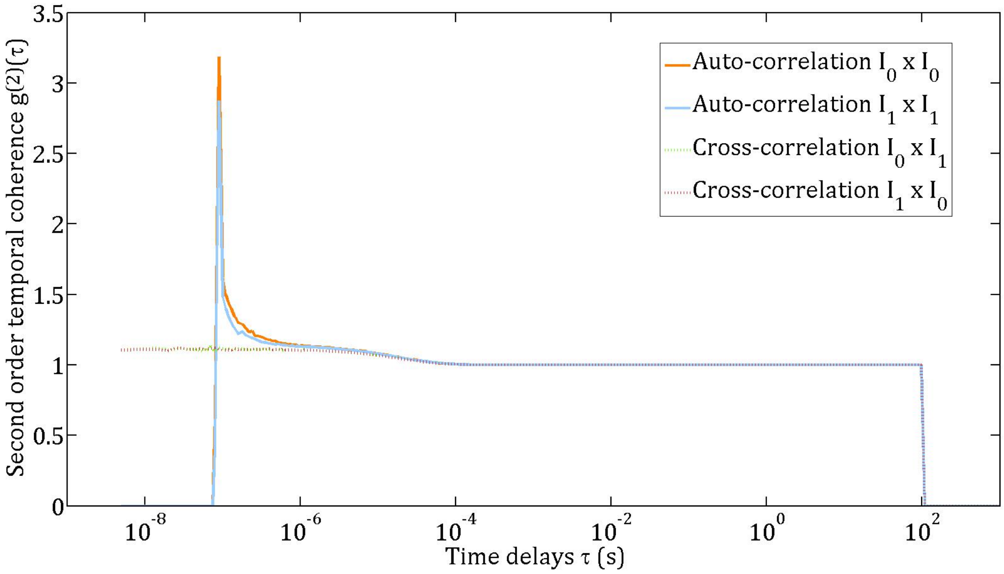

Figure 5.1: Auto- and cross-correlations measured by the correlator in the QUAD mode for telescopes 0 and 1, thus providing the telescope baseline 0 (autocorrelations) and the baseline 3 cm (cross-correlations). The plot shows time limits set both by the equipment (detectors and correlator) and by the experiment (exposure time). The afterpulsing is also apparent as the dominant peak at $\approx 10^{-7}$ s.

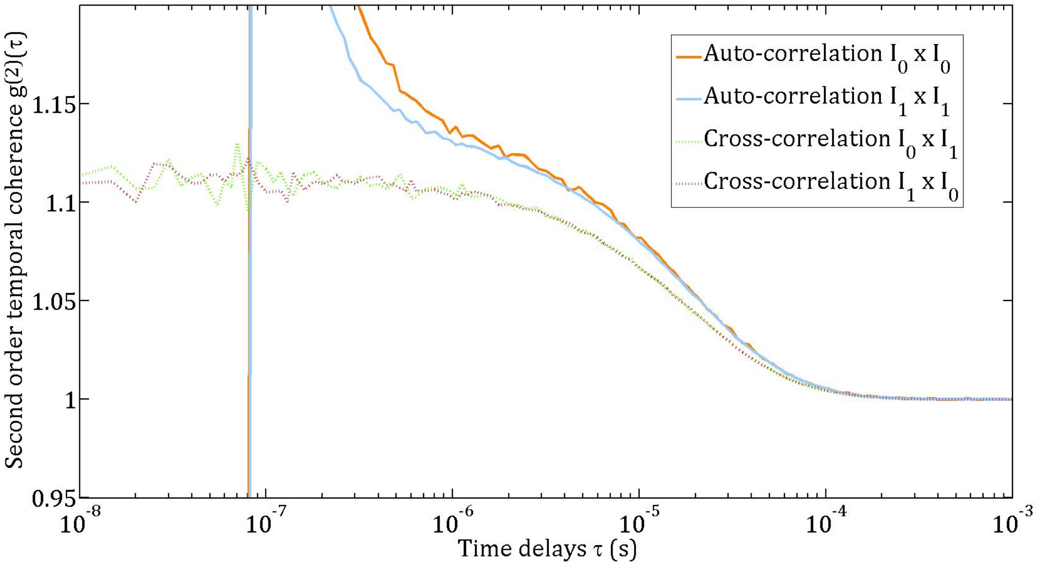

Figure 5.2: Zoom into Figure 5.1, showing the region of main interest. The decay of correlation with increased time delay is a measure of the second-order temporal coherence (Figure 2.6).

However, the aim was to obtain the *spatial* coherence. This was achieved by measuring $g^{(2)}(\tau)$ for many different telescopic baselines. The set-up comprised five telescopes, allowing ten baselines (+ one for the auto-correlation, i.e., zero-baseline). For each baseline the cross-correlations $A * B$ and $B * A$ were averaged together giving $g^{(2)}(\tau, b)$ with b the baseline ($b = 3\ cm$ for Figure 5.2). Figure 5.3 shows $g^{(2)}(\tau, b)$ plotted for each b, here the equal baselines (the two 5 cm and 10 cm) were averaged together, additionally all autocorrelations of each measurement were averaged to give the zero-baseline. It is immediately seen that $g^{(2)}(\tau, b)$ decreases as the baseline b increases.

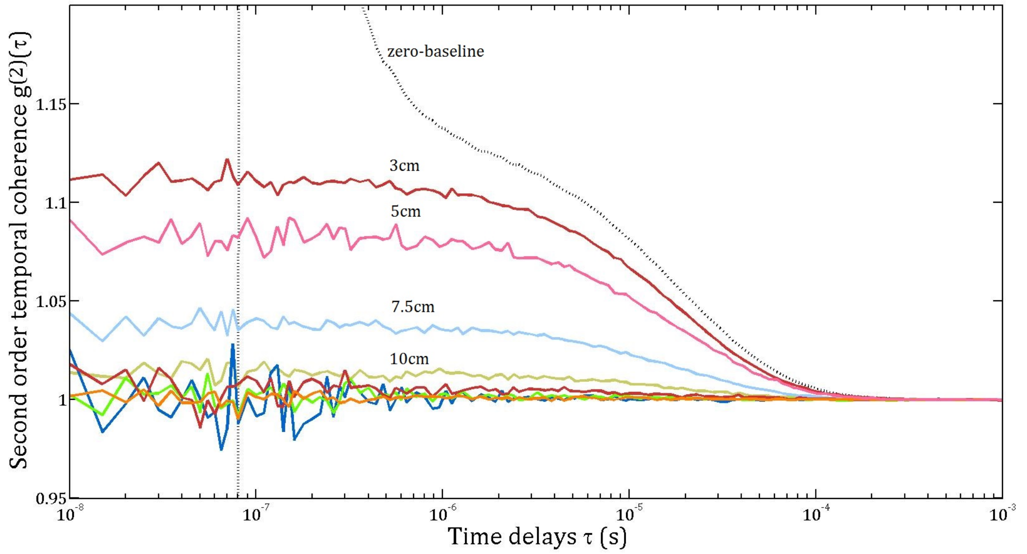

Figure 5.3: $g^{(2)}(\tau)$ plotted for different telescopic baselines b. The autocorrelation of all measurements were averaged to find the zero-baseline.

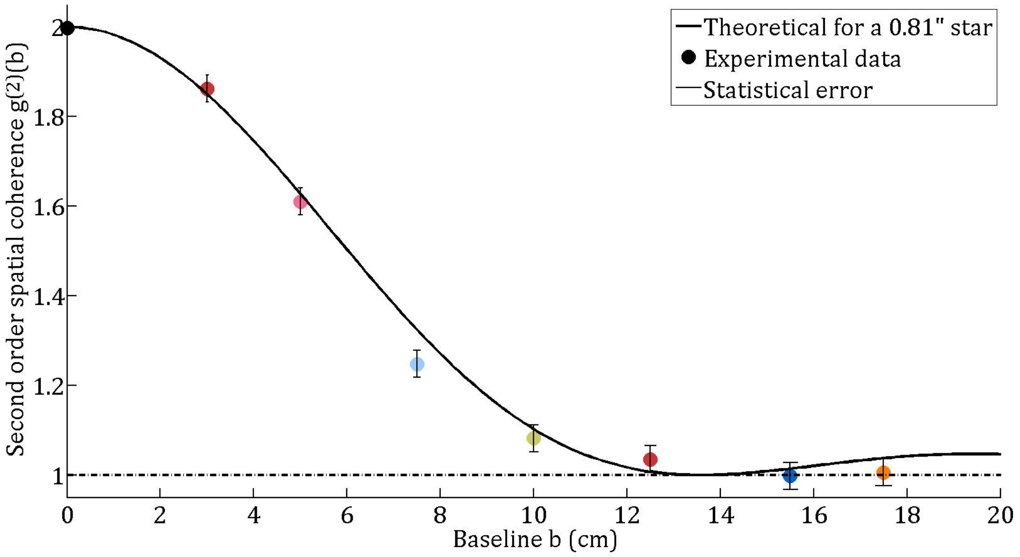

Figure 5.4: Second-order coherence as function of the telescopic baseline. The curve is the theoretical spatial coherence for a star with angular diameter of 0.81”. Colors are the same as in Figure 5.3

Finally, the spatial coherence $g^{(2)}(b)$ was obtained by plotting the maximum of $g^{(2)}(\tau, b)$ as a function of b and is shown in Figure 5.4. To find these maximum values, the correlation at each baseline was averaged for the time delays between 1 and 10 μs. The correlation values for time delays smaller than 1 μs were rejected due to their higher noise level. For the autocorrelation it is always less straightforward to find the value due to the afterpulsing. In fact, the maximum of $g^{(2)}(\tau, b = 0)$ may be hidden in the afterpulsing peak. Instead the maximum was estimated at the location where the autocorrelation curve would form a plateau. Then, the data were normalized in order to be compared with theoretical models. The normalization consisted by multiplying the values to obtain $g^{(2)}(\tau, b = 0) = 2$. It should be noted that such a normalization may contain errors because of the estimation of $g^{(2)}(b = 0)$. However, it is seen on Figure 5.4, that the $g^{(2)}(b = 3\text{cm})$ meets the theoretical curve. Since the cross-correlation is not affected by the afterpulsing, it confirms that the normalization was good. To find the statistical error, a set of measurements was made for one baseline keeping all the parameters constant. The deviation of the curves was used to calculate the error bars.

So far, this analysis permits to find stellar angular diameters only, similar to how intensity interferometry originally was used at Narrabri. One aim of reviving stellar intensity interferometry with the coming Cherenkov Telescope Array will be to enable stellar imaging. To do that, there is a need for a dense u-, v-plane coverage both to cover different spatial scales, and to retrieve a phase information. In this thesis the aim is to simulate such large array of telescopes. In Chapter 3, we introduced a method to use the laboratory array as a 2-dimensional array by rotating the pinhole. Let us then define $g^{(2)}(b, \theta)$, which is the spatial second-order coherence function redefined in polar coordinates, with b the baseline for a pair of telescopes, referring to the radial direction, and θ the angle of rotation of the pinhole. In this manner, it can be found a curve like Figure 5.4 ($g^{(2)}(b, \theta)$) for each θ. For visualizing that function, the data points from the 0.81” aperture are superposed onto a 3-dimensional theoretical plot of $g^{(2)}(u, v)$ in Figure 5.5.

For such a homogeneous circular star, $g^{(2)}(u, v)$ is obvious, however it becomes nontrivial for stars with more complex structures. For these stars, the experimental data were fitted to a 2-dimensional smooth mesh by *Matlab*, these results are presented in the following sections.

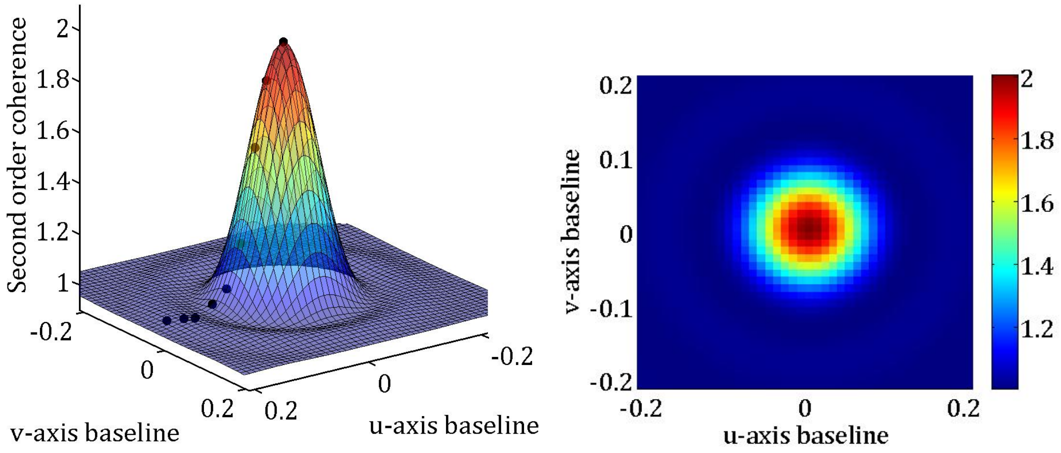

Figure 5.5: $g^{(2)}(b,\theta)$ is plotted in 2-dimensions (right) and 3-dimensions (left) for one angle θ. By doing the same measurements for different position angles θ's it is possible to obtain a map of $g^{(2)}(u,v)$.

5.2 Visibility curves for three round stars

First, it was of interest to look at simple stars such as the one in the previous example, all with similar geometry but of different sizes. The measurements were thus performed as explained above, but the analysis was constrained to a one-dimensional array (i.e., the second-order coherence curves were measured only for one position angle of the aperture θ). It is interesting to compare these curves, and see how they change as function of the angular diameter of the star. Here are the results for the three simple circular stars: 0.10mm #1, 0.15mm #1 and 0.20 mm #1. The curves resulting from the experiment are plotted together in Figure 5.6. The data points are compared to theoretical curves predicted from the experimental determination of the stellar diameters from their diffraction patterns. As expected, the coherence decreases faster with increasing baseline, as the size of the source increases. The results are satisfactory, as it can be seen that the data points follow the theoretical model quite well. This first result perfectly illustrates the principle of interferometry as well as the validity of the laboratory intensity interferometer. From this conclusion, it was possible to take the experiment to a new level and pursue the measurements for more complex targets.

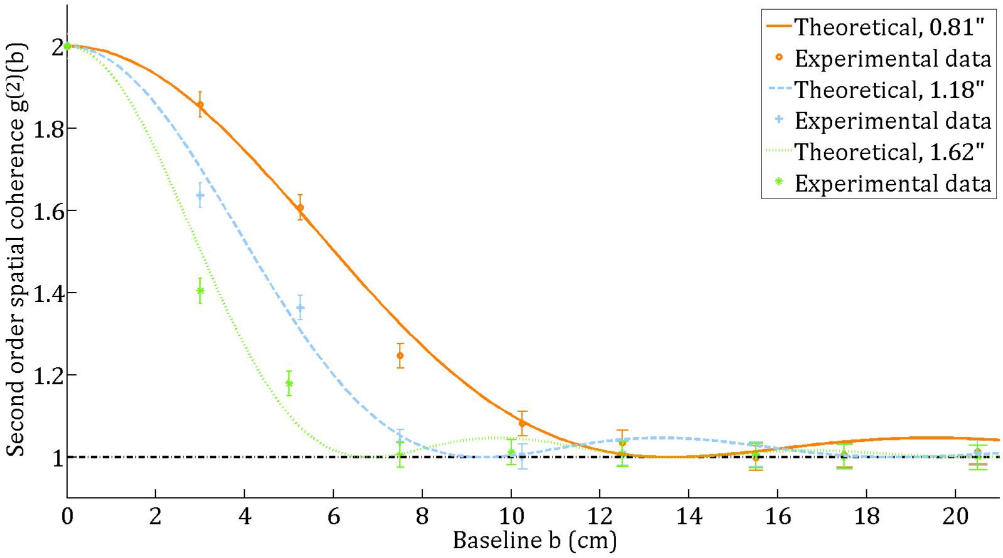

Figure 5.6: Spatial coherence for three circular uniform artificial stars of different angular extent. The experimental data points are plotted together with theoretical curves.

5.3 2D visibility map for a binary system

The double pinhole $0.10 + 0.10$ mm #1 was chosen to imitate a "binary star" for the purpose of studying more complex stellar structures. The two holes were made to be of the same size, and their Fourier transform (Chapter 4) revealed a very clean pattern which confirmed it. The analysis was conducted as previously for this star. The results obtained are seen in Figure 5.7. As expected, it was obtained a fringed coherence pattern due to the light from the two pinholes interfering. However, the fringes are not resolved perfectly due to the lack of even shorter baselines. In fact the curves that were expected are plotted as thin lines, while the curves in bold are what could be resolved with the laboratory set-up, thus only two "fringes" are "observed" while a fully resolved pattern should have shown three of them. Here the word "fringes" is within citation marks, since these are no physical fringes.

For this "complex" star system, the measurements were performed for different position angles in order to get the two-dimensional $g^{(2)}(u, v)$ map. It was obtained for six different angles; 0^o, 30^o, 60^o, 90^o, 120^o and 150^o. Since the array was able to measure ten baselines for each angle, this gave a total of 60 baselines plus one for the zero-baseline autocorrelation. However, since what is measured, is the squared visibility, the data are symmetric for a rotation of 180^o. Knowing this, allowed us to duplicate the data for the angles 180^o to 360^o, thus obtaining a total of 121 baselines. But, as already stated, there were two baselines of 5 cm and two of 10 cm in the one-dimensional array. Taking that into account, we ended up with only 8 effective baselines for each angle, i.e., a total of 97 baselines.

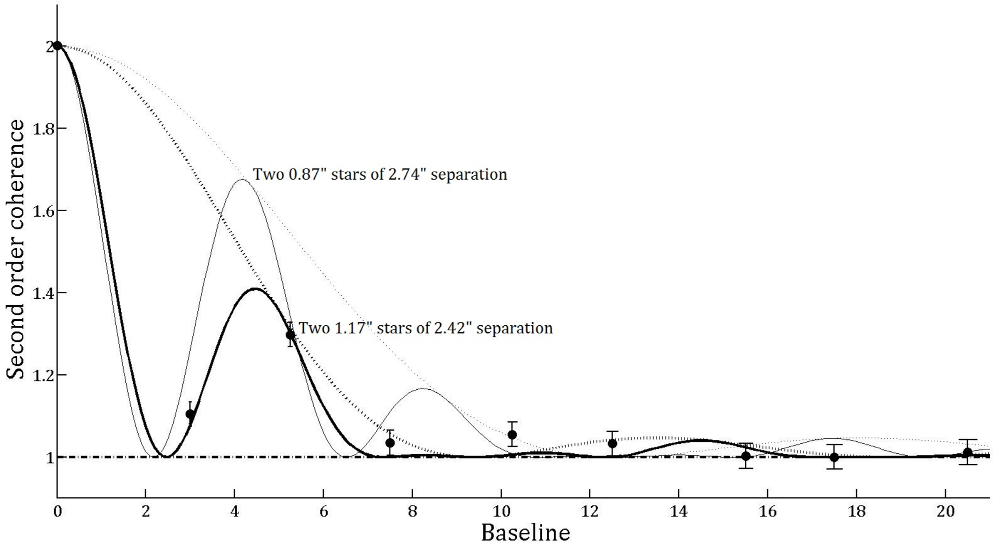

Figure 5.7: Experimental data points for a binary star with theoretical second-order coherence curves superposed. The bold one is what seemed to be fitting the data. The thin curve is the "true" curve that should have been obtained (calculated from the binary-star parameters determined in in the diffraction experiment), but since the array was somewhat undersampling, it was not able to resolve all the "fringes" peaks. Thus, it seems like the star is a binary of 1.17" with 2.42" separation, which is imprecise. Additionally, the curves for a single star are plotted as dashed lines as they enclose the "interference" ones, and show the size of the individual stars.

The corresponding baselines were converted to the Cartesian coordinates of the u-, v-plane, and the plotted data are shown in both two and three dimensions in Figure 5.8 with surface fit. It is even clearer in this figure that one fringing is missing. It should be noted that in spite of the sparsity of the data, the surface fit is already showing very clear structures in the Fourier domain. However, with such insufficient data the analysis would lead to erroneous stellar dimensions. In fact it was "resolved" a binary star of 1.17" angular diameters and 2.42" while the true dimensions were 0.84" angular diameter and 2.74" angular separation. The issue of undersampling the u, v-plane is, of course, common to all types of interferometers or Fourier-plane imagers and illustrates that any interferometer works best for sources which have angular extent matching its resolving power. Thus, a large interferometer would not be able to resolve large stars, which can be counter-intuitive. Such limitations can be compensated with more extensive u,v-plane coverage, such as will be available with the CTA configuration which will permit a very dense u, v-plane coverage, except perhaps for the very shortest baselines.

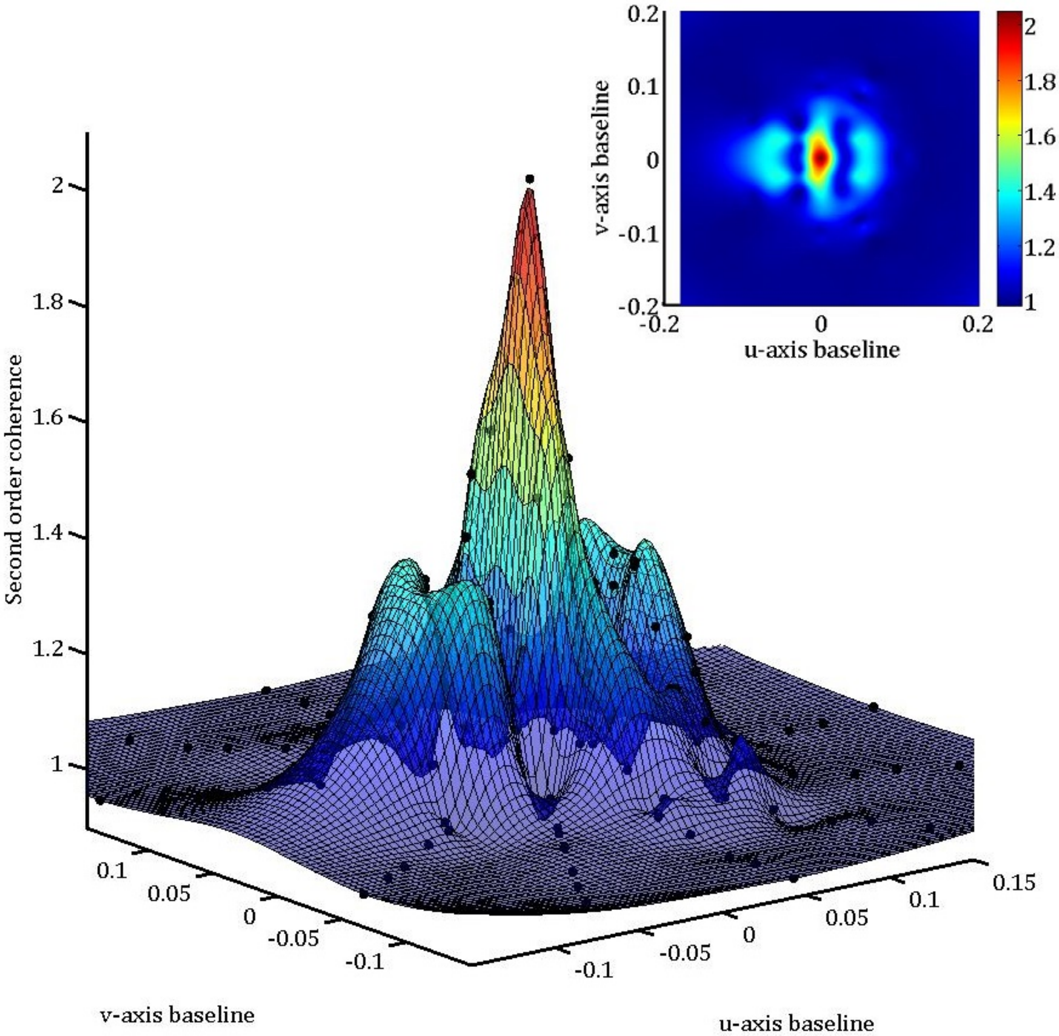

Figure 5.8: Experimentally determined two-dimensional (top) and three-dimensional (bottom) second-order spatial coherence for the binary star. The results show "fringes" verifying the binary nature of the source. Although the number of baselines was large, all spatial scales were still not resolved by the present telescope array. The plots also show the symmetry of the data around the u-axis).

5.4 2D visibility map for an elliptical star

Finally, the elliptical star was studied. It was judged to be the most interesting star since no gaps of relevant baselines were expected in its interferometric plane coverage. For this reason, the star was investigated thoroughly. A series of measurements was made for eleven angles; 0^o, 10^o, 20^o, 30^o, 60^o, 80^o, 90^o, 120^o, 150^o, 170^o and 180^o. Similar to what was done for the binary, the data were mirrored for angles spanning 180^o to 360^o. This time more data were duplicated coming from the angles 0^o, 180^o and 360^o. In total 161 baselines were obtained.

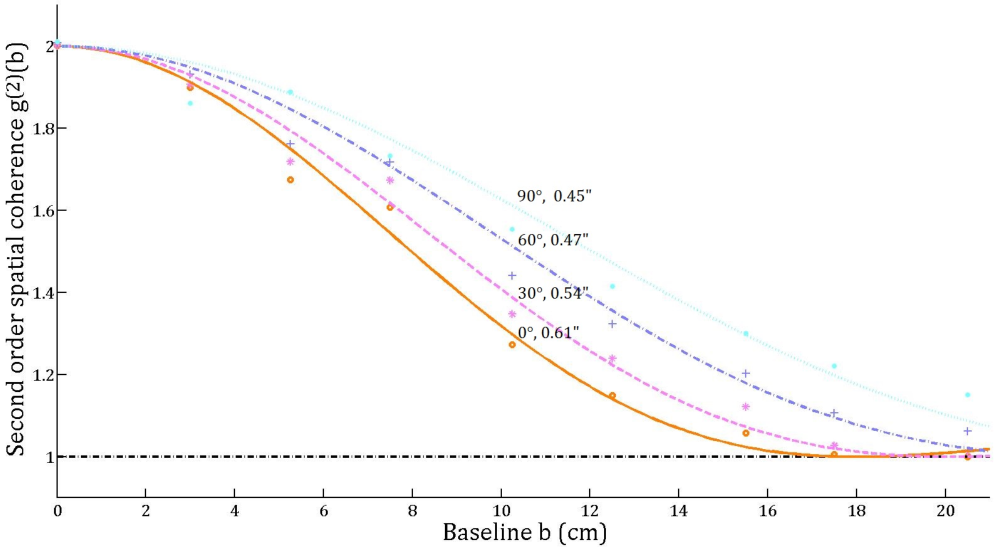

Figure 5.9: Second order coherence as a function of baseline for the elliptical star measured at some different position angles.

Some of the $g^{(2)}(\theta, b)$ curves are plotted in Figure 5.9 to show how the angular diameters measured were varying as θ was changed. In Figure 5.10, all the corresponding angular radii deduced are plotted in polar coordinates. On the figure, the ellipticity of the star is seen, its diameter is ≈ 0.60" at the maximum and slightly more than 0.40" at the minimum value which approximatively coincide with those obtained with the Fourier analysis, Table 4.1. Finally, the two- and three-dimensional fits of $g^{(2)}(u, v)$ are shown in Figure 5.11.

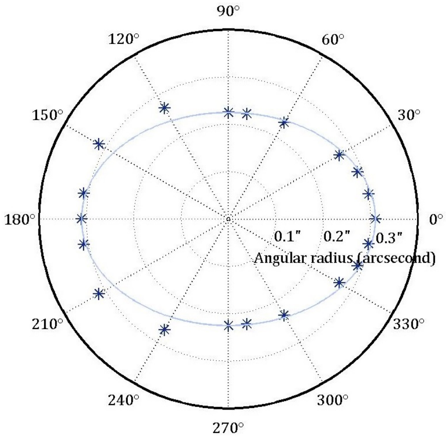

Figure 5.10: The experimentally determined angular radius of the elliptical star is plotted in arcseconds as a function of the position angle of the star θ in degrees and in polar coordinates. Superimposed on it is an ellipse of 0.45" and 0.62" minor and major diameters respectively.

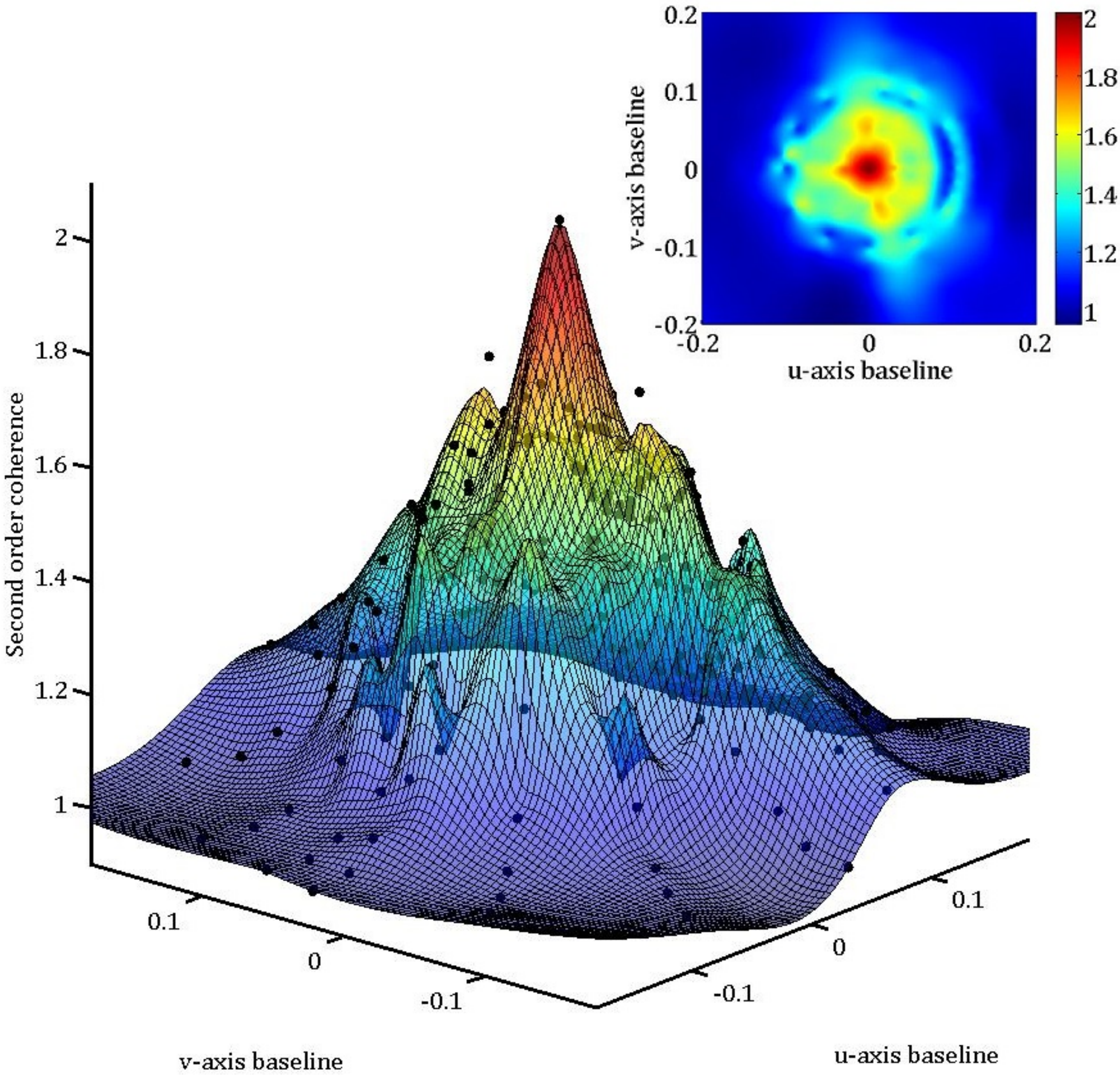

Figure 5.11: Two-dimensional (top) and three-dimensional (bottom) experimentally determined second-order coherence for the elliptical star. The results show a somewhat elliptical pattern indicating the non-symmetric nature of the source.

5.5 Image reconstruction

In this section, the work of Paul Nuñez, from Collège de France and Observatoire de la Côte d'Azur in Nice, is acknowledged. Paul Nuñez's doctoral work at the University of Utah dealt with image reconstruction of intensity interferometric data [29] and for this project he kindly performed full image reconstructions from the present laboratory data. The following results, are thus the outcome of his contributions.

Intensity interferometry only retains the squared magnitude of the visibility $V(u, v, 0)$; Equation 2.33, while the phase is also required to directly apply the Van Cittert-Zernike theorem. Therefore, image reconstruction from intensity interferometry is somewhat complicated. Nonetheless, advanced phase retrieval techniques have been worked out for also the particular aim of using Cherenkov telescopes for stellar intensity interferometry. One of these ideas is to use a higher-order correlation such as the third order one $g^{(3)}$ (correlation between 3 telescopes, i.e., $I_l * I_m * I_n$, with l, m and n indices for 3 locations). However $g^{(3)}$ seems to be seriously noise limited [30]. Another technique, the Cauchy-Riemman approach, involves fitting the data to analytical functions. Although the phase is not known, one can put some constraints onto it, such as that the phase should vary smoothly within the interferometric plane. Such techniques are only valid for a sufficiently dense interferometric plane coverage, such as what will be available with the Cherenkov Telescope Array. This approach hence provides a first "guess" of the phases of the Fourier components. The next important step in the image reconstruction (and indeed for any interferometric technique) is the post processing of the data, a task being here done with the software *MiRA* [31].

A first attempt was to fit the experimental data to an analytical function in order to apply the Cauchy-Riemman approach. This approach, however, proved unsuccessful as the u-, v-plane coverage of the laboratory setup was too sparse for its requirements. However, since the star did not possess further complex surface structures such as spots, it was instead possible to start by fitting the data to a Gaussian for a first guess, and then proceed with post-processing. The MiRA software then appeared to be a good tool to reconstruct an image from this first approximation; the results for the elliptical and the binary stars are shown in Figure 5.12.

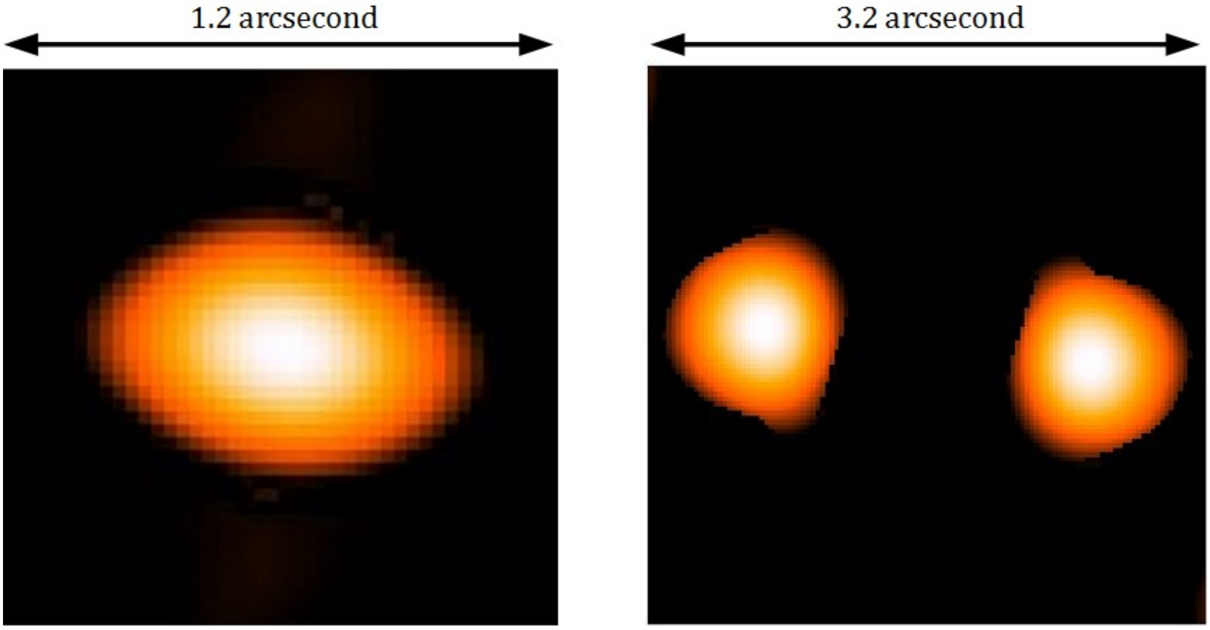

Figure 5.12: Reconstructed images of the elliptical star (left) and the binary (right). The experimental data were first fitted to a Gaussian function, and the images were then post-processed with the software *MiRA*. (Computations by Paul Nuñez, Collège de France and Observatoire de la Côte d'Azur.)

Chapter 6

Additional tests

6.1 Different scatterers

In Chapter 3, it was mentioned that a set of polystyrene microspheres was available, originally ordered for the scattering of the starlight. Although it was chosen to use milk for most measurements, tests were also performed with the micro-spheres. The main motivation was to study how temporal coherence would evolve as a function of the suspended microspheres sizes in regard to Equation 3.1.

A set of six different microspheres sizes; 0.05, 0.2, 0.45, 1, 45 and 90 μm were available. Out of these six different sizes, only three of them showed significant SNR to measure the temporal coherence; 0.20, 0.45 and 1 μm. The baseline of 5 cm and the circular aperture of 100 μm were used. The different micro-sphere coherence curves obtained are plotted together in Figure 6.2. It can be seen that the temporal coherence increases as the size of the micro-spheres increases. This is a direct result of Equation 3.1; the larger the particles, the slower they move, and thus the slower the scattered intensity fluctuates.

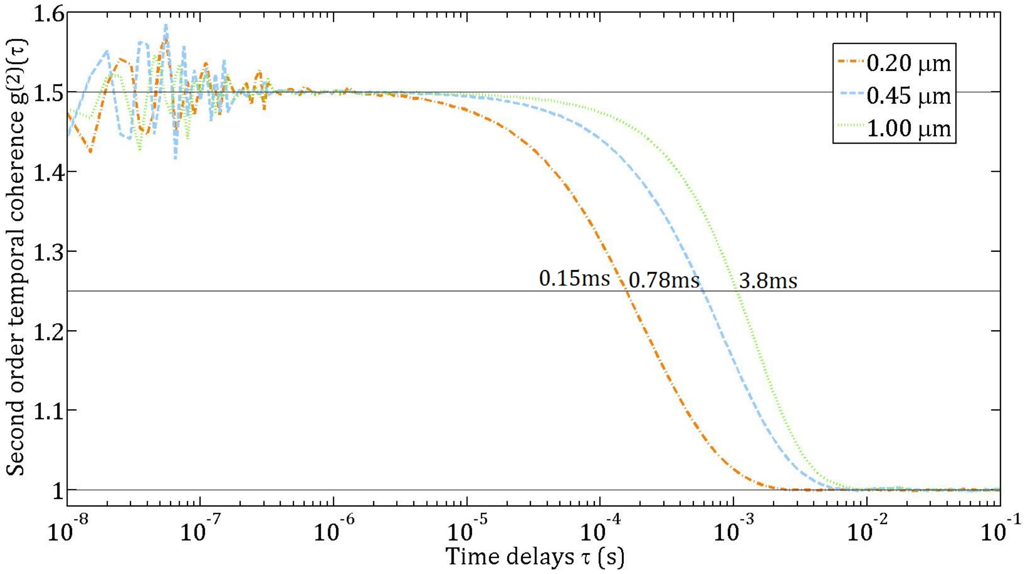

Figure 6.1: Temporal coherence measured for suspensions of micro-sphere of three different sizes.

Following that, two different sizes of particles were mixed and the coherence was measured again. It appeared that the temporal coherence was in all cases determined by the smaller particles, which makes sense as they are the ones moving the fastest.

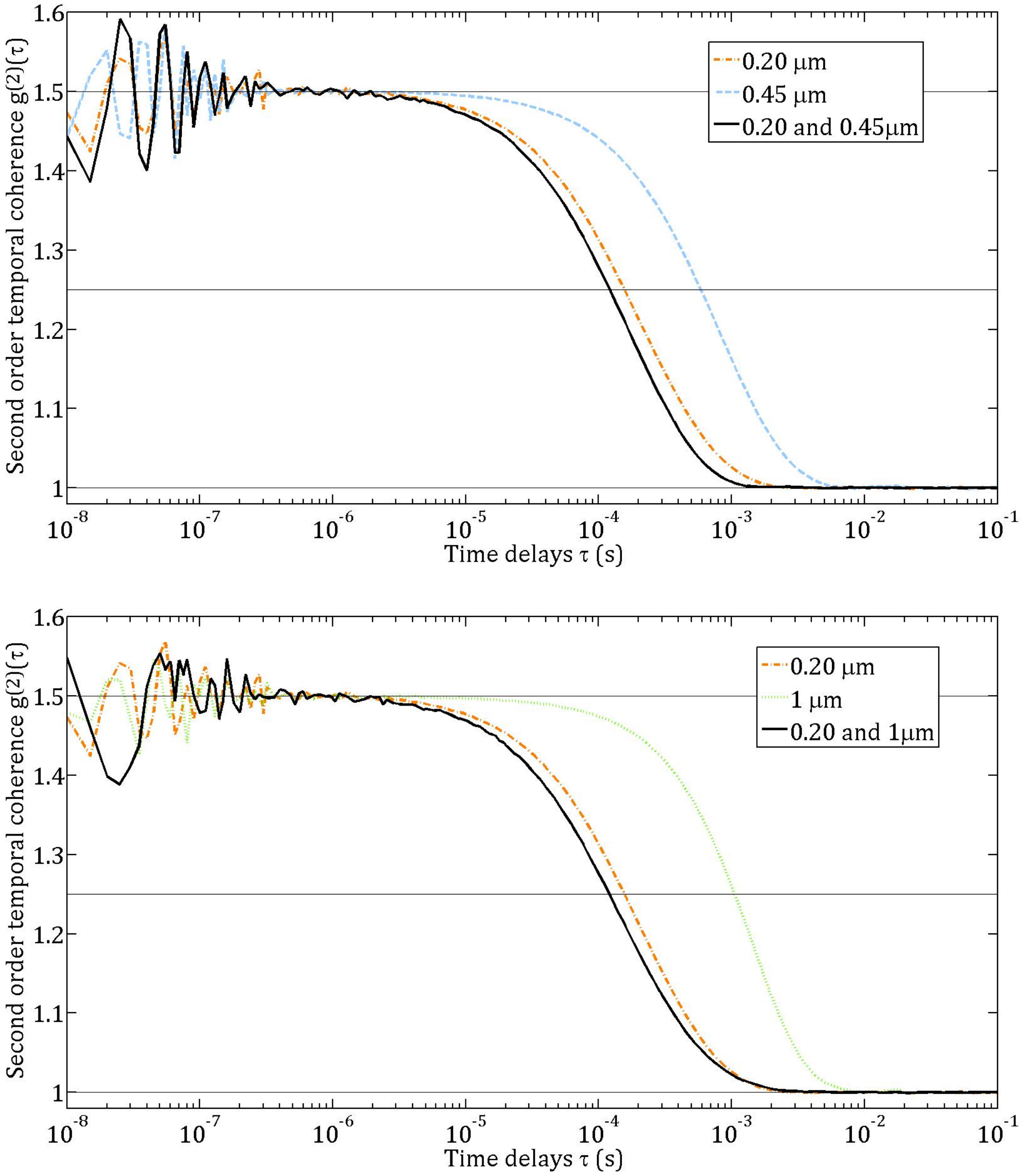

Figure 6.2: Temporal coherence measured for a suspension mix of two different micro-sphere sizes compared to those of single sizes.

6.2 Polarization effects

The squared visibility V^2 (corresponding to $g^{(2)} - 1$) should ideally decrease by a factor of two when the light is unpolarised as compared to linearly polarised light [22]. For this reason it was decided to check that with the set-up. A polarisation filter was used right after the star and the cross- and auto-correlations were measured for one baseline. The same was done without the filter and the results are compared in Figure 6.3. A stringent trend is seen; both auto- and cross-correlations increase significantly when using a polarisation filter. However the corresponding V^2 increase is slightly less than two. This could be explained by the fact that the light resulting from the scattering is already partly polarized.

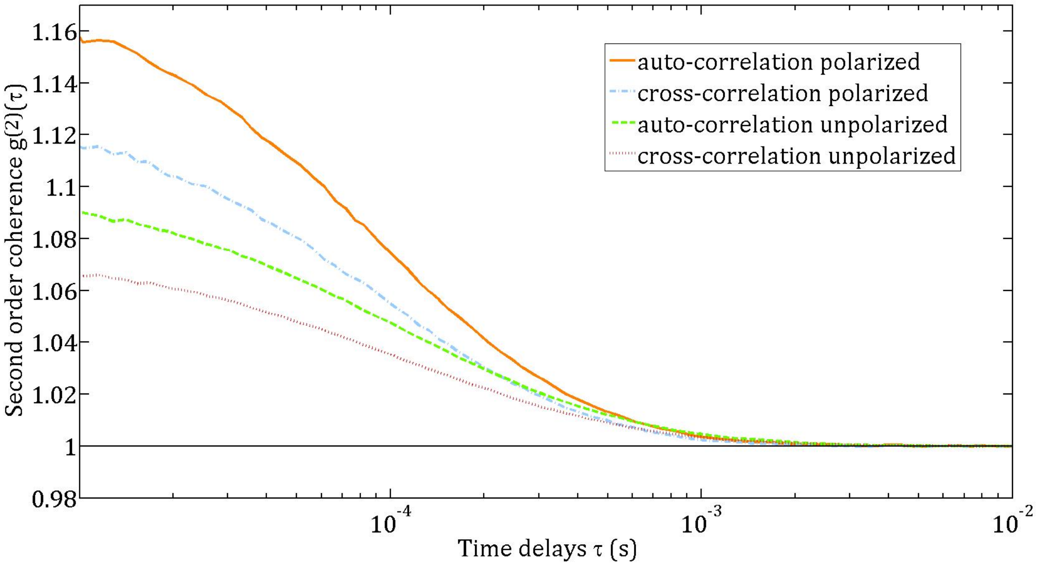

Figure 6.3: Correlation (auto- and cross-) measured with and without a polarising filter. The correlations increase when the light is polarised, as expected theoretically.

Chapter 7

Discussion and conclusion

7.1 Interpretation of the experimental results

In this experimental simulation, a telescope array was built and used to successfully carry out intensity interferometry on several different artificial stars. This was done by measuring the correlation of fluctuations in light between different pairs of telescopes. It permitted to determine the second-order spatial coherence of the various artificial stars.

In a first sequence, five telescopes positioned along a line provided a one-dimensional array. In this configuration, the second-order spatial coherence of starlight was measured along one dimension. This quantity permitted to determine the apparent stellar angular diameters. In this manner, this first array configuration performed measurements analogous to those made with the Hanbury Brown and Twiss original interferometer in Narribri. The main difference in array configuration was that several fixed telescopes were used to produce the different baselines needed, rather than using two mobile telescopes. One advantage of such a configuration, is that the correlation in intensity fluctuations can be measured simultaneously between different pairs of telescopes.

The angular diameters of three round stars were determined in this manner. Prior experimental analysis of the aperture sizes and shapes trough diffraction of light provided independent measurements of the angular diameters. Thus, it was possible to compare these results with the ones produced by the laboratory array and the comparisons showed good agreements. It confirmed that the requirements for doing intensity interferometry were correctly understood and carried out in the experiment.

In the second step, the array was reconfigured to become a two-dimensional array by rotating the position angle of the artificial "stars", as was explained in previous chapters. Interesting targets for this configuration were the non-symmetrical ones, such as the elliptical and the binary "stars". The binary was first measured with a total of 97 baselines. Such a large number of baselines allowed to reconstruct a two-dimensional map of the spatial coherence. It was realised that the binary separation was too large to be fully resolved by the telescope array, due to a lack of shorter baselines. This well illustrates one of the limitations of any actual interferometer; they can only resolve spatial features within their resolution power. For this very reason, it is desirable to have many different baselines, in order to cover all spatial scales.

One elliptical star was also measured. Its spatial coherence was measured at different position angles, thus obtaining different angular diameters at each orientation, revealing the ellipticity of the star. In a similar manner as for the binary, a two-dimensional map was reconstructed, this time for a total of 161 baselines. The resulting maps for both stars showed that for the number of baselines used it was already possible to recognize rather complex patterns.

The measurements of the elliptical and the binary stars were complemented by full image reconstructions, performed by Paul Nuñez from Collège de France and Observatoire de la Côte d'Azur in Nice. The resulting images show the potential of a Cherenkov Telescope Array configuration for stellar surface imaging. Once again, what the experiment highlighted for the particular purpose of making images, was the need for a dense interferometric plane coverage, especially if more complex surface structures are to be resolved on real stars. Most importantly, this is an experimental demonstration that (and how) it is possible to produce direct images of stars through intensity interferometry. Obviously, with its more than 1000 possible baselines, spanning over a couple of kilometers, the Cherenkov Telescope Array will have the potential of producing images, of at least hotter stars, with an unprecedented resolution.

7.2 Lessons learned

It is clear that through this laboratory experiment, significant experience was gained, both for the experimental procedure and for the data handling and data analysis. Moreover the experiment addresses relevant considerations for instrument optimization.

Regarding first the cameras; while the single-photon avalanche-diode detectors have proved perfectly adequate for the laboratory simulation, it would be desirable to have such with shorter deadtimes and able to handle large photon count rates. There also exist other ideas for improving the SNR. It can be noted from Equation 2.38 that the SNR is independent of the spectral passband. In this manner, the SNR ratio could be considerably increased by simultaneously measuring the correlations in different spectral channels. Ideally, a wavelength-resolving photon counting detector would represent a promising instrument for intensity interferometry. Currently, this option stands in the state of a dream, as such devices are not yet available. However, already a low-resolution spectrometer with multiple detectors could be a step in that direction.

Another concern for the actual cameras regards the size of the photosensitive area. Actual Cherenkov telescopes produce quite large images of stars, requiring correspondingly larger detectors. Such detectors are currently being developed in industry, e.g., digital silicon photomultipliers which have the advantage of combining both the speed performances of a single-photon avalanche-diode with a CMOS logic array. Such types of two-dimensional single-photon avalanche-diode arrays would be of interest for actual stellar intensity interferometry applications.

A further practical issue regards the adaptation of the camera to the Cherenkov telescopes, which of course have their own special cameras for detecting Cherenkov light flashes. Ideally independent cameras should be added for intensity interferometry. This is an important issue that is being considered in the actual design of the Cherenkov telescopes. One option is to have the camera placed on the outside lid of the Cherenkov camera, while another suggested option is to have one pixel of the Cherenkov camera available for other measurements such as intensity interferometry.

Regarding the computation of the correlation, the experiment showed the simplicity, and time efficiency in the use of a digital correlator. This type of real-time data processor only saves the correlation functions. However, since these are calculated and immediately displayed, it permits to have a real-time data feedback, thus if a problem were to occur, it could be detected and eventually fixed already during the data acquisition. However, it is still to be decided whether instead to record and store all the raw data or just discard them. On one hand, keeping the data would involve the need for a large storage capacity, but on the other hand it could enable a more advanced data analysis, such as retrieving also higher-order correlations.

Finally, some other issues which are not covered by this experiment still remain to be solved. For example, one needs to understand what would be the influence of using several meter- or even kilometer-long (metal or optical?) cables to connect the telescopes between them. In this experiment, both ≈ 0.5 m and ≈ 10 m-long BMC cables were tested with no observable difference. Another issue may arise form the large size of the Cherenkov telescopes if observing relatively large sources.The correlation will thus be averaged over the telescope area, which will decrease the coherence measured, and will have to be accounted for. According to Hanbury Brown and Twiss [22], the decrease can be expressed by multiplying the correlation by a factor which depends upon the stellar angular diameter, the baseline, the telescopes position in the interferometric plane and the size of the detector.

7.3 Ideas for future improvements

Obviously, effects of random noise could be mitigated by repeating the measurements in a systematic manner and thus obtaining better statistics. However, the overall aim of the project was to demonstrate the feasibility of stellar intensity interferometry with a telescope array analogous to the Cherenkov Telescope Array, and to validate the theory with a reasonable precision. In fact, the experiment could hardly be made more precise without using a more elaborated laboratory setup. For example, more telescopes could be added to increase the number of baselines, thus improving the quality of the data, but this would not add significantly to the principal interpretation of the results.

In spite of that, a number of implementations exist that could significantly improve the realism of the experiment. The most obvious one, is the use of a more realistic light source, more similar to actual starlight. Although the dynamic scattering technique does a good job in providing chaotic light, its long temporal coherence still deviates a lot from realistic starlight, even if applying a narrow bandpass color filter. The difficulty of producing thermal light in the laboratory with sufficient surface brightness has already been discussed above. However, novel light sources that might also mimic hot stars are becoming available. For instance, during the SPIE conference on *Astronomical Telescopes + Instrumentation* in Montreal in June of this year, a commercial company (ENERGETIQ) demonstrated a device producing highly brilliant thermal white light. The device is driven by a broadband laser which keeps a tiny volume of plasma heated to more than 10,000K, a temperature not unlike the stars desired to be observed. Such a light source might be very useful for upgrading the present experiment, providing astrophysically realistic broad-band light. In addition to that, it could be used to test simultaneous observations in multiple spectral bandpasses.

Another envisioned future experiment would be to test the set-up on actual telescopes for observing actual stars and trying to retrieve correlations. Additional external factors will then enter, and one will need to understand them before full-scale operations can be pursued. What kind of external noise sources might affect the SNR and what durations of exposure times are realistic?

7.4 Issues encountered

During the experiment, it was realised that the detectors are so sensitive that they may pick up various signals from somewhere in their environment, which happened a few times. During some measurements, a sinusoidal signal was seen at a frequency of 1 MHz, the origin of which was never figured out. However, such a signal affects the measured correlation, which of course is a problem. Actually, if all the measurements would be performed with the same superposed signal, then it might be calibrated out by the normalisation. However, if it appears only during some part of the experiment, it can become very tricky to compensate for it. In any case, such interfering signals are not desirable.

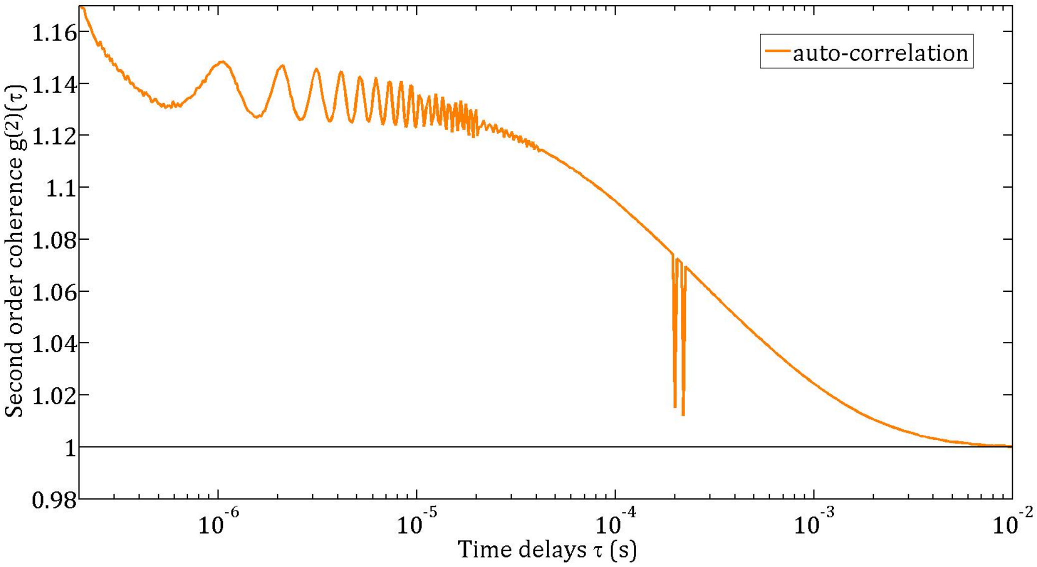

Figure 7.1: Example of a weird signal sometimes seen. This might plausibly have originated from some electronic device in, or near the building, but its origin was never determined.

Chapter 8

Summary

Intensity interferometry was invented in 1949 by Robert Hanbury Brown and Richard Q. Twiss. Despite a successful start, it has not been used recently, mainly due to the need for large telescopes. Possibilities to revive the technique have recently emerged with the development of Cherenkov telescopes which observe gamma-ray induced Cherenkov light in air and are also suitable for intensity interferometry. The planned CTA, the Cherenkov Telescope Array is of particular interest with its large baselines envisioned. The aim will not be to merely measure angular diameters, but to produce optical images of stars with a potential resolution reaching nearly 0.05 mas, roughly ten times better than what currently is feasible. The fundamental principle remains the same as in the original intensity interferometer, but new technologies could open up a whole new science topic of stellar surface imaging.

In this project, a revised technique of intensity interferometry was tested for a simulated CTA-type telescope array. The main difference from the previous one in Narribri lies in the telescopes configurations offered by CTA. The combination of a large number of telescopes enables numerous unique baselines, and provides the key capability in using intensity interferometry for imaging. The project also tested the performance of new solid-state photon detectors and digital data processors for the technique. It is thus an essential step between the basic theory and actual stellar observational runs with the CTA facility.

The large optical laboratory (≈ 25 m) of Lund Observatory was used for setting up the experiment. At one end of the room, a small-scale array of laboratory telescopes was built in order to observe artificial stars at the opposite end of the room.
Intensity interferometry measures the second-order coherence of light, sensitive to also the quantum statistics of the photons. For fundamental reasons, the laboratory light illuminating the artificial stars had to be of a thermal and chaotic nature, i.e., with bunching of photons. In addition the light had to be bright in order to obtain adequate photon fluxes at the telescopes. Such light was obtained by scattering laser light onto microspheres suspended in water, undergoing thermal (Brownian) motion. The laser light provided a very high brightness temperature (but without photon bunching), while the resulting scattered light had the required photon bunching (i.e., the photons were more likely to be emitted in bunches during a coherence time characteristic of the (Doppler) velocity of the microspheres) but still retaining the brightness temperature.

The telescopes were made with simple achromatic lenses focusing the starlight onto fast photon-counting semiconductor detectors (avalanche photodiodes). The signals were fed to a digital data processor computing correlation functions for photon arrival coincidences between pairs of telescopes. The data analysis provided second-order coherence functions. In order to simulate a two-dimensional telescope array, the position angle of the artificial star was rotated in steps, thus enabling measurements for many baselines with successively different position angles in the interferometric plane. This allowed the reconstruction of two-dimensional maps of the second-order coherence, which is required for reconstructing actual images.

For most artificial stars (three round and one elliptical), the angular diameters could directly be retrieved from such analysis (with good agreement with independent diameter measurements made through diffraction). For a binary star, the array was not able to fully resolve the binary separation since that was too large relative to the shortest baselines available. Using these data, image reconstructions of both the binary and the elliptical stars was performed by Paul Nuñez in Nice, an expert in the field. Although the interferometric plane coverage was sparser in comparison to what will be available with CTA, it was already possible to obtain images.

This work thus carried out a rather complete end-to-end simulation of stellar intensity interferometry. The results showed good agreements with the theory, validating that the concepts are well understood. Furthermore, it confirmed that the detectors used, the signal handling, the digital data processors, and the reconstruction algorithms had adequate capability to carry out stellar intensity interferometry with also large telescope arrays, with a view toward the upcoming CTA.

Publications and presentations

Results from the project have been presented at:

(1) *Astronomdagarna 2013* , Lund Observatory, October 2013.

Poster presented:
"*Optical interferometry over kilometer baselines*
Diffraction-limited imaging with Cherenkov telescope arrays"
`https://www.dropbox.com/s/dndj407y0x5c74l/Lund_AD_2013_Interferometry.pdf`

(2) *Workshop on Hanbury Brown & Twiss interferometry: Prospects for astrophysics and quantum optics*, Observatoire de la Côte d'Azur, Nice, France; May 2014.
`https://www.oca.eu/spip.php?article850`

Talk presented:
"*Reviving Stellar Intensity Interferometry with CTA*"
`https://www.oca.eu/IMG/pdf/HBT_Lagadec.pdf`

(3) The SPIE conference on *Astronomical Telescopes + Instrumentation* in Montréal, Québec, Canada, June 2014
`http://spie.org/x13662.xml`

Talk presented jointly with Dainis Dravins:
"*Stellar intensity interferometry over kilometer baselines: Laboratory simulation of observations with the Cherenkov Telescope Array*"
Proc. SPIE 9146, Optical and Infrared Interferometry IV (Jayadev K. Rajagopal; Michelle J. Creech-Eakman; Fabien Malbet, eds.), 91460Z (2014). Preprint: arXiv: 1407.5993
`http://proceedings.spiedigitallibrary.org/proceeding.aspx?articleid=1891922`
`http://arxiv.org/abs/1407.5993`

Bibliography

[1] D. Hoffleit and W. H. Warren. Bright Star Catalogue, fifth revised ed., 1995. `http://cdsarc.u-strasbg.fr/`.

[2] H. Jensen, D. Dravins, S. LeBohec, and P. D. Nuñez. Stellar intensity interferometry: optimizing air Cherenkov telescope array layouts. volume 7734 of *Proc. SPIE*, 2010.

[3] P. R. Lawson. Notes on the History of Stellar Interferometry. In P. R. Lawson, editor, *Principles of Long Baseline Stellar Interferometry*, page 325, 2000.

[4] Académie des sciences (France). Prix Bordin, Rapport sur le Concours de l'année 1867. In *Comptes rendus hebdomadaires des séance de l'Académie des sciences*, 1868.

[5] A. A. Michelson. On the Application of Interference Methods to Astronomical Measurements. *Philosophical Magazine and Journal of Science*, 30:182, 1890.

[6] A. A. Michelson. Measurement of jupiter's satellites by interference. *Publ.Astron.Soc.Pacific*, 3:274–278, 1891.

[7] A. A. Michelson and F. G. Pease. No. 203. Measurement of the diameter of alpha Orionis with the interferometer. *Contributions from the Mount Wilson Observatory / Carnegie Institution of Washington*, 203:1–11, 1921.

[8] R. Hanbury Brown. A Test of a New Type of Stellar Interferometer on Sirius. *Nature*, 178:1046–1048, 1956.

[9] R. Hanbury Brown. *Boffin: A personal story of the early days of radar, radio astronomy and quantum optics.* 1991.

[10] E. S. Kulagin. A Superposed-Ray Interferometer. *Sov.Astron.*, 13:1023, 1970.

[11] D. G. Currie, S. L. Knapp, and K. M. Liewer. Four stellar-diameter measurements by a new technique: amplitude interferometry. *Astrophys.J*, 187:131–134, 1974.

[12] D. W. McCarthy and F. J. Low. Initial results of spatial interferometry at 5 microns. *Astrophys.J.Lett.*, 202:L37–L40, 1975.

[13] A. Labeyrie. Interference fringes obtained on VEGA with two optical telescopes. *apjl*, 196:L71–L75, March 1975.

[14] D. Mourard, I. Tallon-Bosc, A. Blazit, D. Bonneau, G. Merlin, F. Morand, F. Vakili, and A. Labeyrie. The GI2T interferometer on Plateau de Calern. *Astron.Astrophys.*, 283:705–713, 1994.

[15] M. Shao and D. H. Staelin. Long-baseline optical interferometer for astrometry. *J.Opt.Soc.Am.*, 67:81–86, 1977.

[16] M. Shao and D. H. Staelin. First fringe measurements with a phase-tracking stellar interferometer. *Appl.Opt.*, 19:1519–1522, 1980.

[17] J. E. Baldwin, M. G. Beckett, R. C. Boysen, D. Burns, D. F. Buscher, G. C. Cox, C. A. Haniff, C. D. Mackay, N. S. Nightingale, J. Rogers, P. A. G. Scheuer, T. R. Scott, P. G. Tuthill, P. J. Warner, D. M. A. Wilson, and R. W. Wilson. The first images from an optical aperture synthesis array: mapping of Capella with COAST at two epochs. *Astron.Astrophys*, 306:L13, 1996.

[18] Bély P. Y, Laurance R. J, Volonte S., Greenaway A., Haniff C., Lattanzi M., Mariotti J. M, Noordam J. E, Vakili F., von der Lühe O., Lambert H., Calvel B., Scaddan R., and Vangasse P. Kilometric Baseline Space Interferometry. In P. Y. Bely and J. B. Breckinridge, editors, *Space Telescopes and Instruments V*, Proc.SPIE 3356, pages 58–73, 1998.

[19] A. Labeyrie. Resolved imaging of extra-solar planets with future 10-100km optical interferometric arrays. *Astron.Astrophys.Suppl.*, 118:517–524, 1996.

[20] R. Hanbury-Brown and R. Q. Twiss. Correlation Between Photons in Two Coherent Beams of Light. *J.Astrophys.Astron.*, 15:13, 1994.

[21] A. D. Code, R. C. Bless, J. Davis, and R. H. Brown. Empirical effective temperatures and bolometric corrections for early-type stars. *Astrophys.J.*, 203:417–434, 1976.

[22] R. Hanbury Brown. *The intensity interferometer: Its application to astronomy.* 1974.

[23] The Cherenkov Telescope Array. `http://www.cta-observatory.org/`.

[24] H.Jensen. A hundred times sharper than Hubble: Stellar imaging with intensity interferometry. Master's thesis, Lund University, 2010.

[25] P. D. Nuñez, S. LeBohec, D. Kieda, R. Holmes, H. Jensen, and D. Dravins. Stellar intensity interferometry: imaging capabilities of air Cherenkov telescope arrays. In *Proc. SPIE*, volume 7734, July 2010.

[26] Saleh B. E. A. and Teich M. C. *Fundamentals of photonics.* Wiley-VCH.

[27] Labeyrie A., Lipson S. G., and Nisenson P. *An introduction to optical stellar interferometry.* Cambridge University Press.

[28] R. Hanbury Brown and R. Q. Twiss. Interferometry of the Intensity Fluctuations in Light. III. Applications to Astronomy. *Proc.Roy.Soc.A*, 248:199–221, 1958.

[29] Paul Nuñez. *Toward Optical Itensity Interferometry for High Angurlar Resolution Stellar Astrophysics.* Doctoral degree, University Of Utah,, 2012.

[30] V. Malvimat, O. Wucknitz, and P. Saha. Intensity interferometry with more than two detectors? *Month.Not.Roy.Astron.Soc*, 437:798–803, January 2014.

[31] MiRA: image reconstruction for optical interferometry.
`http://cral.univ-lyon1.fr/labo/perso/eric.thiebaut/?Software/MiRA`.